Development and Processing of p-type Oxide Thermoelectric Materials

Wu, NingYu

Publication date:
2014

Document Version
Publisher's PDF, also known as Version of record

Development and Processing of p-type Oxide Thermoelectric Materials

Ph.D. Thesis

NingYu Wu

Supervisor: Prof. Søren Linderoth
Co-Supervisor: Prof. Nini Pryds
Dr. Ngo Van Nong

Institut for Energikonvertering og –lagring
Danmarks Tekniske Universitet
Risø, Denmark

October 2014

Abstract

The main aim of this research is to investigate and develop well-performing p-type thermoelectric oxide materials that are sufficiently stable at high temperatures for power generating applications involving industrial processes.

Presently, the challenges facing the widespread implementation of thermoelectric power generation technology lie in the high cost and low efficiency of thermoelectric systems. Scalable and practical applications, including commercialization based on the currently used materials are subject to environmental and cost issues, and thus are difficult to be realized. Metal oxides have attracted much attention due to features such as a natural abundance of constituent elements, environmental benignity and durability at high temperature in air. This research aims to develop and investigate the misfit-layered cobaltate $Ca_3Co_4O_{9+\delta}$, which demonstrates a large potential for high temperature applications owing to its large positive Seebeck coefficient (S) together with a metallic-like electrical conductivity and a low thermal conductivity typical of a "phonon glass–electron crystal".

The research begins with the study of $Ca_3Co_4O_{9+\delta}$ syntheses by solid-state and sol–gel reactions, followed by the use of spark plasma sintering (SPS) processing with different conditions such as sintering temperatures, applied pressures and ramping rates. With characterization of the microstructure, bulk density and thermoelectric transport properties, $Ca_3Co_4O_{9+\delta}$ synthesized by sol–gel reaction followed by the proper spark plasma sintering processing conditions is suggested to be a beneficial means of obtaining high-performance $Ca_3Co_4O_{9+\delta}$ owing to the resulting smaller particle sizes and enhanced grain alignment.

Other than the conventional solid-state reaction and sol–gel methods, a rapid auto-combustion reaction for the synthesis of $Ca_3Co_4O_{9+\delta}$ nano-powder is developed to realize nanostructuring for enhanced thermoelectric properties. The procedure is a modification of the conventional citrate–nitrate sol–gel method where an auto-combustion process is initiated by a controlled thermal oxidation–reduction reaction. This synthesis produces morphological and compositional homogeneity, and fine, well-defined particle sizes. With determined optimal spark plasma sintering processing conditions, highly dense and beneficially textured $Ca_3Co_4O_{9+\delta}$ can be fabricated.

Introducing extrinsic elements as dopants may exert great influence on the thermoelectric properties. Singly Fe-doped and Fe/Y co-doped $Ca_3Co_4O_{9+\delta}$ samples synthesized by the newly developed auto-combustion reaction followed by spark plasma sintering processing with the effects of Fe and Fe/Y doping on the high temperature thermoelectric properties (from room temperature to 800 ℃) were investigated and discussed. The Fe substitution at the Co-sites effectively reduces the electrical resistivity (ρ) while the Seebeck coefficient is influenced only

slightly. Y substitution for Ca^{2+} leads to an increase in the Seebeck coefficient but also in the electrical resistivity. With a proper amount of Fe co-doping, the increase in the electrical resistivity was compensated, and together with the improved Seebeck coefficient the addition of Fe lead to the enhancement of the overall thermoelectric performance.

With the aforementioned approach, further investigation has been conducted on rare-earth doping with Ce in $Ca_3Co_4O_{9+\delta}$ in order to explore the effects on the high temperature thermoelectric properties. With the auto-combustion reaction synthesis followed by spark plasma sintering processing, $Ca_{3-x}Ce_xCo_4O_{9+\delta}$ exhibited increasing electrical resistivity and Seebeck coefficient with increasing Ce doping content over the whole measured temperature range, while the in-plane thermal conductivity (κ) was only slightly influenced. Since the introduction of Ce leads to a small decrease in the power factor (*PF*) but also reduction in the thermal conductivity resulting in the figure-of-merit (*ZT*) values being similar to the un-doped $Ca_3Co_4O_{9+\delta}$, the *ZT* may be enhanced in rare-earth and transition metal (e.g., Ce and Fe) co-doped $Ca_3Co_4O_{9+\delta}$ through decoupling of the otherwise interdependent electronic and thermal transport properties.

Resumé

Denne afhandlings fokus er at undersøge og udvikle p-type termoelektriske materialer med god ydeevne, der udviser tilstrækkelig stabilitet ved høje temperaturer til at de kan benyttes til strømgenerering ved industrielle processer.

I øjeblikket ligger udfordringerne der forhindrer termoelektrisk strømudvinding i at blive almindeligt udbredt i de store omkostninger samt ringe nyttevirkning af nuværende termoelektriske systemer. Skalerbare og praktisk anvendelige systemer er derudover svære at realisere, da kommercialisering på baggrund af de anvendte materialer er underlagt miljømæssige og omkostningsmæssige problemer. Metaloxider har tiltrukket megen opmærksomhed på grund af forhold som naturlig overflod af de anvendte grundstoffer, gode miljømæssige egenskaber samt holdbarhed ved høj temperatur i luft. Denne forskning har til formål at udvikle og undersøge defekt-laget cobaltat $Ca_3Co_4O_{9+\delta}$, som udviser et stort potentiale for brug ved høje temperaturer på grund dets store positive Seebeck-koefficient (*S*) sammen med en metallisk-lignende elektrisk ledningsevne og en lav varmeledningsevne, som er typisk for en "phonon glas–elektron krystal".

Afhandlingen starter med studiet af $Ca_3Co_4O_{9+\delta}$ synteser ved faststof-reaktion og sol–gel reaktioner, efterfulgt af brug af spark plasma sintring (SPS) under forskellige forhold som sintringstemperaturer, temperaturprofiler og anvendt tryk. Efter karakterisering af mikrostruktur, densitet og termoelektriske transportegenskaber af $Ca_3Co_4O_{9+\delta}$ syntetiseret ved sol–gel-metoden efterfulgt af de rette SPS forarbejdningsbetingelser, er dette fundet at være en gavnlig måde at opnå højtydende $Ca_3Co_4O_{9+\delta}$. Den resulterende højtydende effekt skyldes små partikelstørrelser samt øget korntilpasning.

Foruden den konventionelle faststof-reaktion og sol–gel-metode, er en hurtig auto-forbrændingsreaktion for syntesen af $Ca_3Co_4O_{9+\delta}$ nano-pulver udviklet for at opnå nanostrukturering, som giver forbedrede termoelektriske egenskaber. Proceduren er en modifikation af den konventionelle citrat nitrat sol–gel-metode, hvor en auto-forbrændingsproces initieres under en kontrolleret termisk oxidations-reduktionsreaktion. Denne syntese producerer morfologisk og kompositorisk homogenitet og fine veldefinerede partikelstørrelser. Under bestemte SPS forarbejdningsbetingelser kan der fremstilles $Ca_3Co_4O_{9+\delta}$ med en gavnlig overfladestruktur og høj densitet.

Introduktion af udefrakommende elementer via dotering kan have en stor indflydelse på de termoelektriske egenskaber. Enkelt Fe-doterede og Fe/Y co-doterede $Ca_3Co_4O_{9+\delta}$ prøver blev syntetiseret vha. den nyudviklede auto-forbrændingsproces med derpå følgende SPS under tilpassede forarbejdningsbetingelser. Den resulterende effekt af Fe og Fe/Y defekterne i $Ca_3Co_4O_{9+\delta}$ på de termoelektriske egenskaber ved høj temperatur (fra stuetemperatur til 800 ℃) er blevet undersøgt og diskuteret. Fe-substitution på Co-gitterpladserne reducerer den elektriske

resistivitet (ρ), mens Seebeck koefficienten kun påvirkes lidt. Ca^{2+} substitueret med Y medfører en stigning i Seebeck koefficienten, men også i den elektriske resistivitet. Med en passende mængde Fe co-dotering blev stigningen i den elektriske resistivitet kompenseret, og sammen med den forbedrede Seebeck koefficient medførte tilføjelsen af Fe en forøgelse af den samlede termoelektriske ydeevne.

Som ved den ovenfor nævnte fremgangsmåde blev en yderligere undersøgelse foretaget, hvor $Ca_3Co_4O_{9+\delta}$ blev doteret med den sjældne jordart Ce, for at undersøge effekten på de termoelektriske egenskaber ved høj temperatur. Ved auto-forbrændingsprocessen efterfulgt af SPS behandlingen, udviste $Ca_{3-x}Ce_xCo_4O_{9+\delta}$ øget elektrisk resistivitet og Seebeck-koefficient ved stigende Ce doping over hele det målte temperaturinterval, mens varmeledningsevnen i planen (κ) kun var lidt påvirket. Eftersom introduktionen af Ce medfører et lille fald i power faktoren (*PF*), men også en reduktion af varmeledningsevnen, hvilket betyder at figur-of-merit (*ZT*) værdierne kommer til at ligne dem for de u-doterede $Ca_3Co_4O_{9+\delta}$, kan ZT øges ved dotering med sjældne jordarter og overgangs-metal (f.eks. Ce og Fe) co-dotering af $Ca_3Co_4O_{9+\delta}$ ved afkobling af de ellers indbyrdes afhængige elektroniske og termiske transport egenskaber.

Contents

Acknowledgement

Three years just like a fleeting month, and I did not believe there could be joy in doing research until being here. This memory would live with me forever just like the scar on my face which, coincidently, was the start of this delightful and marvelous three-year trip.

I would like to thank the people who ever helped me and encouraged me. Without any of you, this thesis would never be done. Prof. Søren Linderoth, Prof. Nini Pryds and Dr. Ngo Van Nong, I deeply thank you for believing in my competence and bringing me here. I would embed in my mind every single scene from the first minute after meeting you all. The great freedom you granted me is the essence of every single word here.

Tim Holgate and Li Han, you are not only my dearest colleagues but also my closest friends. With your advice I can quickly catch the core of thermoelectric and explore the beauty of it. The kind encouragement from Ebtisam Abdellahi I still clearly remember, probably you would never believe the fact that more than a hundred samples relied on it.

Scientific terms and equations themselves could never knit such an unforgettable experience. Cordially, I thank the people who ever smiled at me; to me, here is like a family, and you as brothers and sisters really warm my heart. Regina Bulatova, Kawai Kwok, Xiao Tang, Jing Shao, Anita Voss, Dennis Christensen, Sune Veltzé, Dan Eriksen, YunZhong Chen, Zhao Yue, Ali Sarhadi, Angela Zhang, DeWei Ni, Benoit Charlas, Dino Boccaccini, Felix Trier, Hoang Ngan Pham and Thanh Hung Le…thank you for all the jokes and conversations. Every cup of coffee we ever drank together is not just a beverage but also a piece of beautiful memory. I apologize to the lovely Lauren Holgate, Dan Song and adorable Isaac Holgate for my three-year game "an un-expected friend"; I am always warmly welcomed while suddenly showing up in front of your door. In the following summers, I will definitely recall Nini´s yearly barbecue and the time we played the Danish Viking game.

Denmark, if you are not around, would never be the happiest country in the world. I will never erase memories about every single corner and event we have ever walked and participated in. I especially acknowledge the sponsorship from the Danish Council for Strategic Research for making it possible for me to accomplishing my ideas.

Thanks my lovely mother, brother and friends in Taiwan, even though I am in a distant country where the winter is colder and longer. With your constant support I never feel lonely but closer than ever.

After eight years I move forwards again on academics and wish your dream has been carried out, to my dearest and most respectful father.

List of Publications

Peer-review Papers

1. **NingYu Wu**, Ngo Van Nong, Nini Pryds and Søren Linderoth

"**Effects of Y and Fe co-dopants on High Temperature Thermoelectric Properties in $Ca_3Co_4O_{9+\delta}$,**" manuscript submitted to "*Journal of Alloys and Compounds*", Oct. 2014.

2. **NingYu Wu**, Ngo Van Nong, Nini Pryds and Søren Linderoth

"**High Temperature Thermoelectric Properties of Ce doped $Ca_3Co_4O_{9+\delta}$,**" manuscript in preparation, Sept. 2014.

3. Tim C. Holgate, Li Han, **NingYu Wu**, Ngo Van Nong and Nini Pryds

"**Effects of Conducting Oxide Barrier Layers on the Stability of Crofer® 22 APU/$Ca_3Co_4O_9$ Interfaces**," *J. Mater. Res.*, in press, Sept. 2014.

4. **NingYu Wu**, Tim C. Holgate, Ngo Van Nong, Nini Pryds and Søren Linderoth

"**High Temperature Thermoelectric Properties of $Ca_3Co_4O_{9+\delta}$ by Auto-combustion Synthesis and Spark Plasma Sintering**," *J. Eur. Ceram. Soc.*, vol. 34, no. 4, pp. 925–931, Apr. 2014.

5. Tim C. Holgate, Li Han, **NingYu Wu**, Espen D. Bøjesen, Mogens Christensen, Bo B. Iversen, Ngo Van Nong and Nini Pryds

"**Characterization of the Interface between an Fe–Cr Alloy and the p-type Thermoelectric Oxide $Ca_3Co_4O_9$**," *J Alloy Compd.*, vol. 582, pp. 827–833, Jan. 2014.

6. **NingYu Wu**, Tim C. Holgate, Ngo Van Nong, Nini Pryds and Søren Linderoth

"**Effects of Synthesis and Spark Plasma Sintering Conditions on the Thermoelectric Properties of $Ca_3Co_4O_{9+\delta}$,**" *J. Electron. Mater.*, vol. 42, no. 7, pp. 2134–2142, Apr. 2013.

7. Tim C. Holgate, **NingYu Wu**, Martin Søndergaard, Bo B. Iversen, Ngo Van Nong and Nini Pryds

"**Kinetics, Stability, and Thermal Contact Resistance of Nickel–$Ca_3Co_4O_9$ Interfaces Formed by Spark Plasma Sintering**," *J. Electron. Mater.*, vol. 42, no. 7, pp. 1661–1668, Jul. 2013.

Conference Presentations

1. **NingYu Wu**, Ngo Van Nong, Nini Pryds, Søren Linderoth

"**High Temperature Thermoelectric Properties of Y and Fe co-dopants in $Ca_3Co_4O_{9+\delta}$ by Auto-combustion Synthesis and Spark Plasma Sintering**"

Part of "Proceedings of the 11th European Conference", 2014.
Presented at "11th European Conference on Thermoelectrics", 2013, The Netherlands (Oral).

2. **NingYu Wu**, Tim C. Holgate, Ngo Van Nong, Nini Pryds, and Søren Linderoth

"**High Temperature Thermoelectric Properties of $Ca_3Co_4O_{9+\delta}$ by Auto-combustion Synthesis and Spark Plasma Sintering**"

Presented at "TEP-CH 2013: Synthesis and Function of Thermoelectric Materials", 2013, Switzerland (Oral).

3. **NingYu Wu**, Tim C. Holgate, Ngo Van Nong, Nini Pryds, and Søren Linderoth

"**Effects of Synthesis and Processing on the Thermoelectric Properties of $Ca_3Co_4O_{9+\delta}$**"

Part of "Proceedings of the 31st International and 10th European Conference on Thermoelectrics", 2012.
Presented at "31st International & 10th European Conference on Thermoelectrics", 2012, Denmark (Oral).

List of Figures

Chapter 1

Introduction

In the 21st century, energy and environmental issues have become the biggest challenges for the human society due to the gradually elevating energy cost and the global warming associated with the fossil fuels. Green energies, such as the well-known photovoltaics, wind energy and biomass, have been developed for decades as alternative energy sources to meet the increasing energy demand associated with the process of civilization. These technologies have provided human beings an undeniable route to diminish the greenhouse gas emissions and their impact on the environment [1]–[4].

Among green energies, thermoelectric (TE) energy conversion arouses a great deal of interest since the ability to directly convert the thermal energy associated with a temperature gradient into electrical energy and vice versa. As a means of power generation, electricity is able to be extracted from heat sources, which is known as the "Seebeck effect". On the contrary, with the external electrical energy input, the phenomena called the "Peltier effect" can be used for creating temperature gradient for cooling or heating purposes [5][6]. The devices using TE materials possess many advantages such as solid-state operation, maintenance-free operation, and reliability due to the absence of moving parts and chemical reactions involved. These make TE devices particularly suitable for applications where the repairs would be difficult or impossible, for instance in space or remote terrestrial applications [7][8]. The Mars rover "Curiosity" is powered by a radioisotope thermoelectric generator (RTG) which converts the heat released by naturally decaying plutonium dioxide into electricity. Similar devices can also be found in Cassini and Galileo spacecrafts [9]–[11]. Additionally, a TE generator can be used in waste heat recovery to supply auxiliary power to improve an overall system efficiency, such as applications on vehicles or in factories to recover exhaust or industrial waste heat [12]–[15].

The major limits for broadening TE applications are the low energy conversion efficiency and high capital cost, which make TE technology inadequate to replace their conventional counterparts. The voltage that arises from a temperature difference across a material divided by the magnitude of that temperature gradient is called the Seebeck coefficient. In order to maximize the thermoelectric voltage for a given temperature gradient, a large Seebeck coefficient (S) is preferred. Also, in order to be able to efficiently serve as an electrical power

source, a high electrical conductivity (σ) is desired to maximize the output current through minimizing the internal resistance. In order to maintain the temperature gradient, the thermal conductivity (κ) should be low. Together with the above three intrinsic physical properties, the dimensionless figure-of-merit, *ZT*, is usually used to evaluate the performance of a TE material and is given as

$$ZT = (\frac{\sigma \cdot S^2}{\kappa}) \cdot T \,, \tag{1.1}$$

where *T* is the absolute temperature [16]. The larger the *ZT* value, the more efficiently the TE material converts energy [17][18]. Despite immense efforts having been made towards the development of TE materials with larger *ZT* value, high material and processing cost and complex fabrication methods still greatly limit the practical use and commercialization. Therefore, to explore and research materials of high efficiency with low cost and simple fabrication methods is an important focus within current thermoelectric research.

In this chapter, the fundamental thermoelectric effects, applications, properties and an overview of the current research progress will be introduced and discussed.

1.1 Thermoelectric Effects

The mechanism of the conversion between thermal energy and electrical energy is based on the thermoelectric effect. The thermoelectric effect is a generic term including three defined thermodynamically reversible effects, namely the Seebeck effect, Peltier effect and Thomson effect. Sometimes the thermoelectric effect may be referred to as the Peltier–Seebeck effect.

1.1.1 Seebeck Effect

In 1821, Baltic German physicist Thomas Johann Seebeck noticed a deflected compass needle when it was brought near a loop consisting of two dissimilar metals with junctions at different temperatures [19]. Seebeck recognized this was caused by magnetism induced by the temperature difference and called the phenomenon the thermomagnetic effect. Danish physicist Hans Christian Ørsted afterwards realized the thermomagnetic force was induced by an electric current and gave the term "thermoelectricity". As shown in Fig. 1.1, today it is known as the “Seebeck effect”.

In a closed loop with junctions at different temperature, there would be an electric current. In other words, in an open circuit with the temperature difference at two junctions an electrical potential difference (voltage, ΔV_{out}) at the two terminals would build up, as illustrated in Fig.

1.2. Within the limited temperature difference (ΔT), the developed thermoelectric voltage is proportional to the temperature difference and the linear relation is given as

$$S_{AB} = \frac{\Delta V_{out}}{\Delta T}, \tag{1.2}$$

where the proportionality constant S_{AB} is called the "relative Seebeck coefficient" between two materials A and B in the circuit and is expressed in units of $\mathrm{V/K}$ or $\mathrm{V/°C}$ (commonly $\mu\mathrm{V/K}$ or $\mu\mathrm{V/°C}$) [20].

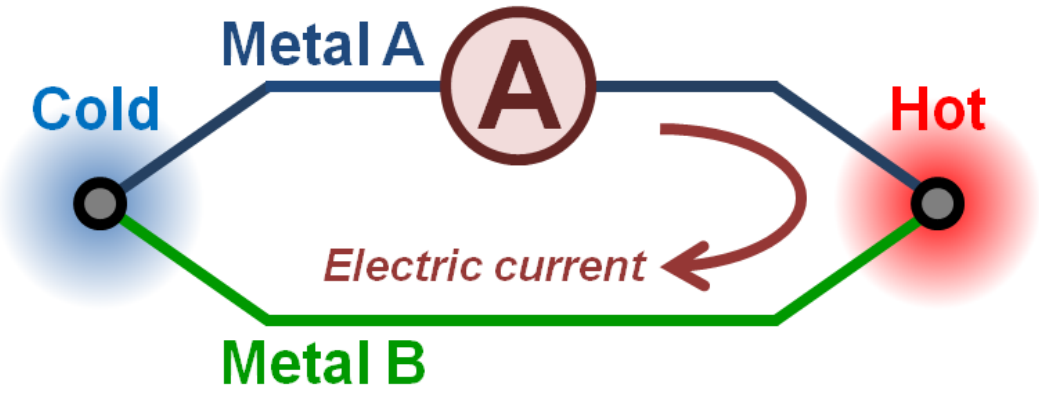

Fig. 1.1. The scheme of the Seebeck effect.

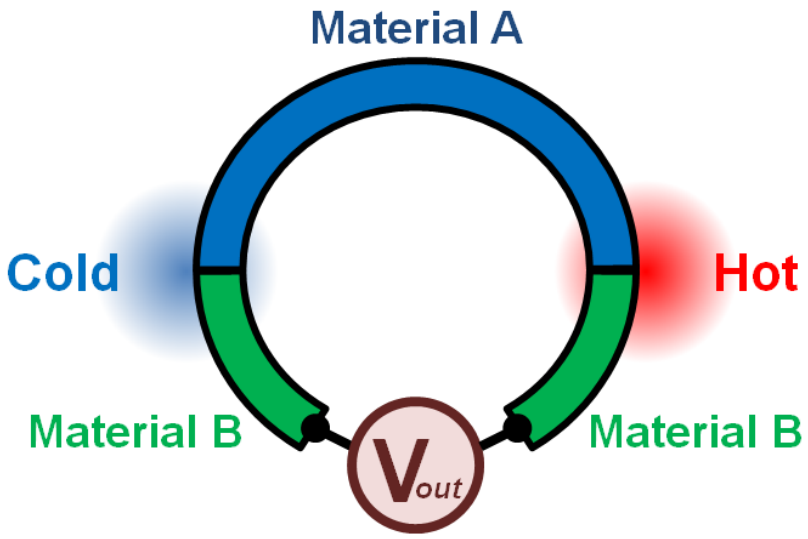

Fig. 1.2. The Seebeck effect in an open circuit.

The Seebeck effect can also occur in a single material. Similar to the condition mentioned above, a material subjected to a temperature gradient would build up a thermoelectric voltage (V) at two ends of the material, as illustrated in Fig. 1.3. If the temperature difference (ΔT) between the two ends is small, the Seebeck coefficient of this material is given as

$$S = -\frac{\Delta V}{\Delta T}, \tag{1.3}$$

where ΔV is the thermoelectric voltage between the two ends and S is the Seebeck coefficient of the material, which is also measured in units of $\mathrm{V/K}$ or $\mathrm{V/^{\circ}C}$. Thus with Eq. 1.3, Eq. 1.2 can be written as

$$S_{AB} = S_B - S_A = \frac{\Delta V_A}{\Delta T} - \frac{\Delta V_B}{\Delta T}, \tag{1.4}$$

S_A and S_B are the absolute Seebeck coefficients of the material A and B; which are intrinsic properties depending on the nature of materials.

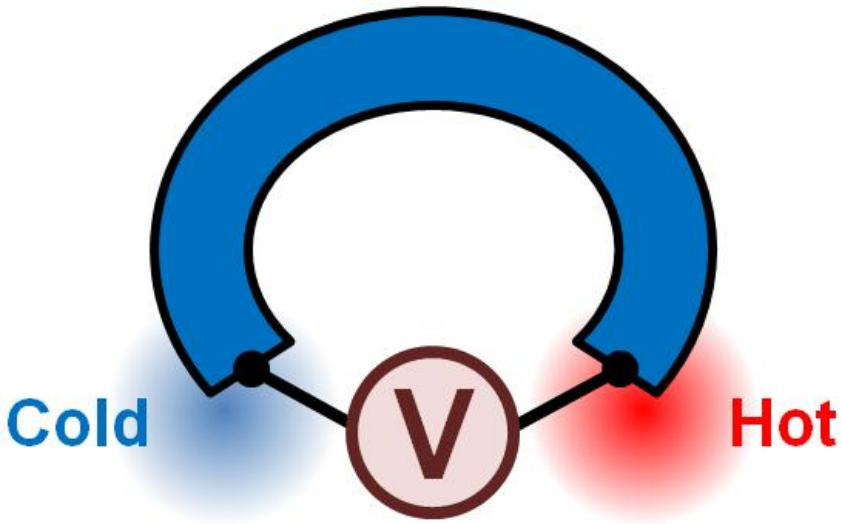

Fig. 1.3. The Seebeck effect in the sole material.

A Seebeck coefficient can be positive or negative. While positive, the higher temperature end is with the lower voltage and two directions of the temperature and thermoelectric voltage gradients are opposite. The sign of the Seebeck coefficient is generally governed by the dominant charge carrier (holes or electrons); therefore it is positive in a p-type semiconductor

and negative in a n-type semiconductor. The Seebeck coefficient is often referred to as the thermopower but to avoid the confusion, the term "Seebeck coefficient (*S*)" would be used in the following text.

1.1.2 Peltier Effect

The Peltier effect was discovered in 1834 and is named after French physicist Jean Charles Athanase Peltier [21]. In a closed loop formed with two dissimilar materials with an applied electric current, heat may be generated at one junction but removed at another, in other words, it may result in heating and cooling at the junctions as shown in the schematic of Fig. 1.4. When the direction of the electric current is reverse, the opposite heat flow would be observed accordingly, thus the junction can behave as a heater or cooler. The heat generated or removed at the junction is proportional to the electric current (*I*) and the relation can be given as

$$\dot{Q} = (\Pi_A - \Pi_B) \cdot I \,, \tag{1.5}$$

where $\dot{Q}$ is the heat generation or removal rate and Π_A and Π_B are the material dependent Peltier coefficients of the materials *A* and *B*. The Peltier effect is complimentary to the Seebeck effect since the thermal energy (heat) is transferred by the electrical energy in the former, however in the later the thermal energy drives the electrical energy.

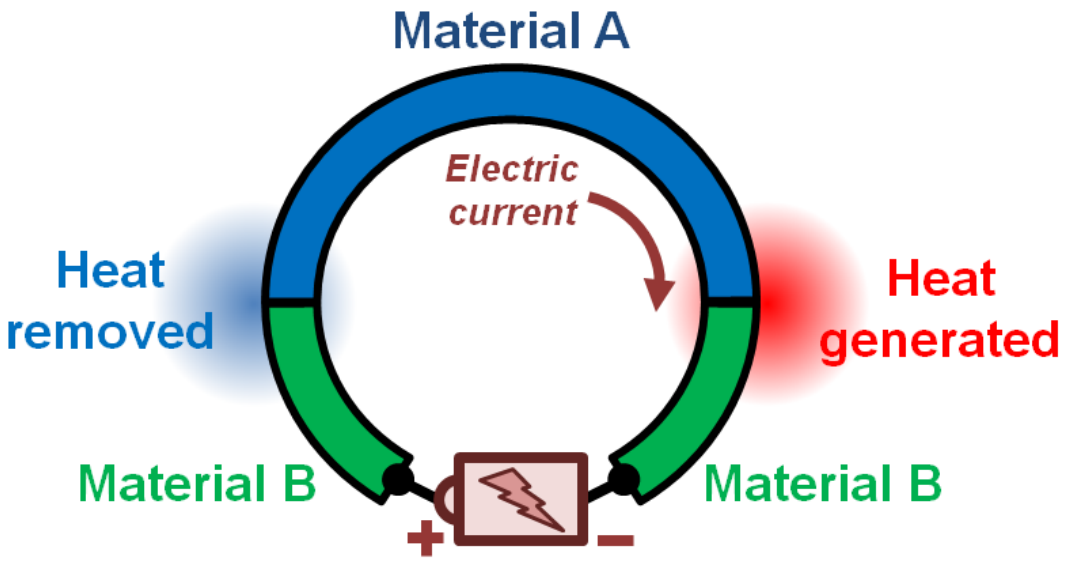

Fig. 1.4. The scheme of the Peltier effect.

1.1.3 Thomson Effect

Nearly 20 years later, the correlation between the Seebeck and Peltier effects was noted by William Thomson (Lord Kelvin) which is known as the Kelvin Relations and subsequently the Thomson effect was predicted and observed [22][23]. While a temperature gradient is applied in a material at the same time with the existence of an electric current, heat would either be absorbed by the material or released from it. The absorbed or released heat is proportional to the electric current (I) and the temperature gradient (∇T), which can be calculated as

$$\dot{q} = \tau \cdot I \cdot \nabla T \,, \tag{1.6}$$

in which $\dot{q}$ is the heat absorption or release rate and τ is the Thomson coefficient. With the electric current flowing towards the hot side and a positive temperature gradient, a positive Thomson coefficient means the material absorbs heat, as illustrated in Fig. 1.5.

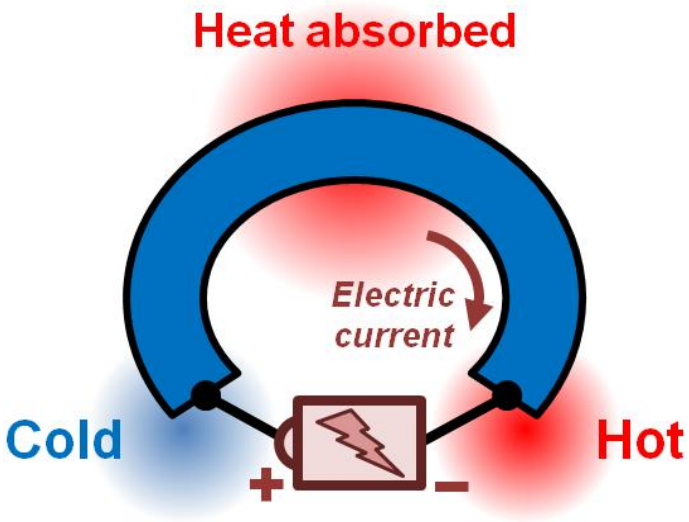

Fig. 1.5. With a positive Thomson efficient, the given temperature gradient and electric current, a material absorbs heat.

1.2 Functions of Thermoelectric Effects

The most popular and classic TE application is a thermocouple. The thermocouple is a device used to measure temperature and it consists of two dissimilar conductors joined together at one end with their other ends (the thermocouple leads) isothermally in contact but electrical insulated from each other. While the temperature difference builds between the junction (at the

temperature to be measured) and the ends of the leads (held at a known reference temperature), a differential voltage is produced and the unknown temperature can be determined. This is a demonstration of the aforementioned Seebeck effect as the thermocouple voltage arises because of a difference in the Seebeck coefficients of the dissimilar conductors (Fig. 1.2).

From a macroscopic perspective, the Seebeck and Peltier effects provide a means to convert electrical energy to thermal energy and vice-versa. As the schemes shown in Fig. 1.6, a TE generator consists of n- and p-type semiconductors which are electrically connected in series and thermally in parallel. By applying a heat source on one side and a heat sink on another to build a temperature difference, positive and negative charges (holes and electrons) in the semiconductors flow toward the cold side and electrical energy is developed based on the Seebeck effect. On the contrary, with the same construction an applied electrical current will pump heat from one side to the other via the Peltier effect. Either as a power generator or a cooler, no moving parts or chemical reactions are involved in the process. Therefore, TE devices are ideal to be used in the applications which require durability and reliability. Additionally, TE devices are scalable. By connecting n- and p-type semiconductors (as illustrated in Fig. 1.6, also called a unicouple) electrically in series and thermally in parallel, a TE module (as shown in Fig. 1.7) is able to provide a specific amount of electrical or cooling power on demand.

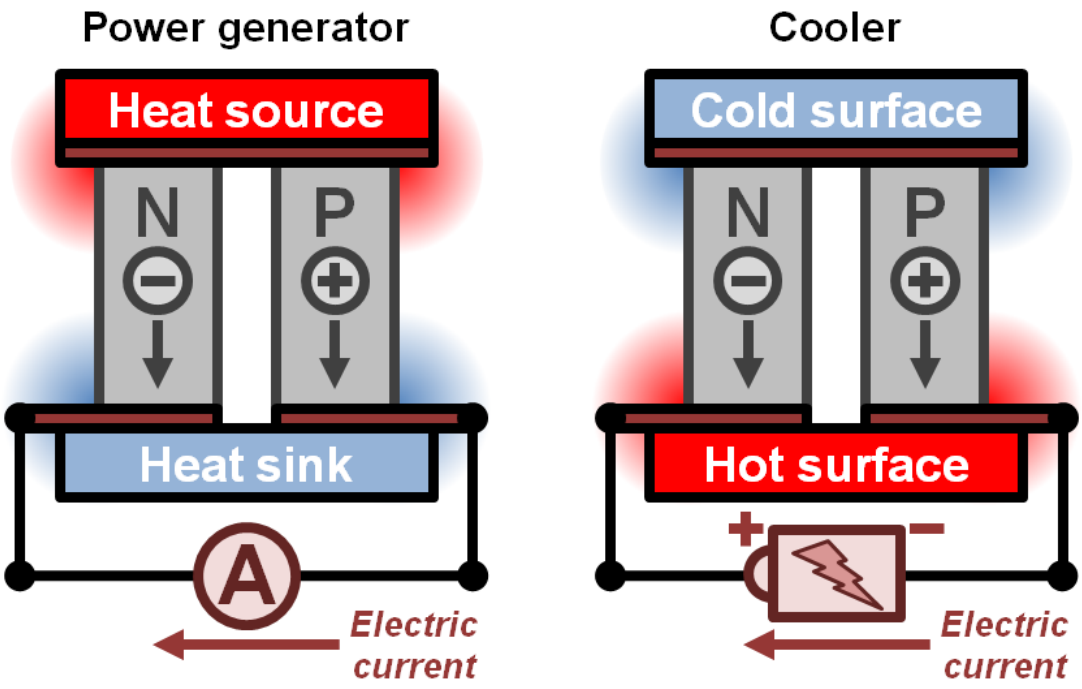

Fig. 1.6. The schemes of a TE power generator (left) and cooler (right).

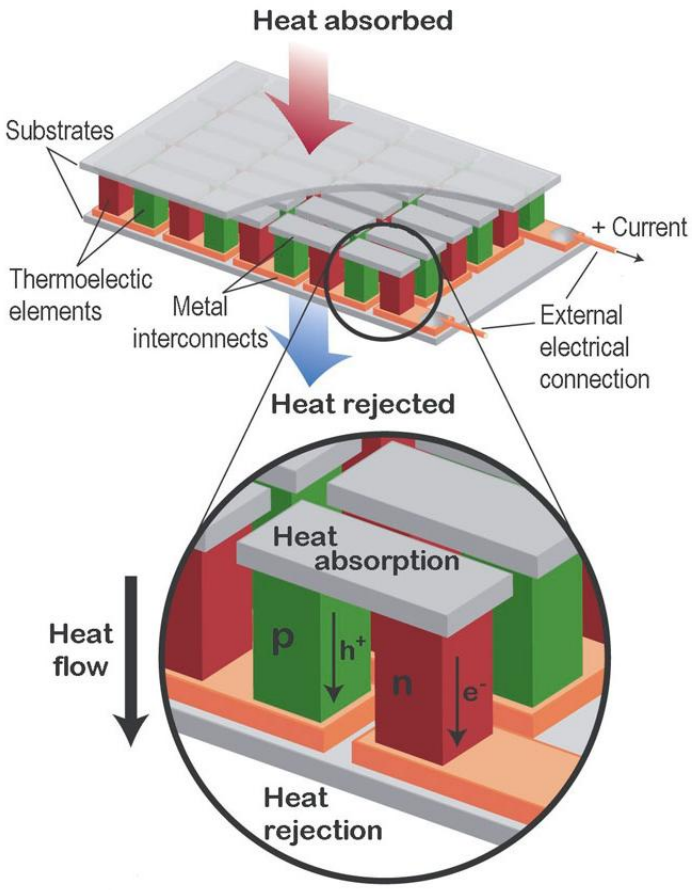

Fig. 1.7. TE power generation module (top) contains many unicouples (bottom, same as the scheme in Fig. 1.6) which are connected electrically in series and thermally in parallel [24].

In two publications during the period from 1909 to 1911, German physicist Edmund Altenkirch established a theory for the maximum efficiency of a TE power generator and cooler [25][26]. Today it is simply known as the dimensionless figure-of-merit, *ZT* (Eq. 1.1). It indicates a good TE material should possess high electrical conductivity, large Seebeck coefficient and low thermal conductivity. Since these three properties are correlated, to improve one of them may often lead to an offset from another, constraining the enhancement in *ZT*. Fig. 1.8 illustrates the dependence of these properties on carrier concentration [24]. It is clear that the electrical conductivity and Seebeck coefficient are related inversely. For instance, metals normally possess high carrier concentration with high electrical conductivity, but small Seebeck coefficient and high thermal conductivity leading to poor *ZT* values. The reciprocal relation also can be noticed between the electrical conductivity and thermal conductivity. Due to the fact that a part of thermal energy is conducted by charge carriers, a material with high carrier concentration is not only beneficial to the electrical conductivity but also to the thermal

conductivity, resulting in thermal insulators not being suitable for TE applications even though they exhibit very low thermal conductivity because they have also poor electrical conductivity. TE materials with the optimal *ZT* values, therefore, are typically heavily doped semiconductors with the carrier concentration between 10^{19} and 10^{21} carriers per cm^3. The details regarding the TE properties, the electrical conductivity, Seebeck coefficient and thermal conductivity are discussed later in this chapter.

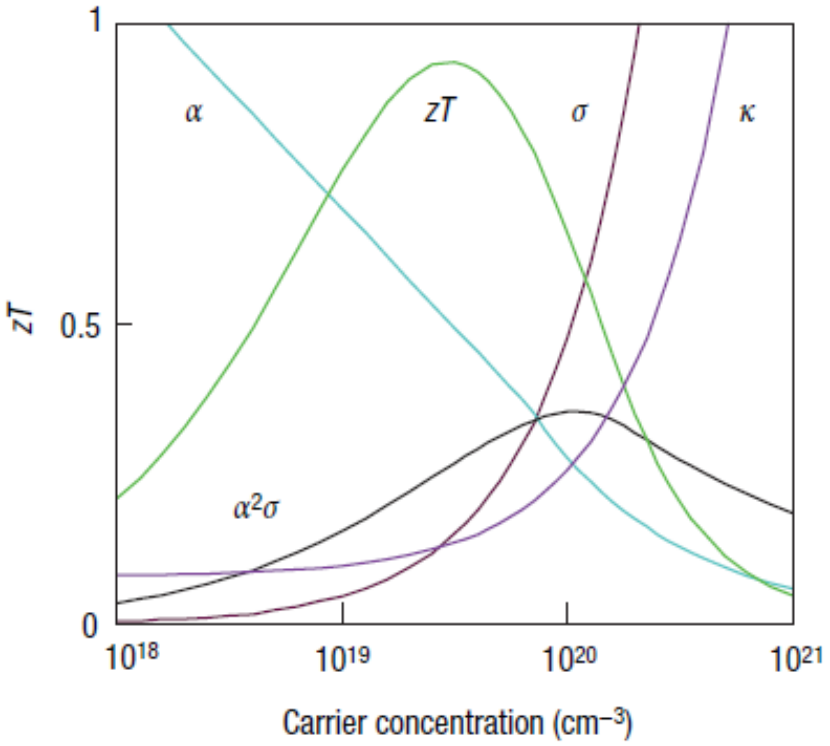

Fig. 1.8. The maximum of *ZT* involves compromised thermal conductivity (κ, plotted on the y-axis from 0 to a top value of 10 $W/m{\cdot}K$) and Seebeck coefficient (α or *S*, 0–500 $\mu V/K$) with electrical conductivity (σ, 0–5000 $1/\Omega{\cdot}cm$) [24].

The materials with larger *ZT* values may be expected to contribute more enhancement of the energy conversion efficiency in applications. For a TE power generator, the maximum efficiency (η) is expressed by

$$\eta = \frac{\Delta T}{T_h} \cdot \frac{\sqrt{1+Z_D\bar{T}}-1}{\sqrt{1+Z_D\bar{T}}+\frac{T_c}{T_h}}, \tag{1.7}$$

where T_h and T_c are the hot and cold side temperatures respectively; ΔT and $\bar{T}$ are the temperature difference and the average temperature of the hot and cold sides [27]. Care should be taken that $Z_D\bar{T}$ is the device figure-of-merit ($Z_D\bar{T}$ is used to distinguish "the device *ZT*" from "the material *ZT*"), in which the intrinsic properties of both TE materials in the device are involved. From Eq. 1.7, the efficiency for a power generator clearly depends on other device factors except the material *ZT*. It mainly stems from the fact that the material *ZT* includes temperature dependant properties (α, S, κ) and those differ from each material (n- and p-type) in a device. If those properties are assumed temperature independent and are identical in all constituent TE materials in a device, Z_D equates the material Z in Eq. 1.7 [27]. Similar to all heat engines, the efficiency limit of a TE power generation corresponds to the Carnot efficiency ($\Delta T/T_h$, the first term in Eq. 7). With the given condition $T_h = 1100$ K and $T_c = 500$ K, the conversion efficiency (η) can be plotted as a function of $Z_D\bar{T}$ as shown in Fig. 1.9. The conversion efficiency increases with $Z_D\bar{T}$ indicating that maximizing the device $Z_D\bar{T}$ values is necessitated for the optimal energy conversion performance.

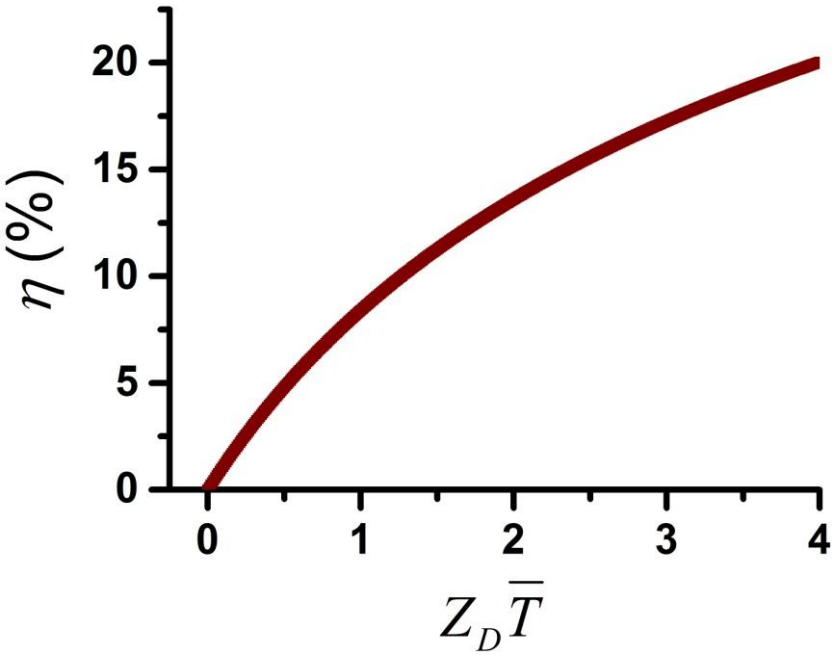

Fig. 1.9. The calculated conversion efficiency (η) as a function of $Z_D\bar{T}$ with $T_h = 1100$ K and $T_c = 500$ K according to Eq. 1.7.

1.3 Thermoelectric Properties

1.3.1 Electrical Conductivity (σ) and Resistivity (ρ)

Since current must pass through the TE elements in order for a TE generator to provide electrical power, the electrical conductivity or resistivity is an important material-dependant TE property. The electrical conductivity is the reciprocal of electrical resistivity and which is determined by the ability of a material to conduct electrical current; in other words, a material with high electrical conductivity (low resistivity) indicates the readily electric charge movement is allowed in it. With the Drude model [28][29], the electrical conductivity can be expressed as

$$\sigma = \frac{n \cdot q^2 \cdot \tau}{m^*}, \tag{1.8}$$

where n is the carrier concentration and τ is the mean-free-time between scattering events during the carrier conduction; q is carrier charge ($+e$ for "hole" and $-e$ for "electron") and m^* stands for the carrier effective mass. The electrical conductivity is always positive irrespective of either hole or electron carriers in a material, and is also usually a function of temperature. In a metal with a perfect lattice, an electron will conduct without any ionic collisions (i.e., τ is infinite). The finite electrical conductivity for metals mainly results from the thermal motion of ions to scatter electrons, and the impurities leading to an imperfect lattice. As a result of the thermal motion, the electrical conductivity of pure metals decreases with the elevated temperature.

Semiconductors possess the electrical conductivity between metals and insulators. With increasing temperature, the electrical conductivity increases in contrast to metals, and for which the changes in the carrier concentration and mean free time are responsible. Similar to metals, the carrier mean free time decreases with elevating temperature in semiconductors, however, the increase in the carrier concentration with temperatures overwhelms the drop in the carrier mean free time and results in the increased electrical conductivity [30].

To alter the electrical properties in semiconductors, doping is an effective manner as it directly influences the carrier concentration. Through doping, dopant atoms are intentionally introduced into an intrinsic (pure) semiconductor as either donors or acceptors to vary the carrier concentration. Depending on the dominant carrier concentration, a doped semiconductor with electron carriers is classified as a n-type semiconductor, or with hole carriers as a p-type semiconductor [30]. Since the TE current responding to an applied temperature gradient in n- and p-type semiconductors points to the opposite direction, a pair of two type materials is essential for consistent current flow in the construction of a TE device (as seen in Fig. 1.6 and 1.7).

1.3.2 Seebeck Coefficient (S)

In the Seebeck effect, a material with a temperature difference applied at two ends results in an electrical potential difference (voltage) between these two ends, thus the expression of the Seebeck coefficient is given by Eq. 1.3. It is noteworthy that the voltage built up in the sole material is not able to be measured simply by a voltmeter since the Seebeck effect simultaneously occurs in the external measurement materials (leads for a voltmeter) and contributes an additional voltage (as seen in Fig. 1.2). The measured net voltage leads to the relative Seebeck coefficient as expressed in Eq. 1.2. Technically, with a small temperature difference, the electric current density (J) occurs within the material can be expressed by

$$J = \sigma(-\nabla V) + \sigma \cdot V_T(-\nabla T) = \sigma(-E - V_T \cdot \nabla T), \tag{1.9}$$

where ∇V and ∇T are the voltage and temperature gradients respectively; σ is the electric conductivity [31]. The first term is the current density contributed from the voltage built up by the accumulated charges, and the second term describes the current density driven by the temperature gradients (V_T is the voltage as a function of the temperature difference). These currents flow in opposite directions. The scheme for a metal with electron carriers in this case can be seen in Fig. 1.10. If the equilibrium is reached and the temperature difference is maintained, no electric current flows. Thus Eq. 9 is given with $J = 0$ as

$$\sigma(-\nabla V_s - V_T \cdot \nabla T) = 0, \tag{1.10}$$

where ∇V_s is the electric field generated by the Seebeck effect. The Seebeck coefficient (S) is then determined as

$$-\nabla V_s = S \cdot \nabla T, \; S = V_T. \tag{1.11}$$

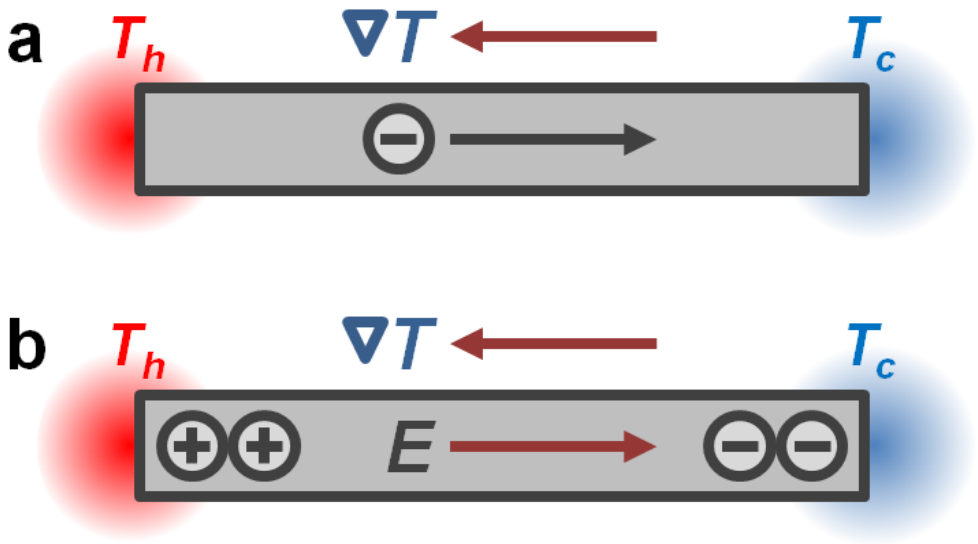

Fig. 1.10. The scheme of the Seebeck effect in the sole metal with electron carriers. (a) The electrons with higher energy at the hot side migrate toward the cold side. The electron current points to the cold side. (b) With the accumulated charges at two ends, the internal electric field (E) applies a force on electrons to migrate toward the hot side. The flows of the electrons in (a) and (b) are opposite.

The Seebeck coefficient can be positive or negative, and is related inversely with the electrical conductivity as mentioned. To have an insight into it, a simple situation can be considered; assume a free electron one-dimensional (1D) system with the uniform distribution of free electrons and impurities as scattering sites. In addition, a temperature gradient is applied and assumed as

$$T(x+\Delta x) > T(x)\,. \tag{1.12}$$

In this simple system, a free electron with the effective mass m and charge $-e$ behaves as an ideal gas and the average electron energy (ε) is only a function of temperature: $\varepsilon = \varepsilon(T)$. As described in Eq. 1.9, the electric current density driven by the temperature difference can be expressed as

$$j = -\sigma \cdot V_T \cdot \nabla T = (-e) \cdot n \cdot \upsilon\,, \tag{1.13}$$

where n is the electron density in this case and υ is the average drift velocity of electrons. The average drift velocity depends on the average electron energy thus it is given by

$$\upsilon\big[n, T(x)\big] - \upsilon\big[n, T(x+\Delta x)\big] = -\frac{\partial \upsilon(n,T)}{\partial T} \cdot \frac{\partial T}{\partial x} \cdot \Delta x\,. \tag{1.14}$$

Clearly both diffusion and thermal conduction are involved in above. For simplicity, the electron density (n) is assumed constant with position and time. As the assumption of the uniform electron and impurities distributions in the system, Δx can be a constant mean free path (l) and written as

$$l = \upsilon \cdot \tau = \Delta x\,. \tag{1.15}$$

Using Eq. 1.13 to 1.15, the local net electric current density (j_{net}) toward the hot side is given as

$$j_{net} = j\big[T(x)\big] - j\big[T(x+\Delta x)\big] = (-e) \cdot n \cdot \left(-\frac{\partial \upsilon(T)}{\partial T} \cdot \frac{\partial T}{\partial x} \cdot l\right) = -\sigma \cdot V_T \cdot \frac{\partial T}{\partial x}\,. \tag{1.16}$$

Then with Eq. 1.15,

$$V_T = \frac{(-e)\cdot n}{\sigma}\cdot\frac{\partial\upsilon(T)}{\partial T}\cdot\upsilon\cdot\tau\,. \tag{1.17}$$

With the Drude model as given in Eq. 1.8 for the electric conductivity and the definition of the Seebeck coefficient as expressed in Eq. 1.11, Eq. 1.17 can be expressed as

$$\begin{aligned} S = V_T &= \frac{1}{(-e)}\cdot m\cdot\frac{\partial\upsilon(T)}{\partial T}\cdot\upsilon \\ &= \frac{1}{(-e)}\cdot\frac{m}{2}\cdot\frac{\partial\upsilon^2}{\partial T} = \frac{1}{(-e)}\cdot\frac{\partial}{\partial T}(\frac{1}{2}m\upsilon^2)\,, \\ &= \frac{1}{(-e)}\cdot\frac{\partial\varepsilon}{\partial T} = \frac{1}{(-e)}\cdot\frac{C}{n} \end{aligned} \tag{1.18}$$

where C is the heat capacity of the material. The Seebeck coefficient is inversely proportional to the carrier concentration (n, electron concentration in this case), and varies in a reciprocal manner with the electric conductivity according to the Drude model. A material with electron as a carrier leads to the negative Seebeck coefficient, as shown in this case; on the contrary, positive for a hole-conducting material.

In Eq. 1.18, the basic relationship between the Seebeck coefficient, carrier concentration and carrier charge is given. For more accurate expression and prediction, the Mott formula is often used and is given as [32]

$$S(T) = \frac{\pi^2\cdot k_B^2\cdot T}{3q}\cdot\left.\frac{d\ln[\sigma(E)]}{dE}\right|_{E=E_F}, \tag{1.19}$$

where q is the carrier charge and k_B is the Boltzmann constant; $\sigma(E)$ is the electric conductivity contributed from electrons with the energy E and E_F is the Fermi energy. By using the relation $\sigma = n\cdot q\cdot\mu$ into Eq. 1.19, the modified Mott formula is known as [33]

$$S(T) = \frac{C_e}{n} + \frac{\pi^2\cdot k_B^2\cdot T}{3q}\cdot\left.\frac{d\ln[\mu(E)]}{dE}\right|_{E=E_F}; \tag{1.20}$$

$\mu(E)$ is the energy dependant mobility and C_e is the electronic specific heat. From Eq. 1.19 and 1.20, the relationship between S, n, q and σ can also be found as concluded from Eq. 1.18. The Mott formula is mainly used to predict the Seebeck coefficient of a weakly correlated metal at low temperature. It expresses the Seebeck coefficient is contributed from the energy dependant density of state (DOS), carrier drift velocity and relaxation time of the Fermi surface. However, due to the use of the independent single particle DOS, the Mott formula is generally not

applicable for semiconductors, superlattices and strongly correlated materials such as cobalt oxides.

To overcome the weakness of the Mott formula on strongly correlated systems, the interactions between electrons have to be taken into consideration, especially for transition metal oxides due to the non-negligible 3*d* orbital overlapping amplitude between atoms; the Coulomb repulsion appears and exerts influence on the electron conduction occurring in the same atomic orbital. Based on the Hubbard model [34], effects of the strong electron correlation on the Seebeck coefficient have been studied and the importance of the spin degeneracy has been indicated [35]–[39]. The Mott formula is derived from the Kubo formula [40], which is given as

$$S(T)=\frac{1}{T}\cdot\frac{\int_0^{\infty}dt\int_0^{\beta}d\tau\left\langle \hat{J}_x^E(t-i\tau)\hat{J}_x(0)\right\rangle}{\int_0^{\infty}dt\int_0^{\beta}d\tau\left\langle \hat{J}_x(t-i\tau)\hat{J}_x(0)\right\rangle}-\frac{\mu(T)}{qT}, \tag{1.21}$$

where q is the carrier charge, $\mu(T)$ is the temperature dependant chemical potential and β equates $1/(k_B\cdot T)$; $\hat{J}_x^E$ and $\hat{J}_x$ are the energy flux and charge current operators respectively. At high temperature β is close to zero and two operators become constant, thus the first term in Eq. 1.21 goes to zero and can be thrown out. The high-temperature limit of the Seebeck coefficient is approximately dependant on the chemical potential, which according to the definition is given as

$$\frac{\mu(T)}{T}=-\left(\frac{\partial s}{\partial N}\right)_{E,V}, \tag{1.22}$$

where *s* is the entropy of the system and *N* is the number of particles; *E* and *V* are the internal energy and volume. Then the entropy can be expressed in terms of microstates by

$$s=k_B\ln g, \tag{1.23}$$

where *g* stands for microstates, meaning the degeneracy in the system. With Eq. 1.23, Eq. 1.22 is written as

$$\frac{\mu(T)}{T}=-k_B\cdot\left(\frac{\partial\ln g}{\partial N}\right)_{E,V}, \tag{1.24}$$

and the Seebeck coefficient from Eq. 1.21 can be expressed as

$$S(T\to\infty)=-\frac{\mu(T)}{qT}=\frac{k_B}{q}\cdot\frac{\partial\ln g}{\partial N}, \tag{1.25}$$

which is a justifiable approximation only at high temperature. In Eq. 1.25, the Seebeck coefficient is expressed as the entropy transport per carrier.

By the Hubbard model, the strong electron correlation can be introduced into the expression of the Seebeck coefficient in terms of the degeneracy. For simplicity, the one-dimensional (1D) case with the on-site repulsion resulting from the Coulomb repulsion between electrons at the same atomic orbital is considered, and the Hubbard Hamiltonian is written as

$$H = -t \cdot \sum_{i,\sigma} \left(C_{i,\sigma}^{\dagger} C_{i+1,\sigma} + C_{i+1,\sigma}^{\dagger} C_{i,\sigma} \right) + U \cdot \sum_{i,\sigma} n_{i\sigma} n_{i-\sigma} \,, \tag{1.26}$$

where t is the hopping integral which represents the kinetic energy of electrons hopping between atoms, and U is the on-site Coulomb repulsion; $C_{i,\sigma}^{\dagger}$ and $C_{i,\sigma}$ are, respectively, the electron spin (σ) creation and destruction operators on site i; $n_{i\sigma}$ is the number operator for spin. Clearly this Hamiltonian includes the electronic kinetic energy and the on-site Coulomb interaction. At high temperature, $t, U \ll k_B T$, for a system with the uniform and random distribution of N_A sites and N electrons, spin-up and spin-down electrons randomly locate among sites N_A and each site is able to be occupied doubly. The degeneracy can be expressed as

$$g = \sum_{N_{\uparrow}}^{N} \left(\frac{N_A!}{N_{\uparrow}!(N_A - N_{\uparrow})!} \cdot \frac{N_A!}{N_{\downarrow}!(N_A - N_{\downarrow})!} \right), \; N = N_{\uparrow} + N_{\downarrow} \,. \tag{1.27}$$

After using Stirlings approximation, the Seebeck coefficient for the condition $t, U \ll k_B T$ is given by

$$S(T \to \infty) = \frac{k_B}{(-e)} \cdot \ln\left[\frac{(2-\rho)}{\rho} \right], \tag{1.28}$$

where ρ denotes the ratio of electrons to sites ($\rho = N/N_A$) and $q = (-e)$ since the negative charge of a electron. Eq. 1.28 is the generalized Heikes formula which is derived from the Hubbard model with the excluded on-site Coulomb repulsion [41]. For the case $t \ll k_B T \ll U$ in the same system, the on-site repulsion (U) should be taken into account; therefore, the configuration of a site which is occupied by two electrons with parallel or opposite spins is forbidden. Then the degeneracy is given as

$$g = 2^N \cdot \frac{N_A!}{N!(N_A - N)!}, \tag{1.29}$$

leading to the Seebeck coefficient being expressed as

$$S(T \to \infty) = \frac{k_B}{(-e)} \cdot \ln\left[\frac{2(1-\rho)}{\rho}\right]. \tag{1.30}$$

The difference between Eq. 1.28 and Eq. 1.30 stems from the strong electron correlation.

By the description for the Seebeck coefficient at high temperatures in a strongly correlated system, Eq. 1.30 can be further extended and used for cobalt oxides, such as Na_xCoO_2 and $Ca_3Co_4O_{9+\delta}$ [38][39]. In these materials, the oxidation state of the Co ions is mixed between 3+ and 4+. Consequently two configurations of Co ions, Co^{3+} and Co^{4+} are involved in the degeneracy, and are defined as g_3 and g_4 for Co^{3+} and Co^{4+}, respectively. The values of g_3 and g_4 depend on the Hund's rule and the crystal-field splitting between t_{2g} and e_g orbitals together with the temperature [38][42]. While the temperature is sufficiently high, the total number of configurations is given as

$$g = g_3^{N_A - M} \cdot g_4^{M} \cdot \frac{N_A!}{M!(N_A - M)!}, \tag{1.31}$$

where M is the number of Co^{4+} sites and $N_A!/[M!\,(N_A - M)!]$ signifies the number of the Co^{3+} and Co^{4+} site configurations. Using the Eq. 1.31, the Seebeck coefficient of a cobalt oxide can be expressed as

$$S(T \to \infty) = \frac{k_B}{(-e)} \cdot \ln\left(\frac{g_3}{g_4} \cdot \frac{x}{1-x}\right),\ x = \frac{M}{N_A}, \tag{1.32}$$

where x is the concentration of Co^{4+}. The spin states for Co^{3+} and Co^{4+} in this case can be considered as low- (LS), intermediate- (IS) and high-spin (HS) which are close to each other in energy owing to the relatively small gap between t_{2g} and e_g, as shown in Fig. 1.11. In cobalt oxides, the degeneracy ratio g_3/g_4 not only affects the value but also the sign of the Seebeck coefficient, as does the concentration x.

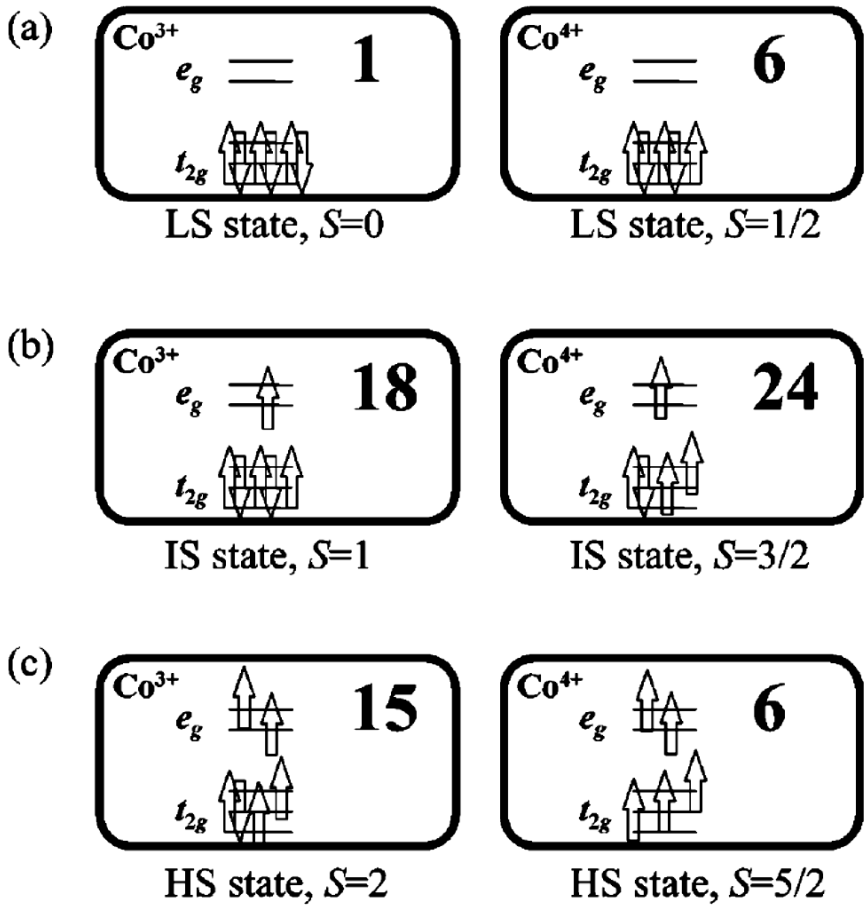

Fig. 1.11. The scheme of Co^{3+} and Co^{4+} ions states: low-spin state (a), intermediate-spin state (b) and high-spin state (c) in cobalt oxides. The lines signify the energy states of t_{2g} and e_g. The arrows represent for electron spins. S is the magnitude of the spin and the number in each frame stands for the degeneracy g_3 or g_4 [38].

$Ca_3Co_4O_{9+\delta}$ is a p-type layered material containing CoO_2 layers in which the hole carrier conduction takes place (details are referred to later in this chapter). Since the CoO_2 layer is highly hole doped and consists of Co^{3+} and Co^{4+} ions, the fact of a mixed Co oxidation state of +3.5 in which results in $x = 0.5$ [39]. In addition, both Co^{3+} and Co^{4+} ions in CoO_2 layers generally are in the low-spin state (LS) for the un-doped $Ca_3Co_4O_{9+\delta}$. Applying Eq. 1.32 with $x = 0.5$ and the ratio $g_3/g_4 = 1/6$, the high temperature limit of the Seebeck coefficient $S(T \to \infty) = 154\ \mu V/\mathrm{K}$ is obtained for the un-doped $Ca_3Co_4O_{9+\delta}$ and which is close to the experimental observations [43][44].

1.3.3 Thermal Conductivity (κ)

Heat in a material is conducted by carriers and phonons. Therefore, the total thermal conductivity (κ) is associated with the carrier thermal conductivity (κ_e) and the lattice thermal conductivity (κ_L), giving the relationship as $\kappa = \kappa_e + \kappa_L$. In a metal, having a high carrier (electron) concentration, the thermal conductivity is dominated by the carrier component. The metal which is the best electrical conductor is the best thermal conductor as well. In contrast, the heat conduction in an insulator is phononic and the lattice contribution accounts for the total thermal conductivity. Since the carrier is involved in the heat transfer as well as the electric conduction, with the Wiedemann–Franz law, the ratio of the electronic thermal conductivity (κ_e) to the electrical conductivity (σ) of a metal is given as

$$\frac{\kappa_e}{\sigma} = L_0 \cdot T \tag{1.33}$$

where the ratio is proportional to the temperature by a constant of proportionality L_0, which is the Lorenz number and equal to

$$L_0 = \frac{\pi^2 \cdot k_B^2}{3e^2} = 2.44 \times 10^{-8} \left(\frac{\mathrm{W} \cdot \Omega}{\mathrm{K}^2} \right), \tag{33}$$

where k_B is the Boltzmann constant and e is the charge of an electron. Since the Wiedemann–Franz law is based on the mechanisms of the heat and electrical conduction involving free electrons, it is only valid for the metallic-like conduction. In a metal with the elevated temperature, the average electron velocity increases as well as the collisions between electrons and nuclei, resulting in the increasing electronic thermal conductivity since the enhanced energy transport. In contrast, the electrical conductivity simultaneously decreases as the collisions divert the electrons from forward charge transport.

The Wiedmann–Franz law expresses the prohibition of the simultaneous increase in the electrical conductivity and the depression in the electronic thermal conductivity. Any attempt to improve electrical conductivity leads an offset in electronic component of the total thermal conductivity, causing a challenge for enhancing material *ZT* as shown in Fig. 1.8. In this regard, materials with the thermal conductivity dominated by the lattice contribution are of interests as TE materials since the electrical conductivity is able to be preserved while attempting to the lower thermal conductivity through various techniques (alloying, nanostructuring, etc.). For semiconductors and semimetals, the carrier and lattice contributions to the total thermal conductivity are on the same order [45]. To reduce the lattice thermal conductivity by introducing complex crystal structures is an effective approach since it can interfere with phonon transport [46][47]. For example, $Ca_3Co_4O_{9+\delta}$ possesses a misfit-layered structure where the misfit between layers is expected to hinder the heat conduction in the cross-plane direction. The

existence of imperfections and defects in materials, including additional inclusions and extra grain boundaries, also aids for the lower lattice thermal conductivity [48]. Instead of the presence of the additions as above, doping with heavy and large atoms not only can introduce phonon scattering sites but also adjust the carrier concentration, providing a potential approach for *ZT* enhancement.

1.4 Current Research of Oxide Thermoelectric Materials

A vast and variety of materials has been implemented in TE applications, from metals and semiconductors to ceramics and polymers in categories of materials which consist of mono-, polycrystalline or nanocomposites, and existing as bulks, films, nanoscale wires and clusters. The majority of efforts in recent TE research on bulk materials is mainly focused on semiconductor alloys such as filled skutterudites [49][50], half-Heusler compounds [51], clathrates [52][53], and chalcogenides [54]–[56], in which a $ZT > 1$ has been realized. Via forming monocrystalline, superlattice and nanostructuring, some reports have shown that *ZT* values can be increased further by reducing the lattice thermal conductivity below the alloying limit [56]–[61]. Venkatasubramanian et al. by producing a Bi_2Te_3/Sb_2Te_3 superlattice has increased the device $Z_D\bar{T}$ value to 2.4 at 300 K [57]. Biswas et al. through introducing "all-scale hierarchical architectures" (from atomic-scale lattice disorder and nanoscale endotaxial precipitates to mesoscale grain boundaries) in PbTe successfully enhanced the *ZT* value up to 2.2 at 915 K [61]. Zhao et al. reported the unprecedented *ZT* value of 2.6 at 923 K in a SnSe single crystal suggesting that a simple compound possessing layered structures, anharmonic bonding and intrinsically low thermal conductivity can be a promising TE material in spite of the lack of nanostructuring.

In the high temperature region ($T > 800$ ℃), however, primary alloy systems hardly retain those aforementioned remarkable TE performance due to the increased lattice thermal conductivity leading to the inferior *ZT* values. Additionally, sensitivities of alloy materials to oxidation or sublimation when in air at high temperature as well as the presence of the toxic, naturally rare and expensive constituents are important concerns for practical uses and commercialization. Therefore, oxide TE materials consisting of earth abundant elements, being of relatively lower toxicity and produced through a simpler process have been considered as a candidate for high temperature TE applications in air owing to their thermal and chemical stabilities. With the discovery of single-crystal $NaCo_2O_4$ which possesses distinguished TE properties [62], and later the research work on $Ca_3Co_4O_{9+\delta}$ [63], metal oxides have garnered much interest and been widely studied. In this chapter, several representative oxide TE materials are introduced and discussed.

1.4.1 Layered Cobalt-based Oxide Materials

Typical p-type cobalt-based oxides for TE applications are based on alkali or alkaline metal cobaltates with layered structures as shown in Fig. 1.12 [64]. The charge conduction occurs within the CoO_2 layers while the electronic properties are subject to the variation in the cobalt ion valence and oxygen content [65]. The large Seebeck coefficient stems from the presence of the low-spin state of Co^{3+} as mentioned before (seen in Fig. 1.11) [38]. Additionally, the misfit between layers hinders the phonon transport resulting in lower thermal conductivity and suggests a great capability for TE applications. Na_xCoO_2 and $Ca_3Co_4O_{9+\delta}$ are two promising TE oxides in this class.

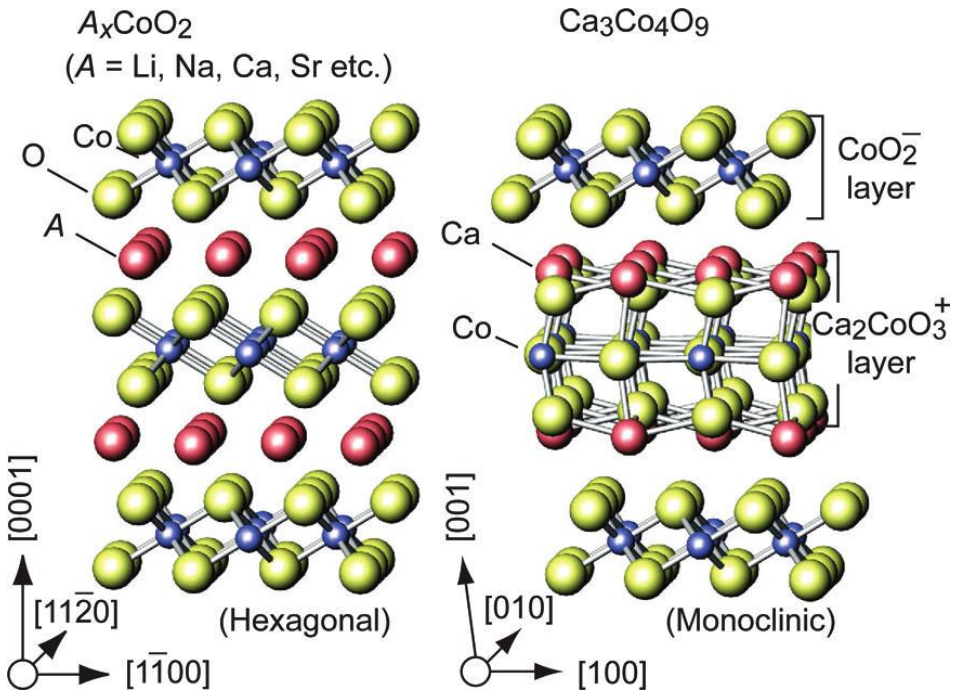

Fig. 1.12. Schematic illustrations of layered cobalt based oxide structures [64]. CoO_2 layers consisting of edge-shared CoO_6 octahedra exist in both A_xCoO_2 (left, A = Li, Na, Ca, Sr) and $Ca_3Co_4O_{9+\delta}$ (right).

1.4.1.1 $Ca_3Co_4O_{9+\delta}$

$Ca_3Co_4O_{9+\delta}$ possesses a misfit-layered structure with a CdI_2-type hexagonal CoO_2 subsystem and a rock salt-type Ca_2CoO_3 subsystem that are alternately stacked along the *c*-axis with identical *a, c* and β parameters but different and incommensurate *b* parameters. Therefore, this misfit-layered oxide can be described as $[Ca_2CoO_3][CoO_2]_{(b1/b2)}$ with a $b1$ to $b2$ ratio of approximately 1.62, where $b1$ to $b2$ are two lattice parameters for the rock salt and CoO_2

subsystems respectively [63][66]. Shikano et al. have reported a p-type single-crystalline $Ca_3Co_4O_{9+\delta}$ with a *ZT* value of 0.83 at 800 ℃ [67].

The methods to produce polycrystalline $Ca_3Co_4O_{9+\delta}$ are versatile and are commonly implemented due to the difficulty in single-crystalline sample preparation. Different $Ca_3Co_4O_{9+\delta}$ syntheses and consolidation processes result in the inferences on the consequent texturing and densification, further affecting the TE properties. Wu et al. reported that highly dense polycrystalline $Ca_3Co_4O_{9+\delta}$ can be obtained via a spark plasma sintering (SPS) processing [43]. With proper SPS conditions, the electrical conductivity may be enhanced. Due to the layered nature of the crystal structure, it is important to take into account the inherent anisotropy due to texturing when characterizing the TE properties of polycrystalline samples [43][44]. Improving the texturing leads to the increase in "in-plane" electrical conductivity and larger power factor, however, the thermal conductivity increases simultaneously since the loss of structural disorder. Particle size is another factor that affects texturing; with the same consolidation process, highly textured $Ca_3Co_4O_{9+\delta}$ can be obtained by smaller $Ca_3Co_4O_{9+\delta}$ particles prepared through wet-chemical reactions. Other than the TE properties, the consolidation process also exerts influence on the mechanic properties [68].

Doping and introducing impurities are commonly adopted for TE property improvement in addition to altering consolidation conditions. The rare-earth ions (La, Pr, Dy, Ho, Er, Yb and Lu) as substitutions at the Ca-site in the $Ca_3Co_4O_{9+\delta}$ system enhances the *ZT* values in high temperature region owing to the increase in the Seebeck coefficient and the decrease in the lattice thermal conductivity [69]–[71]. Nong et al. reported with Lu and Ag substitutions for Ca atom and the existence of Ag as nanoinclusions, the electrical conductivity and Seebeck coefficient can be elevated significantly; together with the decreased thermal conductivity, the highest *ZT* value of 0.6 at about 900 ℃ for poly-crystalline $Ca_3Co_4O_{9+\delta}$ to date has been achieve. Besides, along with the demonstration of the thermal stability, heavily doped $Ca_3Co_4O_{9+\delta}$ with metallic nanoinclusions has presented the potential for high temperature TE applications [70].

1.4.1.2 Na_xCoO_2

Metallic Na_xCoO_2 possesses large a Seebeck coefficient and is composed of a CoO_2 subsystem and a non-fully filled insulating sodium atoms layer [62]. The disorder of sodium atom occupancy leads to the phonon scattering and lower thermal conductivity. TE properties of Na_xCoO_2 are dominated by the sodium content and oxygen vacancy. Due to the difficulty in the control of sodium- and oxygen-vacancy concentration, the variation in the properties of Na_xCoO_2 is more considerable as compared with the variation in $Ca_3Co_4O_{9+\delta}$. The electrical conductivity as well as the Seebeck coefficient increase with the sodium content up to $x = 0.78$ [72]. While introducing oxygen vacancies, the reduction in carrier concentration occurs and leads to lower electrical conductivity and larger Seebeck coefficient; however, the consequent phonon scattering is depressed and the increase in the thermal conductivity results [73].

Partially substituting for cations is a general approach to improve the TE properties of Na_xCoO_2. By Ni doping at the Co-site in Na_xCoO_2, the particle size can be reduced to lower the thermal conductivity along with enhancing the Seebeck coefficient [74]. With Zn substitution for Co, both the electrical conductivity and the Seebeck coefficient are elevated [75]. The presence of Ag in Na_xCoO_2 as impurities has shown the increase in the electrical conductivity and Seebeck coefficient as well as the thermal conductivity, leading to a close to single-crystalline *ZT* value of 0.9 [76]. Generally, TE properties of Na_xCoO_2 are better than $Ca_3Co_4O_{9+\delta}$. However, Na_xCoO_2 easily decomposes by reacting with the water in air, and sodium ions are susceptible to sublimation at temperatures higher than 800 ℃ placing limits on its application [77].

1.4.2 Perovskite-type Oxide Materials

Perovskite-type oxides consist of a diverse group of composition with a general formula ABO_3. As seen in the schematic of the crystal structure shown in Fig. 1.13, *B* cations are surrounded by six oxygen ions forming BO_6 octahedra, and the *A* cation is located in the center of eight corner-shared BO_6 octahedra. Perovskite-type oxides are considered to be potential TE materials due to large Seebeck coefficients at high temperatures. Widespread research has been conducted on materials in this class of perovskite-type transition metal oxides, including two representative systems: $SrTiO_3$ and $CaMnO_3$.

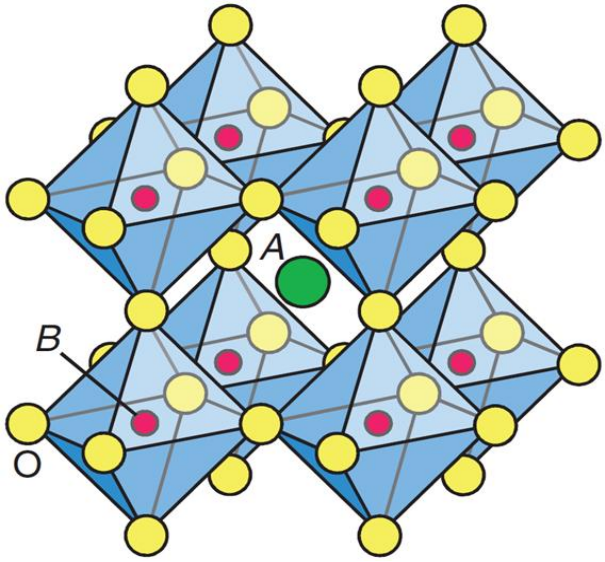

Fig. 1.13. Schematic crystal structure of perovskite-type oxide, ABO_3 [78]. *B* cations are surrounded by six oxygen ions and *A* cation locates in the center of eight corner-shared BO_6 octahedra.

1.4.2.1 $SrTiO_3$

As a n-type TE oxide, $SrTiO_3$ is thermally stable at high temperature and environmentally friendly. $SrTiO_3$ is able to be a good electronic conductor via doping with electron donors. The thermal conductivity in pure $SrTiO_3$ is dominated by the phonon conduction and the electronic contribution is negligible[79]. Through investigations of La doping at Sr-site or Nb doping at Ti-site in $SrTiO_3$ single crystals, the carrier scattering mechanism changes with the temperature; at about 470 ℃ from polar optical phonons/acoustic phonons coupled scattering to acoustic phonon scattering. The *ZT* values increase with the carrier concentration and La-doped $SrTiO_3$ with the largest carrier concentration exhibits a *ZT* value of 0.27 at 800 ℃ [79]. With the combustion synthesis and SPS processing, highly dense samples ($>$ 98 % theoretical density) can be obtained and TE properties are improved as compared with those synthesized by the conventional solid-state reaction (SSR) method; La-doped $SrTiO_3$ which is produced with the same processing reaches a maximum *ZT* value of 0.22 at about 500 ℃ [80].

The electrical conductivity and Seebeck coefficient are insensitive to the kind of rare-earth element doping at Sr-site in $SrTiO_3$, while the thermal conductivity varies strongly; among rare-earth elements, Dy doping results in the highest *ZT* values [81]. With increasing Dy doping concentration, the electrical conductivity and Seebeck coefficient are elevated; simultaneously the lattice thermal conductivity decreases and thus the *ZT* values are enhanced [82]. Other than single element doping, La/Dy co-doping with a proper concentration has been applied for improving electrical properties and a *ZT* value of 0.36 at about 800 ℃ can be obtained [83].

With doping, $SrTiO_3$ can from a superlattice Ruddlesden-Popper structure, expressed as $SrO(SrTiO_3)_n$ or $Sr_{n+1}Ti_nO_{3n+1}$, which is composed of perovskite-type $(SrTiO_3)_n$ block layers and rock salt SrO layers stacking along the *c*-axis, as shown in Fig. 1.14. The superlattice structure offers the mechanisms that are found in layered cobalt-based oxides for reducing thermal conductivity but also causes a decrease in the electrical conductivity [84]–[86]. The rare-earth element doping at the Sr-sites in $SrO(SrTiO_3)_n$ for $n = 2$ effectively improves the local symmetry of TiO_6 octahedra and further enhances the Seebeck coefficient, leading to a *ZT* value of 0.24 at about 730 ℃ found in $(Sr_{0.95}Gd_{0.05})_3Ti_2O_7$ [87]. However, the studies of $(Sr_{1-x}La_x)_{n+1}Ti_nO_{3n+1}$ for $n = 1$ and 2 reveals the larger *ZT* values for $n = 2$ than for $n = 1$; similar *ZT* values found in $(Sr_{1-x}Nd_x)_{n+1}Ti_nO_{3n+1}$ for $n = 1$ and 2 [88], suggesting that more SrO–$SrTiO_3$ interfaces (i.e., $n = 1$) and the layered structure are not as effective as shown to be in layered cobalt-based oxides for TE performance enhancement.

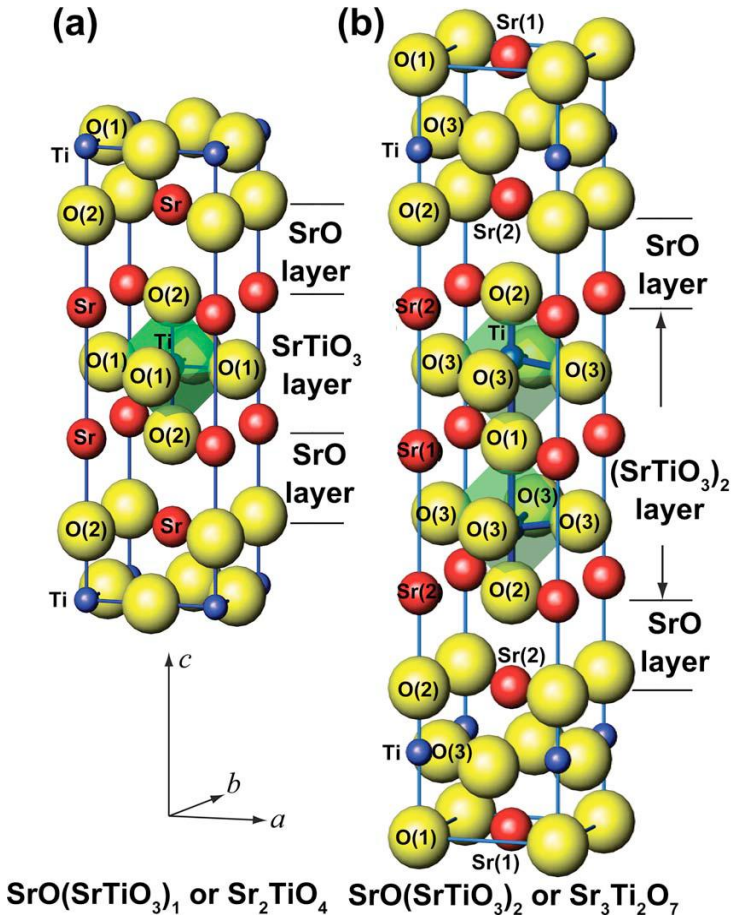

Fig. 1.14. Schematic illustrations of Ruddlesden-Popper crystal structures, $SrO(SrTiO_3)_n$ with $n = 1$ (a) and $n = 2$ (b) [84].

1.4.2.2 $CaMnO_3$

Another promising n-type oxide in this class is $CaMnO_3$, which possesses larger Seebeck coefficient and lower thermal conductivity; however a lower electrical conductivity stands as a barrier to TE applications. Similar to $SrTiO_3$, electron doping is a common approach for enhancing the TE properties and which can be applied on both Ca- and Mn-sites in $CaMnO_3$. By doping with diverse rare-earth elements at Ca-site, $Ca_{0.9}R_{0.1}MnO_3$ (R = La to Yb) exhibits adiabatic small polaron transport below 600 K but metallic-like conductivity at higher temperatures [89]. Similar carrier concentrations arrived at by rare-earth element doping is responsible for the insensitive Seebeck coefficient. However, the structural distortions and ionic mass difference between Ca^{2+} and R^{3+} influences the electrical conductivity and thermal conductivity, leading to the largest ZT value of 0.2 at about 730 ℃ found in R = Dy and Yb samples [89]. Compared to singly doped systems, Dy/Yb co-doped $CaMnO_3$ has shown larger

ZT values which is mainly attributed to the distortion of the electronic density of states together with the enhanced point-defect scattering, leading to a *ZT* value of 0.26 at about 730 ℃ in $Ca_{0.9}(Dy_{0.05}Yb_{0.05})MnO_3$ [90].

Besides doping, processing is also a factor in the enhancement of TE properties. By auto-combustion synthesis, the $CaMnO_3$ phase forms starting at 700 ℃ and completes by 900 ℃, which is much lower than the usual 1350 ℃ for solid-state reaction synthesis [91]. The morphology and grain size distribution of $CaMnO_3$ vary with calcination temperatures and the highest electrical conductivity can be extracted by calcining at 1000 ℃. The grain sizes of $CaMnO_3$ can be diminished to the nanoscale with co-precipitation synthesis [92]. Despite the slight decrease in the electrical conductivity with the shrinking grain size, the enhanced phonon scattering which is induced by a higher concentration of grain boundaries leads to the lower thermal conductivity and further the improvement in *ZT* values. Another route to smaller grains is ultrasonic spray combustion processing [93]. In this method the heat-treatment temperature for pure $CaMnO_3$ is lower as compared with other syntheses and thus smaller starting powder particle sizes can be retained during processing leading to smaller grain sizes. This leads to increases in density and in phonon scattering at the grain boundaries for exhibiting higher electrical conductivity and lower thermal conductivity, respectively.

1.4.3 Transparent Conductive Oxides

Transparent conductive oxides (TCOs) compose a class of materials with optical transparency and high electrical conductivity, being widely used in optoelectronic devices, such as displays, photovoltaics, gas sensors and thin-film resistors. Focuses in this class are mainly on ZnO, In_2O_3, SnO_2 and related oxides. From the point of view of the electrical conductivity and carrier mobility, transparent conductive oxides have potential for TE applications.

1.4.3.1 ZnO

Several features such as the stability, high melting point and high electrical properties prove ZnO to be a potential TE material, nevertheless high thermal conductivity is a central issue. Adequate n-type conduction can be realized in ZnO by doping and common dopants include Al, Ni, Ti and Ga. The electrical conductivity and Seebeck coefficient have been shown to benefit from the amount of 2 % Al addition; the Al induced decrease in the *c*/*a* ratio of the crystal structure, as well as the presence of secondary phases at the grain boundaries, are responsible for resulting in a *ZT* value of 0.3 at 1000 ℃ [94][95]. Grain size is a crucial factor in manipulating the electrical conductivity and thermal conductivity; the samples with larger grains have shown the larger *ZT* values [96].

Analogous to Al doping, the improvements in the electrical conductivity and Seebeck coefficient can be obtained with Ni substitution [97]; however, Ti additions increase the

electrical conductivity but cause a decrease in the Seebeck coefficient [98]. Other than single element doping, Ni or Ti as a co-dopant with Al are able to improve TE performance [99][100]. While Al and Ga are used in co-doped system, the improved Seebeck coefficient and reduced thermal conductivity, along with the slightly decreased electrical conductivity lead to a *ZT* value of 0.65 at about 975 ℃ [101].

SPS processing has been shown to enhance the Al doping amount into ZnO and results in the increased electrical conductivity [102]. Additionally, since Al doping is associated with the variation of the grain size, the combined effect of Al doping and grain refinement can be realized by a proper choice of the SPS condition and thus reduce the thermal conductivity. RF plasma processing provides a new approach to produce doped ZnO nanopowders and retain metallic electrical conductivity [103]. Al-containing ZnO composites consisting of nanoscale ZnO grains and $ZnAl_2O_4$ precipitates synthesized by the microwave-stimulated solvothermal synthesis exhibit approximate 20 times lower thermal conductivity at room temperature than ZnO without nanotructuring. Together with the retained electrical conductivity and Seebeck coefficient, a 50 % larger *ZT* value of 0.44 at about 730 ℃ than non-nanostructured ZnO has been demonstrated [104].

1.4.3.2 In_2O_3

In_2O_3 forms the cubic bixbyite-type crystal structure and is a weak n-type semiconductor. By extrinsic dopants, the carrier concentration and thus electrical conductivity can be strongly elevated. In addition to a low thermal conductivity, In_2O_3 is expected to be applied for TE applications.

Nanoscale Ge-doped In_2O_3 grains can be produced by citrate gel synthesis [105]. Since the effects of the electron doping and enhanced phonon scattering, a *ZT* value of 0.3 is achieved. Via a co-precipitation method and SPS processing, the average grain size of Zn/Ce co-doped In_2O_3 can be minimized to 10 nm and the nanostructures are able to be reserved [106]. With diminishing grain size, the electrical conductivity increases and thermal conductivity decreases; a *ZT* value of 0.4 at about 780 ℃ has been obtained in the 50 nm grained sample.

$(ZnO)_mIn_2O_3$ is an related compound with a layered structure, consisting of $InO_{1.5}$, $(Zn,In)O_{2.5}$ and ZnO layers alternately stacked along the *c*-axis. As a superlattice material, it shows a desirable low thermal conductivity and high carrier mobility; similar to layered cobalt based oxides, $(ZnO)_mIn_2O_3$ is suitable for TE applications. Equivalent atomic species have been utilized to introduce appropriate lattice distortion to suppress thermal conductivity and enhance the carrier mobility, thus improving TE performance [107]. Due to the anisotropic nature of layered structures, Y-doped $(ZnO)_5In_2O_3$ fabricated by the reactive-templated grain growth (RTGG) technique has shown that the elevated electrical conductivity, reduced thermal

conductivity while slightly lower Seebeck coefficient can be obtained by doping and enhancing the texturing, leading to a *ZT* value of 0.33 at 800 ℃ [108].

1.4.4 Other Oxide Materials

Other than the above discussed primary TE oxides, BiCuSeO is another promising p-type TE material with a layered structure that is composed by alternately stacking the conductive $(CuSe_2)^{2-}$ layer and insulating $(Bi_2O_2)^{2+}$ layer, as shown in Fig 1.15 [109]. It possesses low thermal conductivity and a variety of dopants for replacing Bi or Se to engineer the TE properties. With substituting Sr for Bi, the electrical conductivity increases and a *ZT* value of 0.76 at 600 ℃ is obtained despite the negative effects of the decreased Seebeck coefficient and increased thermal conductivity [110]. Heavy doping with Ba at Bi-site in BiCuSeO and refinement of the grain size have further enhanced TE properties and resulted in a larger *ZT* value of 1.1 at 650 ℃ [111]. The highly textured microstructure achieved by a hot-forging process has exhibited an increase in carrier mobility and thus enhanced the electrical conductivity, leading to a *ZT* value of about 1.4 at 650 ℃ for $Bi_{0.875}Ba_{0.125}CuSeO$ [112]. Introduction of Cu deficiencies can induce more carriers in the $(CuSe_2)^{2-}$ layers and elevates the electrical conductivity, along with high Seebeck coefficient and low thermal conductivity, realizing the *ZT* value improvement from 0.50 to 0.81 at 650 ℃ [109].

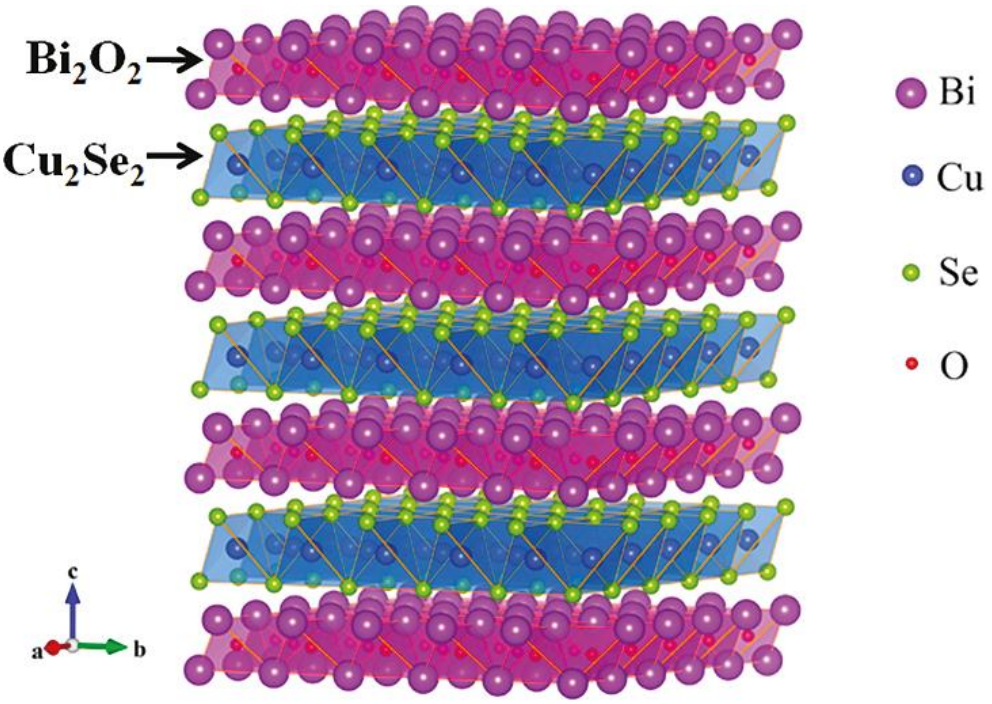

Fig. 1.15. Schematic crystal structure of BiCuSeO [109].

Bi_2O_2Se is a n-type TE oxide with low lattice thermal conductivity approaching the value of glass-like structures, showing a *ZT* value of about 0.2 at 530 ℃ [111]; through doping and structure tailoring, electrical properties are expected to increase. $LaCoO_3$ has exhibited a temperature dependant transition in the Seebeck coefficient, which shows the negative Seebeck coefficient in the range from room temperature to 180 ℃, but a positive value above 180 ℃ [113]. Substituting Ni into Co sites in $LaCoO_3$ can eliminate the transition and maintain the positive Seebeck coefficient. Improving the TE properties by doping can also be applied in $CuAlO_2$ [114]. Ag/Zn co-dopants can enhance the formation of the $CuAlO_2$ phase and thus elevate the electrical conductivity and Seebeck coefficient; however, with the sole Ag dopant or Ag/Ni co-dopants, the electrical conductivity decreases, leading to a *ZT* value of 0.016 at about 790 ℃ in $Cu_{0.979}Ag_{0.02}Zn_{0.001}AlO_2$.

1.5 Research Aim and Thesis Outline

The goal of this Ph.D. study is to develop a p-type TE oxide material with the sufficient and stable performance at high temperatures for power generating applications and which can be potentially incorporated in industrial processes. The scientific objective is to understand the effects of diverse dopants and different material processing methods on the high temperature thermoelectric properties of p-type materials.

The challenges to break through into widespread application of TE power generation lie in the economy of systems and their functionality. Scalable and practical applications, including commercialization based on the currently used materials are subjected to environmental and cost issues, and thus are difficult to be realized. Metal oxides have attracted much attention due to features such as natural abundance, environmental benignity and durability at high temperature in air. The research focuses on the misfit-layered cobaltate $Ca_3Co_4O_{9+\delta}$ which demonstrates significant potential for high temperature applications owing to its large positive Seebeck coefficient together with metallic-like electrical conductivity, and low thermal conductivity typical of a “phonon glass–electron crystal” [115].

Nong et al. have developed a p-type layered $Ca_3Co_4O_{9+\delta}$ polycrystalline with Lu and Ag substitutions for Ca and the existence of Ag as nanoclusions; by the conventional solid-state reaction method and subsequent SPS processing, it shows so far the largest *ZT* value of 0.6 at about 900 ℃ and provides an excellent matching to the n-type counterpart [70]. However, both Lu and Ag are expensive, which necessitates finding alternative cheaper solutions. On the basis of this knowledge, the research begins with the investigations of SPS conditions for solid-state reaction-fabricated $Ca_3Co_4O_{9+\delta}$, such as sintering temperatures, applied pressures and ramping rates, attempting to clarify processing effects by characterizing microstructure, phase purity and TE properties. For a bottom-up study, other than conventional solid-state reaction method, wet-

chemical synthesis accompanied with SPS processing is studied. Developing a new synthesis is also involved and expected to give a firm basis of pure $Ca_3Co_4O_{9+\delta}$ polycrystalline production for sequential approaches.

As introduced before, extrinsic doping is able to exert great influence on the TE properties. Additionally, co-doping has shown potential in other material systems. Sole Fe doping and Fe/Y co-doping are chosen in this research and the systematic investigation of the effects on the high temperature TE properties of $Ca_3Co_4O_{9+\delta}$ is given.

Rare-earth elements as dopants, for instance Lu, have been successfully incorporated into $Ca_3Co_4O_{9+\delta}$ and achieved the enhanced TE performance [69][70]. The investigation of Ce doping as new dopant in $Ca_3Co_4O_{9+\delta}$ aims to explore the effects on the high temperature TE properties and is expected to retain or surpass the desirable features as reported systems with other rare-earth element dopants.

The subsequent chapter 2 explains and discusses the experimental procedures and characterizations. The following four scientific chapters focus respectively on effects of the consolidation processing, synthesis methods, and strategies for enhanced of the thermoelectric properties by single and dual doping.

In chapter 3, the study of $Ca_3Co_4O_{9+\delta}$ syntheses by solid-state and sol–gel reactions, and the spark plasma sintering (SPS) processing with different conditions such as sintering temperatures, applied pressures and ramping rates is presented. With characterizations in respect to the microstructure, bulk density and thermoelectric transport properties, $Ca_3Co_4O_{9+\delta}$ synthesized by sol–gel reaction followed by the proper SPS processing is presented as a beneficial means of obtaining high-performance $Ca_3Co_4O_{9+\delta}$ owing to the resulting smaller particle sizes and better grain alignment.

The development of a rapid auto-combustion reaction for the synthesis of $Ca_3Co_4O_{9+\delta}$ powder is introduced in chapter 4. The procedure is a modification of the conventional citrate–nitrate sol–gel method where an auto-combustion process is initiated by a controlled thermal oxidation–reduction reaction. This synthesis produces morphological and compositional homogeneity, and fine, well-defined particle sizes. With determined ideal SPS processing conditions, highly dense and texturing $Ca_3Co_4O_{9+\delta}$ can be fabricated.

Fe-doped and Fe/Y co-doped $Ca_3Co_4O_{9+\delta}$ samples synthesized by the newly developed auto-combustion reaction and followed by the SPS processing with the effects of Fe and Fe/Y doping on the high temperature thermoelectric properties are investigated and discussed in chapter 5. The Fe substitution at the Co-sites effectively reduces the electrical resistivity (ρ) while the Seebeck coefficient (S) is influenced only slightly. Y substitution for Ca^{2+} leads to an increase in the Seebeck coefficient but also in the electrical resistivity. With proper additional Fe doping, the

rising electrical resistivity was compensated, together with the improved Seebeck coefficient leading to improved thermoelectric properties.

Chapter 6 introduces the effects of Ce doping in $Ca_3Co_4O_{9+\delta}$ on the high temperature TE properties. With the auto-combustion reaction synthesis followed by spark plasma sintering (SPS) processing, Ce-doped $Ca_3Co_4O_{9+\delta}$ exhibited an increased electrical resistivity (ρ) and Seebeck coefficient (S) with increasing Ce doping content over the whole measured temperature range, while the in-plane thermal conductivity (κ) was only slightly influenced. A slight decrease in the power factor (PF) but similar figure-of-merit ZT values to the un-doped $Ca_3Co_4O_{9+\delta}$ suggest potential for the Seebeck coefficient enhancement in a co-doped $Ca_3Co_4O_{9+\delta}$ system.

Chapter 2

Material Processing and Characterizations

In this research, polycrystalline $Ca_3Co_4O_{9+\delta}$ powders are synthesized by solid-state reaction and wet-chemical reactions, followed by spark plasma sintering (SPS) processing for consolidation. Subsequently, the phase identification and microstructural analysis are applied. To determine the TE properties, characterizations for the Seebeck coefficient (*S*), electrical resistivity (ρ) and thermal conductivity (κ) are employed. The general introductions of the $Ca_3Co_4O_{9+\delta}$ syntheses, SPS processing and properties characterizations are provided and discussed in the following text.

2.1 Syntheses of $Ca_3Co_4O_{9+\delta}$

The fabrication of pure or doped $Ca_3Co_4O_{9+\delta}$ powders is mainly followed one of two routes: solid-state reaction or wet-chemical synthesis. The advantages of the solid-state reaction are simplicity and high yield, but the purity and the homogeneity are two major issues of concern. By contrast, wet-chemical synthesis eliminates the drawbacks of the solid-state reaction by atomic scale mixing, but the low yield associated with this process limits the scalability. In this research, conventional citrate–nitrate sol–gel method which involves the chelation between citrate and the metal ions originating from dissolved metal nitrates is employed as one of wet-chemical syntheses. The new developed auto-combustion reaction is served as another wet-chemical synthesis which is a modification of the citrate–nitrate sol–gel method where an auto-combustion process is initiated by a controlled thermal oxidation–reduction reaction.

Solid-state reaction synthesis is achieved by using commercial $CaCO_3$ (99+ %) and Co_3O_4 (99.7 %) starting precursors. The precursors are mixed thoroughly in stoichiometric ratio followed by ball milling with an appropriate amount of ethanol for 48 h. The dried mixtures are then calcined in air at 900 ℃ for 24 h. For citrate–nitrate sol–gel method, a stoichiometric ratio of $Ca(NO3)_2{\cdot}4H_2O$ (99+ %) and $Co(NO_3)_2{\cdot}6H_2O$ (99+ %) are dissolved in aqueous citric acid solution. Following initial heating at 75 ℃ and drying of the gel at 120 ℃ in a vacuum muffle oven, the gel is further heat treated at 750 ℃ for 2 h for single phase $Ca_3Co_4O_{9+\delta}$.

Similar to citrate–nitrate sol–gel method, the auto-combustion reaction is carried out by a stoichiometric ratio of $Ca(NO_3)_2 \cdot 4H_2O$ (99+ %) and $Co(NO_3)_2 \cdot 6H_2O$ (99+ %) which is dissolved in distilled water with a specific amount of citric acid (99+ %) to keep the citrate–metal cation molar ratio at 1. Additionally, the citrate-to-nitrate molar ratio is maintained at 0.40 by introducing NH_4NO_3 (98+ %). After initially drying the gel while stirring continuously at 75 ℃ until a uniform viscous gel is obtained, the temperature is raised to about 250 ℃ to induce the auto-combustion process. The resulting powders are calcined at 750 ℃ for 2 h to obtain single phase $Ca_3Co_4O_{9+\delta}$. The detailed synthetic processes in this research can be found in each chapter.

2.2 Spark Plasma Sintering (SPS) Processing

Conventional hot pressing (HP) and hot isostatic pressing (HIP) are consolidation processing methods in steady state, which are carried out by an external heat source. The surface energy which is activated by the heat spontaneously induces the mass diffusion and grain boundary migration between particles, leading to the densification. Several advantages such as homogeneous structure, texturing and improved mechanical properties can be obtained by these processing methods; however, the grain coarsening resulting from remaining at high operation temperature for a long period is a crucial feature [116]. SPS processing is similar to HP but with different way of heat generation. A pulsed direct current (DC) generator is equipped in a SPS system, as seen in Fig. 2.1. The starting powders are put in a sintering die (a graphite die is used in this research) under a uniaxial pressure placed between two electrodes. During the sintering process, a pulsed DC is applied leading to an internal heat source caused by Joule heating, and plastic deformation is followed due to the external loading at elevated temperature. Due to the unique heating mechanism, the SPS process enables high degree of densification at lower sintering temperatures within a short period (e.g., typically in few minutes) as compared with other conventional sintering processing methods. Combining with the rapid heating (e.g., achieving heating rate up to 1000 ℃/min) and cooling (e.g., up to 300 ℃/min), the SPS process provides the capabilities to depress the grain growth and produce dense materials with controlled microstructures.

The SPS process used in this research is carried out by a Dr. Sinter SPS-515S system manufactured by Fuji Electronic Industrial Co., Ltd. with the capabilities of maximum pulsed current output 1500 A and sintering pressure 50 kN. Detailed SPS processing conditions used in this research depend on the actual experimental requirement and are showed in each chapter.

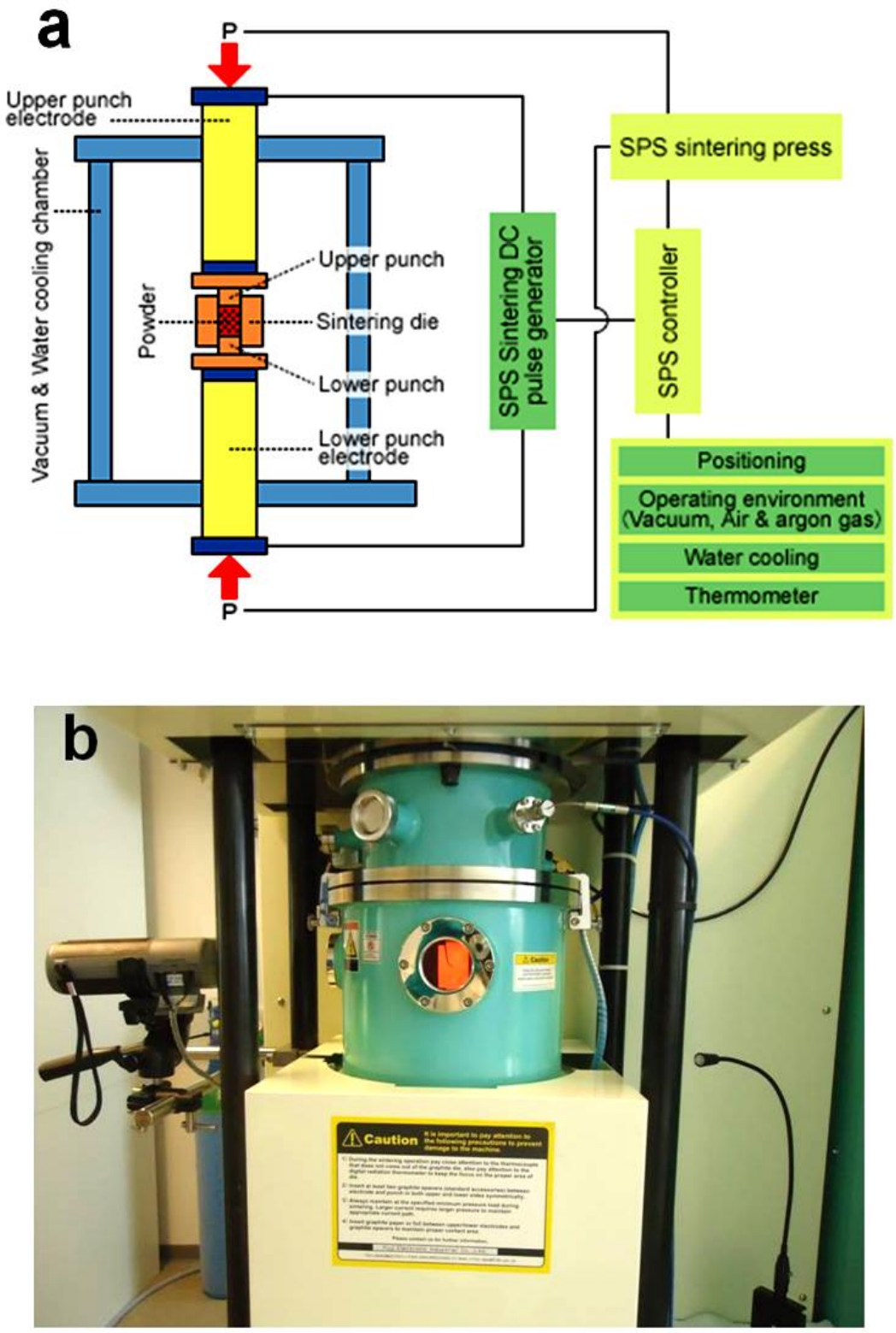

Fig. 2.1. The configuration of a spark plasma sintering system (a) [117], and the picture of the SPS system in Department of Energy Conversion and Storage, DTU (b).

2.3 Electrical Resistivity, Seebeck Coefficient and Thermal Conductivity Characterization

The electrical resistivity and Seebeck coefficient are obtained simultaneously with an ULVAC-RIKO ZEM3 under a low-pressure helium atmosphere. As the configuration shown in Fig. 2.2, the measurement is performed in a furnace and a specimen is held between two electrodes. With an applied constant current through the specimen, the electrical potential difference (voltage, ΔV) can be gauged by two identical thermocouple leads located aside, and thus the electrical resistivity can be determined. All electrical resistivity measurements shown in this research are averaged from four independent measurements at each measuring temperature.

With a temperature gradient provided by a local heater placed at the bottom electrode (as seen in Fig. 2.2(b)), an induced electrical potential difference and temperature difference (ΔT) is recorded with two thermocouples to give the Seebeck coefficient (i.e., $S = \Delta V/\Delta T$) as described in Eq. 1.2. The Seebeck coefficient from a ULVAC-RIKO ZEM3 is determined by the slope of the electrical potential difference versus the temperature difference (i.e., $S = dV/dT$). In this research, the electrical potential differences are extracted at three preset temperature differences to determine the Seebeck coefficient at each measuring temperature.

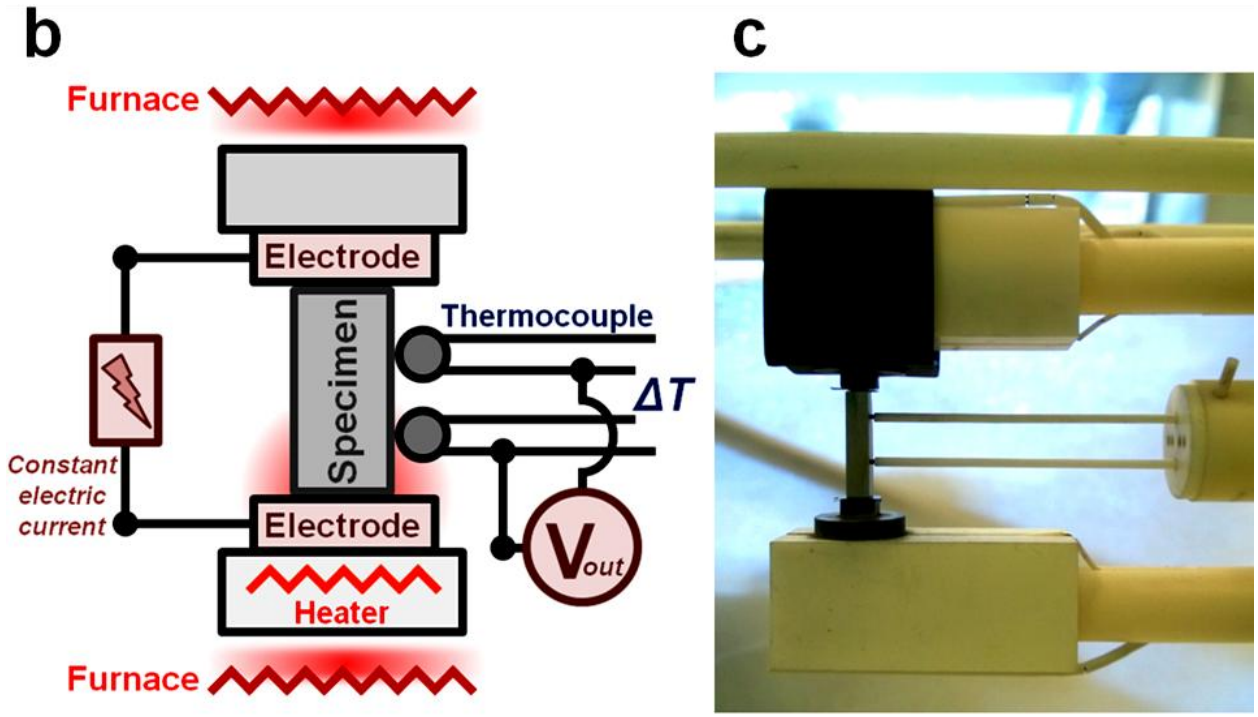

Fig. 2.2. The photo of the ULVAC-RIKO ZEM3 in Department of Energy Conversion and Storage, DTU (a); the schematic configuration of the system (b) and picture of the electrical resistivity and Seebeck coefficient measurements set up (c).

The thermal conductivity is calculated using the equation $\kappa = \rho \cdot \alpha \cdot c_p$, where ρ, α and c_p are the density, thermal diffusivity and specific heat capacity, respectively. The thermal diffusivity is obtained under vacuum in a NETZSCH LFA-457 laser flash system as an average of three measurements at each measuring temperature. The c_p is taken to be the temperature independent Dulong–Petit limit (e.g., 0.798 $J/g{\cdot}K$ for the pure (un-doped) $Ca_3Co_4O_{9+\delta}$). The bulk densities of the samples are measured by the Archimedes' method or using a Micromeritics AccuPyc 1340 gas pycnometer to calculate the density with an average of ten measurements. The theoretical density 4.68 g/cm^3 for the pure (un-doped) $Ca_3Co_4O_{9+\delta}$ is determined based on the lattice parameters reported by Masset et al. [63].

Due to the nature of $Ca_3Co_4O_{9+\delta}$ layered crystal structure, the anisotropy has been considered and special care has been taken in the specimen preparation and the measurements for accurate TE properties (ρ, S, κ). In order to assure each TE property with exactly the same processing history, samples to be measured were cut into small specimens along different directions as shown in Fig. 2.3 with dimension and direction depending on the type of characterizations. The expression "out-of-plane, $\parallel$" and "in-plane, $\perp$" are used to denote the properties measured along the directions parallel and perpendicular to the SPS pressure axis, respectively. Variations in the

TE properties (measurement error) taken from multiple samples remain below 1 % and which is taken into consideration in the comparison and discussion.

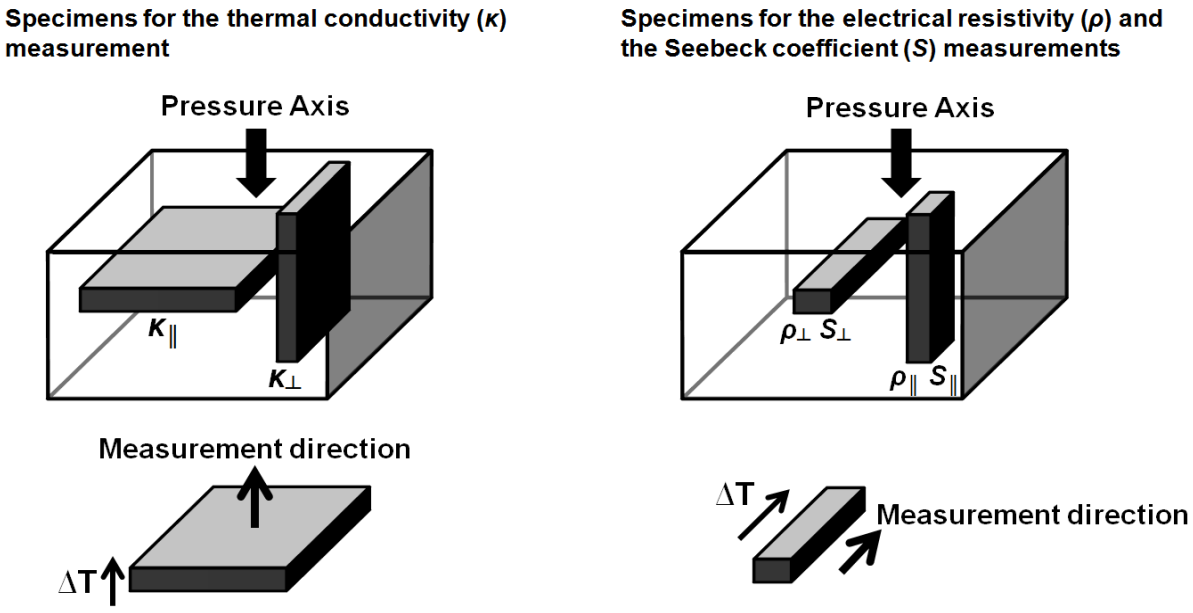

Fig. 2.3. Schematics of the specimens which were cut parallel (∥) and perpendicular (⊥) to the SPS pressure axis due to anisotropy of the samples for the TE properties measurements. The properties ρ, S and κ with the expression of out-of-plane (∥) and in-plane (⊥) denote the properties measured along directions parallel and perpendicular to the SPS pressure axis.

2.4 Other Characterizations

X-ray diffraction (XRD) analysis is obtained using a Bruker D8 diffractometer with Cu K_α-radiation and performed in air at room temperature on as-synthesized powders and consolidated pellets for phase identification with the scan range 2θ from 0 ° to 90 ° and stay for 2 sec. at each 0.01 °. The phases are analyzed and identified by Brucker DIFFRAC^{Plus} EVA software with ICDD PDF-2 Release 2003 database.

Microstructural analysis of the as-synthesized powders and the fracture surfaces of SPS samples is conducted using a ZEISS Supra 35 scanning electron microscope (SEM). The In-lens detector is used along with an acceleration voltage less than 7 kV and a less than 10 mm working distance.

Simultaneous measurements of thermogravimetry (TG) and differential thermal analysis (DTA) is performed in oxygen on a NETZSCH STA-449C. The phase transition is analyzed by

differential scanning calorimetry (DSC) using a NETZSCH DSC-404C under flowing air. A few milligrams of the material to be analyzed were packed into an alumina-lined platinum crucible and loaded into the TG/DTA and DSC. In this research the measurements are performed with a heating rate of 10 ℃/min up to the desired measuring temperature.

Chapter 3

Effects of Synthesis and Processing on the Thermoelectric Properties of $Ca_3Co_4O_{9+\delta}$

Abstract

$Ca_3Co_4O_{9+\delta}$ samples were synthesized by solid-state (SS) and sol–gel (SG) reactions, followed by spark plasma sintering under different processing conditions. The synthesis process was optimized and the resulting materials characterized with respect to their microstructure, bulk density, and thermoelectric transport properties. High power factors of about 400 $\mu W/m{\cdot}K^2$ and 465 $\mu W/m{\cdot}K^2$ (at 800 ℃) were measured for SS and SG samples, respectively. The improved thermoelectric performance of the SG sample is believed to originate from the smaller particle sizes and better grain alignment. The SG method is suggested to be a beneficial means of obtaining high-performance thermoelectric materials of $Ca_3Co_4O_{9+\delta}$ type.

This chapter is published in: N. Wu, T. C. Holgate, N. V. Nong, N. Pryds, and S. Linderoth, "Effects of Synthesis and Spark Plasma Sintering Conditions on the Thermoelectric Properties of $Ca_3Co_4O_{9+\delta}$," *J. Electron. Mater.*, vol. 42, no. 7, pp. 2134–2142, Apr. 2013 [43].

3.1 Introduction

Thermoelectric materials have provided a means to convert thermal energy into electrical energy. The performance of a thermoelectric material can be evaluated by the dimensionless figure-of-merit $ZT = S^2T/\rho\kappa$, which consists of the Seebeck coefficient (S), the electrical resistivity (ρ), the thermal conductivity (κ), and the absolute temperature (T). Shikano and Funahashi first brought attention to $Ca_3Co_4O_{9+\delta}$ as a high-temperature thermoelectric candidate by reporting a ZT of 0.83 (at 800 ℃) for a single crystal [67]. $Ca_3Co_4O_{9+\delta}$ has a misfit-layered structure with a CdI_2-type hexagonal CoO_2 subsystem and a rock-salt-type Ca_2CoO_3 subsystem. The electronic conduction takes place mainly in the CoO_2 layer while the Ca_2CoO_3 subsystem dominates the phononic conduction and may therefore be tuned to reduce the lattice thermal conductivity. However, the two-dimensional character of this layered structure can result in anisotropy in the thermal and electrical transport properties [67][118].

So far, many efforts have focused on $Ca_3Co_4O_{9+\delta}$ to achieve higher thermoelectric performance by either mastering the ion doping or by choice of the processing route, i.e., solid-state (SS) or sol–gel (SG) reactions [69][70][119]–[128]. For pure $Ca_3Co_4O_{9+\delta}$ synthesized by SS, the resulting improvement has led to its thermoelectric properties reaching $\rho = 9$ mΩ·cm, $S = 180\ \mu V/K$, and power factor $PF = 370\ \mu W/m{\cdot}K^2$ at 800 ℃, leading to a ZT of 0.25 [70]. On the other hand, for $Ca_3Co_4O_{9+\delta}$ synthesis by SG, it was shown that $\rho = 6.1$ mΩ·cm, $S = 165\ \mu V/K$, and $PF = 445\ \mu W/m{\cdot}K^2$ at 700 ℃, but unfortunately no data on the thermal conductivity were reported and therefore no value for ZT is available [120]. Recently, Kenfaui et al. conducted a systematic study by varying the conditions of the spark plasma sintering (SPS) process, such as applied pressures and sintering temperatures, discovering that the thermoelectric properties increase with increasing sintering temperature and pressure up to 50 MPa, reaching a PF of 315 $\mu W/m{\cdot}K^2$ at about 550 ℃ [68]. Many other attempts have been made to improve the thermoelectric properties of this type of material.[129][130]. However, more detailed study of the processing parameters along with their relationship to the resulting thermoelectric properties is still needed.

In this work, the thermoelectric properties of samples synthesized by SS and SG followed by consolidation using SPS under different processing conditions were investigated, i.e., temperature, pressure, and ramping rate. The microstructure, bulk density, and thermoelectric properties of the samples were compared and correlated to the processing parameters.

3.2 Experimental Procedure

In this study, solid-state reaction synthesis was achieved by using commercial $CaCO_3$ (99+ %) and Co_3O_4 (99.7 %) starting precursors. The precursors were mixed thoroughly in stoichiometric ratio followed by ball milling with an appropriate amount of ethanol for 48 h. The

dried mixtures were then calcined in air at 900 ℃ for 24 h. For SG synthesis, a stoichiometric ratio of $Ca(NO3)_2{\cdot}4H_2O$ (99+ %) and $Co(NO_3)_2{\cdot}6H_2O$ (99+ %) were dissolved in aqueous citric acid solution. Following initial heating at 75 ℃ and drying of the gel at 120 ℃ in a vacuum muffle oven, the gel was further heat treated at 750 ℃ for 2 h.

The powders produced by SS and SG were consolidated using a SPS (Dr. Sinter SPS-515S; Fuji Electronic Industrial Co., Ltd.). Enough powders were poured into a graphite die to fabricate 5 mm-thick pellets with diameter of 18 mm. A pulsed electric current was then passed through the powders under vacuum (10^{-3} bar) to consolidate the material. A range of processing conditions were chosen, such as sintering temperature 800 ℃ to 900 ℃, uniaxial pressure 30 MPa to 70 MPa, and ramping rate 100 ℃/min to 300 ℃/min. The sintering time was kept constant at 5 min. Table 3.1 presents the detailed SPS conditions.

Table 3.1. SPS process parameters and the relative densities of all samples.

Sample Number	**Synthesis Method**	**Sintering Temperature**	**Applied Pressure**	**Ramping Rate to Sintering Temp.**	**Relative Density***	$\alpha_{(00l)}$
1	SS	800 ℃	30 MPa	100 ℃/min	96 %	36 %
2	SS	850 ℃	30 MPa	100 ℃/min	97 %	39 %
3	SS	900 ℃	30 MPa	100 ℃/min	99 %	37 %
4	SS	800 ℃	50 MPa	100 ℃/min	99 %	41 %
5	SS	850 ℃	50 MPa	100 ℃/min	99 %	41 %
6	SS	900 ℃	50 MPa	100 ℃/min	99 %	37 %
7	SS	800 ℃	70 MPa	100 ℃/min	99 %	40 %
8	SS	850 ℃	70 MPa	100 ℃/min	99 %	42 %
9	SS	900 ℃	70 MPa	100 ℃/min	99 %	34 %
10	SS	850 ℃	50 MPa	150 ℃/min	99 %	40 %
11	SS	850 ℃	50 MPa	200 ℃/min	99 %	40 %
12	SS	850 ℃	50 MPa	300 ℃/min	99 %	38 %
13	SG	850 ℃	50 MPa	100 ℃/min	99 %	78 %

* The theoretical density of $Ca_3Co_4O_{9+\delta}$ is 4.68 g/cm^3 according to Masset et al. [63].

X-ray diffraction (XRD) analysis was conducted using a Bruker D8 diffractometer with Cu K_α-radiation. The bulk density of the samples was measured by the Archimedes method. Microstructural analysis of the powders and the fracture surfaces of SPS-processed samples was conducted using a ZEISS Supra 35 scanning electron microscope (SEM). In-plane Seebeck coefficient (S) and electrical resistivity (ρ) measurements were carried out with an ULVAC-RIKO ZEM3 from room temperature to 900 ℃ under a low-pressure helium atmosphere. The definitions of the in-plane and out-of-plane directions are illustrated in Fig. 3.1.

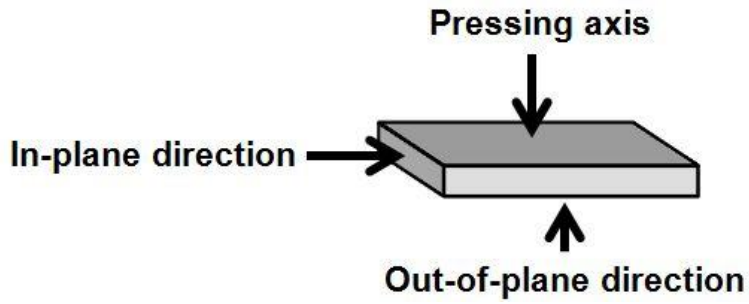

Fig. 3.1. Scheme of in-plane and out-of-plane direction definitions in this work. The in-plane and out-of-plane properties are measured perpendicular and parallel to the applied pressure axis, respectively.

The thermal conductivity was calculated using the equation $\kappa = \rho \cdot \alpha \cdot c_p$ (where ρ, α and c_p are the density, thermal diffusivity, and specific heat capacity). The out-of-plane thermal diffusivity was obtained under vacuum using a NETZSCH LFA-457 laser flash system. The c_p value used in this work was derived from the Dulong–Petit law: 0.798 $J/g{\cdot}K$ at any temperature.

3.3 Result and Discussion

XRD patterns of $Ca_3Co_4O_{9+\delta}$ powders before SPS consolidation are shown in Fig. 3.2(a). All the peaks could be indexed to $Ca_3Co_4O_{9+\delta}$ according to the JCPDS card (PDF # 21-0139) and the XRD patterns reported in the literature, indicating relatively high purity of these samples [63]. The insets in Fig. 3.2 show SEM micrographs of $Ca_3Co_4O_{9+\delta}$ particles produced by the two different synthesis routes, SS and SG; the average particle size for SS is around 2.5 μm with a plate-shape morphology, and the SG sample powders have an average particle size of about 500 nm with a similar morphology. A qualitative difference in the particles sizes of SS and SG powders can also be judged through the width of their XRD peaks (from grain-size broadening effects of nanosized grains), which is in good agreement with the observation from the SEM images (Fig. 3.2, insets). Figure 3.3 exhibits the XRD patterns of the SS and SG samples consolidated using SPS, which were taken parallel to the applied pressure direction. An enlarged

section of the (002) diffraction peaks of the SS and SG samples are also plotted in the insets of Fig. 3.3 for comparison. The change in the relative intensity of the *c*-axis (00*l*) as compared with the (20$\bar{1}$) and (020) peaks before and after SPS processing (Fig. 3.3) indicates the existence of preferred orientation in the samples. To get insight into the degree of preferred orientation, the volume fraction $\alpha_{(00l)}$ of the *c*-axis oriented grains of samples after SPS processing was calculated as

$$\alpha_{(00l)} = \sum(I_{00l}/I^{*}_{00l}) \Big/ \sum(I_{hkl}/I^{*}_{hkl}), \tag{3.1}$$

where I_{hkl} stands for the measured intensity of the (hkl) peaks of SPS-consolidated samples and I^{*}_{hkl} for the intensity of the as-synthesized $Ca_3Co_4O_{9+\delta}$ powders. The calculated a values corresponding to each sample in this work are presented in Table 3.1. The powders synthesized by SS and consolidated by SPS showed a similar *c*-axis orientation volume fraction in the range of 34 % to 41 %. In principle, a higher SPS applied pressure results in higher anisotropy due to texturing, but the calculations of the preferred orientation suggest that the anisotropy of $Ca_3Co_4O_{9+\delta}$ powders synthesized by SS is insensitive to the SPS applied pressure. In contrast, the SG powders (sample 13) exhibited a significant a value of up to 78 %, pointing out the fact that the degree of texturing in the SG-prepared sample is apparently larger than in the case of SS synthesis. The fundamental difference in the particle sizes may be responsible for this texturing. This will be evident later in the text.

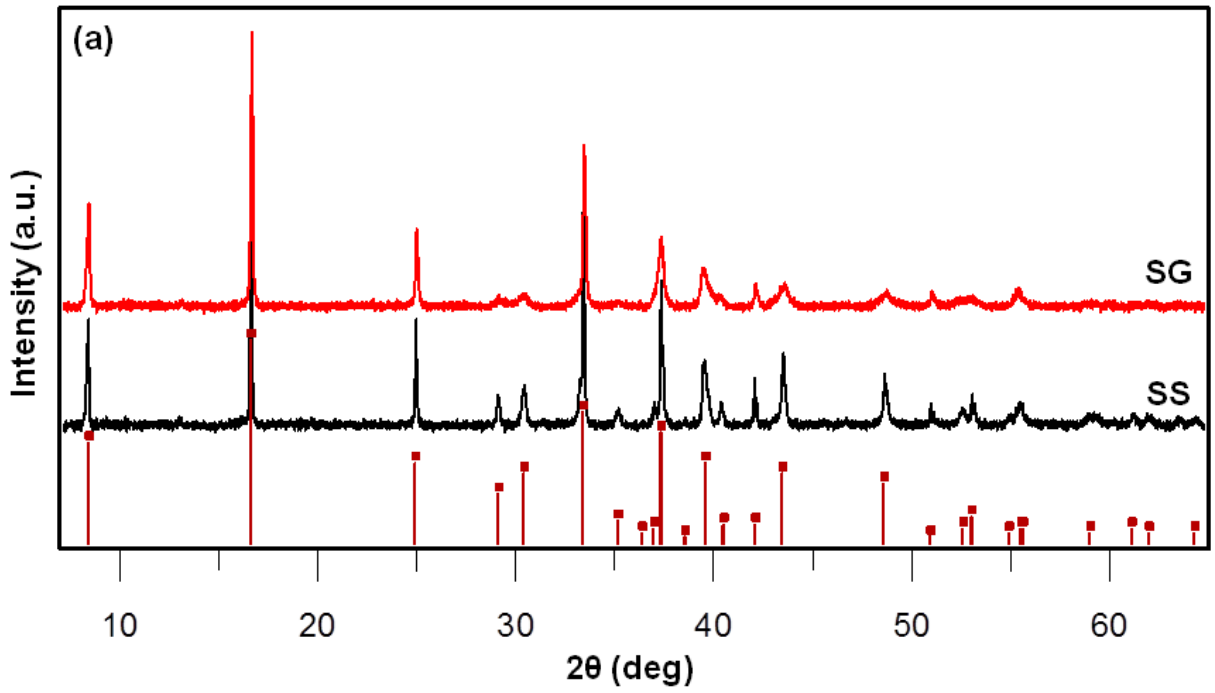

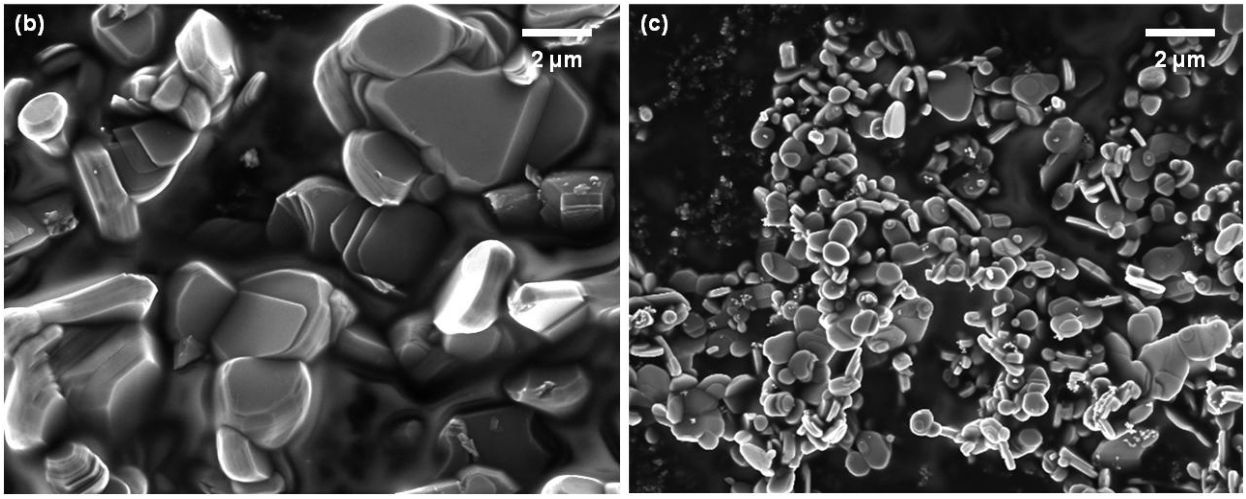

Fig. 3.2. (a) XRD patterns of $Ca_3Co_4O_{9+\delta}$ powders synthesized by SS (black) and SG (red) methods. All peaks can be indexed based on the JCPDS card for $Ca_3Co_4O_{9+\delta}$ (PDF # 21-0139) (brown). Shown in the insets are SEM micrographs (15k ×) of $Ca_3Co_4O_{9+\delta}$ particles from SS (b) and SG (c), respectively.

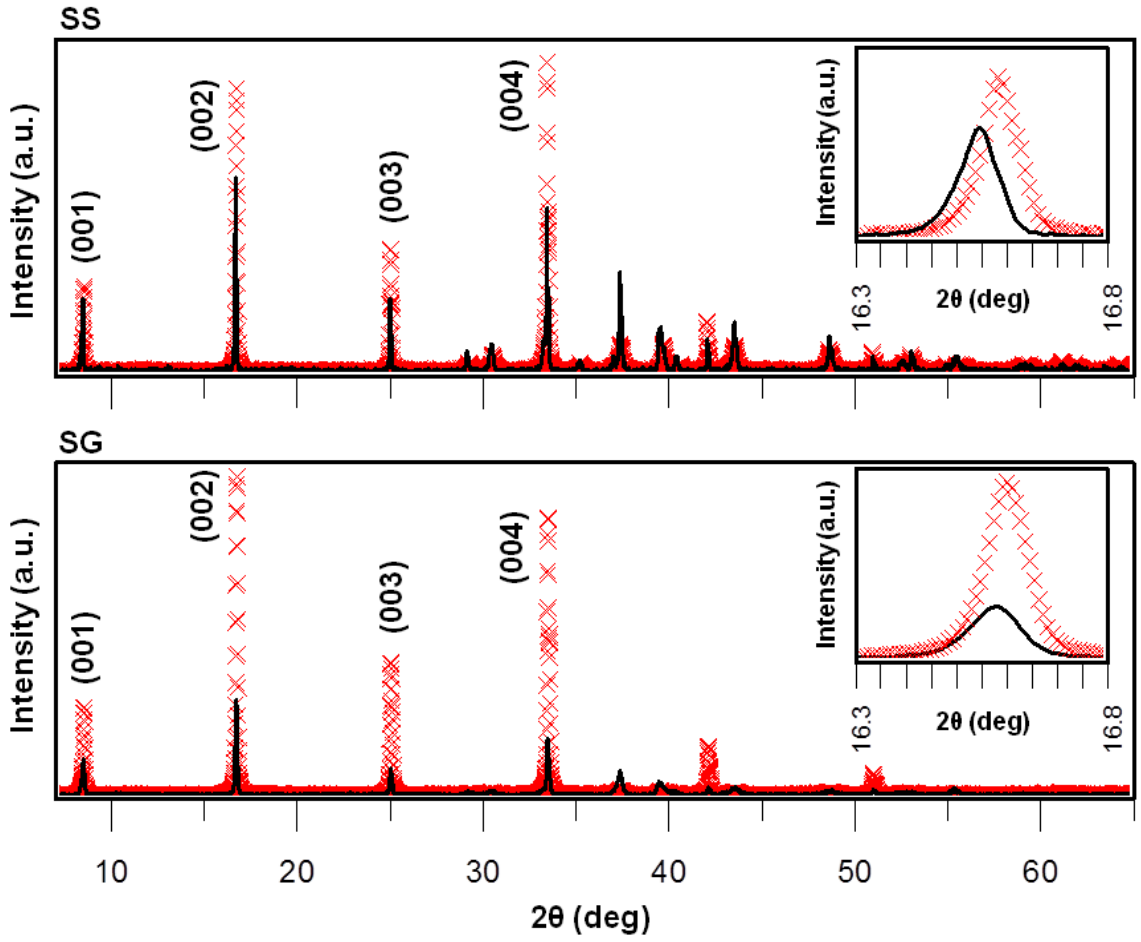

Fig. 3.3. XRD patterns before (black line) and after (red crosses) SPS consolidation. XRD patterns of the consolidated samples were obtained by measuring along the out-of-plane direction. The different intensities of the indexed peaks indicate the difference in the degree of grain alignment. The insets show magnified (002) peaks of $Ca_3Co_4O_{9+\delta}$ corresponding to each synthesis method.

Samples 1–9 are SS-synthesized powders consolidated with various applied pressures and sintering temperatures. A minimum applied pressure of 50 MPa or else a minimum sintering temperature of 900 ℃ resulted in fully densified $Ca_3Co_4O_{9+\delta}$ pellets. Since all the samples showed densities above 96 % of the theoretical density, there was no observable difference between SEM micrographs (Fig. 3.4). Samples 10–12 are a series of samples with varying ramping rate ranging from 100 ℃/min to 300 ℃/min. The ramping rate is the rate of heating before reaching a sintering temperature of 850 ℃ under an applied pressure of 50 MPa. The overall bulk densities of these samples were found to be above 99 %, indicating that the ramping rate had no obvious effect on SPS consolidation (Fig. 3.4).

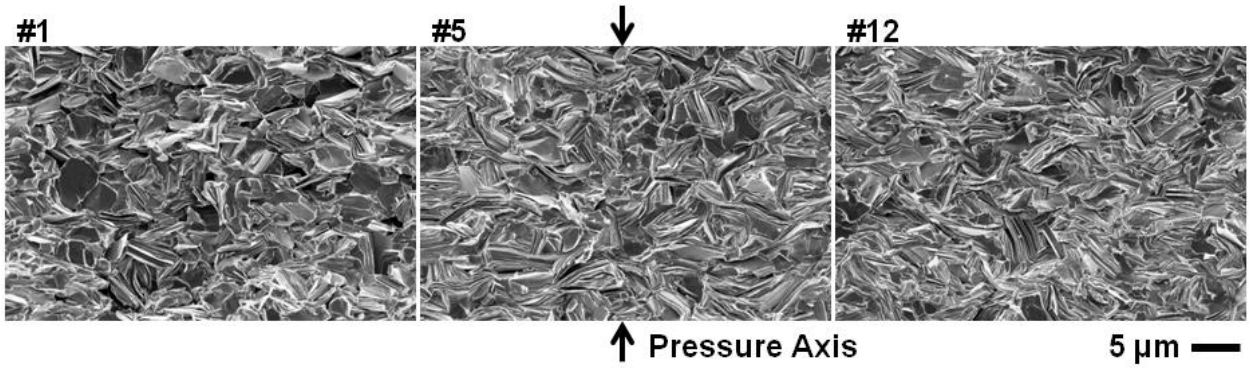

Fig. 3.4. Fracture-surface SEM micrographs (10k ×) of samples 1, 5, and 12 from left to right (with relative density of about 96 %, 99 %, and 99 %, respectively). The observations were carried out along the in-plane direction and the SPS applied pressure axis shown.

A series of in-plane electrical resistivity measurements as a function of temperature of samples densified with different applied pressures and sintering temperatures is shown in Fig. 3.5(a). All measured values are relatively lower than the ones reported in the literature (which range from 9 mΩ·cm to 12 mΩ·cm), especially at high temperature (e.g., 7.31 mΩ·cm at 700 ℃ for sample 9 in this work) [70]. Except for samples 1 and 2, all samples exhibit no significant difference, particularly above 300 ℃. These measurements indicate that, to obtain lower electrical resistivity in these samples, the applied pressure or sintering temperature should be at least 50 MPa or 850 ℃, respectively. This is consistent with the measurements of the relative

density. As seen in Fig. 3.5(f), the electrical resistivity decreases linearly with increasing density. For all the samples with density of 99 % or higher, the average resistivity at 800 ℃ is 7.52 mΩ·cm with less than 2% variance.

The in-plane Seebeck coefficient versus temperature is shown in Fig. 3.5(b). Due to the fact that the Seebeck coefficient is an intrinsic property of the materials, similar values ranging from 140 $\mu W/\mathrm{m}\cdot\mathrm{K}^2$ at room temperature to 175 $\mu W/\mathrm{m}\cdot\mathrm{K}^2$ at 800 ℃ were found, being comparable to the values reported in the literature [70]. It is worth noting that above 800 ℃ there is a turnover in the Seebeck coefficient data. While there is the possibility of a phase change from $Ca_3Co_4O_{9+\delta}$ to the $Ca_3Co_2O_6$ phase, this is unlikely as it would result in an increase in the electrical resistivity and the Seebeck coefficient [131][132]. The observed behavior may be explained in terms of oxygen nonstoichiometry resulting from measurement at high temperatures in a low-pressure atmosphere.

In Fig. 3.5(c) the in-plane power factor is displayed as a function of temperature. At 750 ℃, the maximum power factor is about 410 $\mu W/\mathrm{m}\cdot\mathrm{K}^2$, which is among the highest values reported so far in the literature for bulk samples produced by SS [70]. Because the power factor is inversely proportional to the electrical resistivity by the Seebeck coefficient squared, and since as Fig. 3.5(b) shows, the Seebeck coefficient is weakly affected by the processing conditions, the dependency of the power factor on the processing conditions follows the inverse of the resistivity's trend.

Figure 3.5(d) shows the out-of-plane thermal conductivity as a function of temperature. Except for the samples pressed at 30 MPa (samples 1 and 2), there is little discernible difference between the curves, especially near room and high temperatures. The reason for the lower thermal conductivity of the 30 MPa samples is attributed to the higher porosity (lower density), as seen in Fig. 3.5(f). The dimensionless figure-of-merit *ZT* is the value used to evaluate the overall performance of a thermoelectric material. It should be noted that the *ZT* value in this work is derived from the out-of-plane thermal conductivity obtained along the SPS pressure axis. Since the differences in the degree of texturing between the SS samples in and out of the plane are not significant, combining the in-plane power factor and the out-of-plane thermal conductivity to calculate *ZT* may be justified. Figure 3.5(e) shows *ZT* as a function of temperature. *ZT* seems to be independent of the SPS processing conditions. From the results above, the density seems to play a dominant role in the electrical resistivity and thermal conductivity separately, but for the overall thermoelectric performance, the variance in *ZT* is not significant.

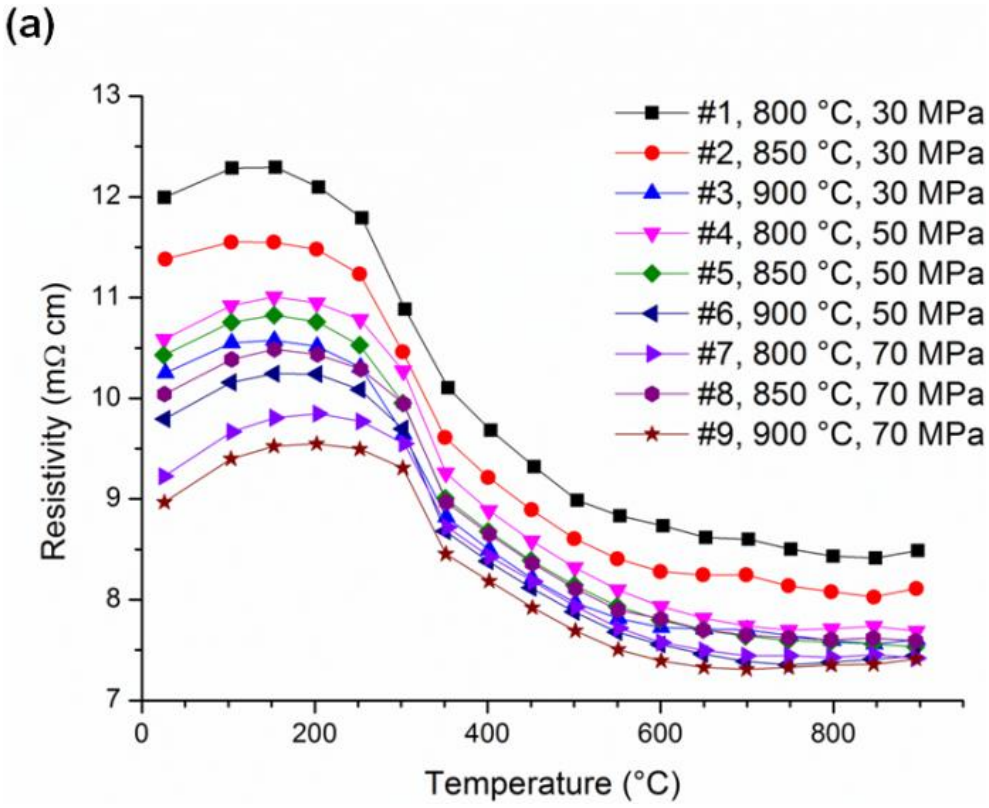
(a)
Resistivity (mΩ cm)
Temperature (°C)
#1, 800 °C, 30 MPa
#2, 850 °C, 30 MPa
#3, 900 °C, 30 MPa
#4, 800 °C, 50 MPa
#5, 850 °C, 50 MPa
#6, 900 °C, 50 MPa
#7, 800 °C, 70 MPa
#8, 850 °C, 70 MPa
#9, 900 °C, 70 MPa

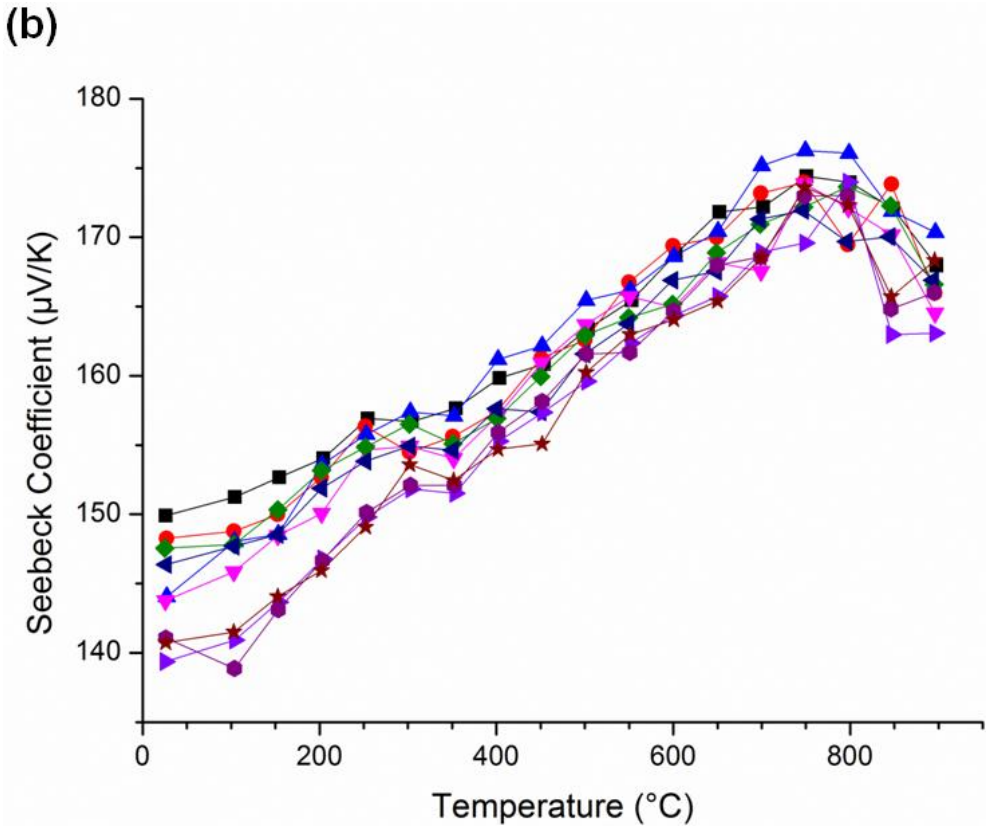
(b)
Seebeck Coefficient (μV/K)
Temperature (°C)

(c)

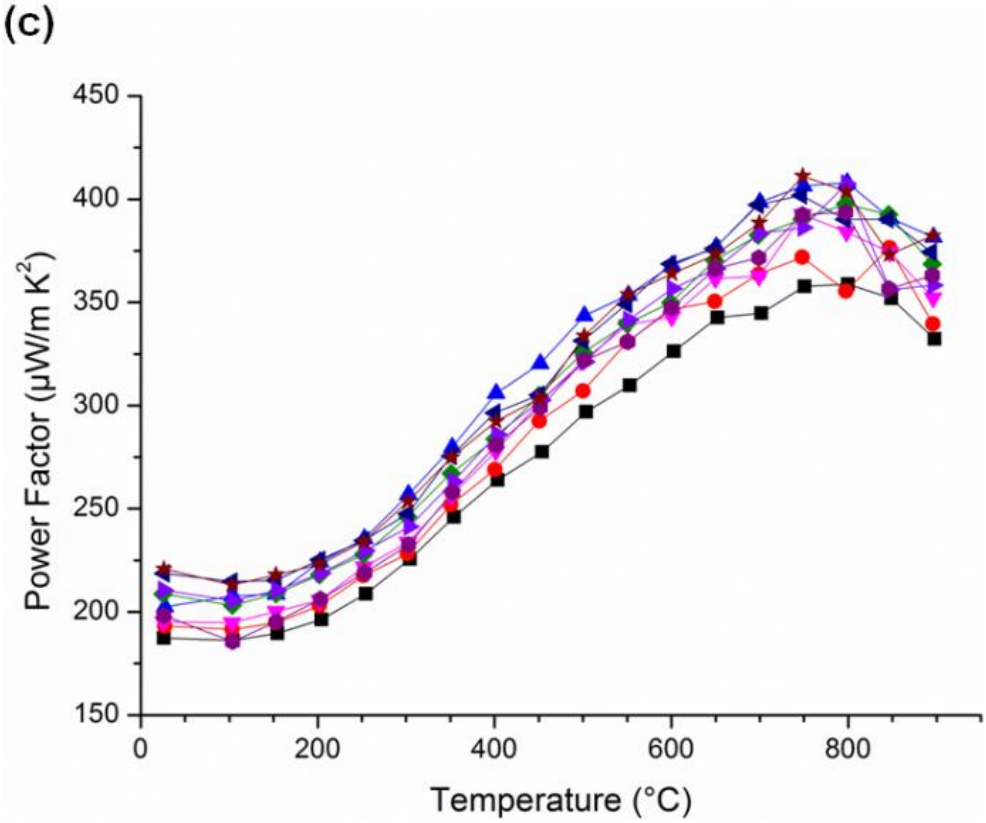
Power Factor (μW/m K²)
Temperature (°C)
150
200
250
300
350
400
450
0
200
400
600
800

(d)

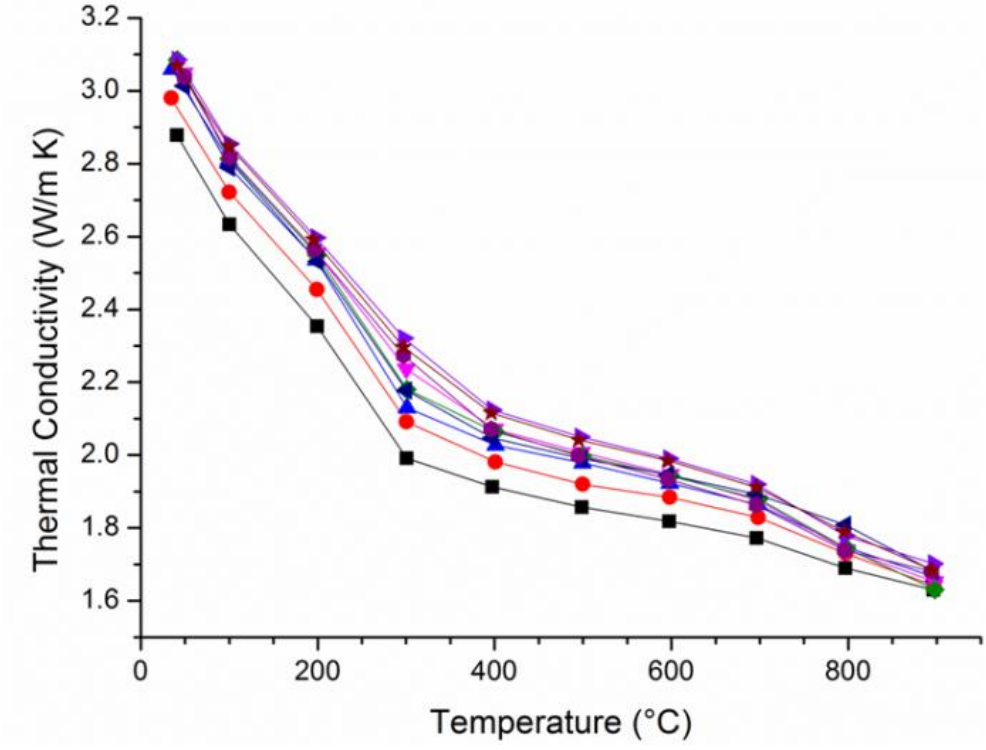
Thermal Conductivity (W/m K)
Temperature (°C)
1.6
1.8
2.0
2.2
2.4
2.6
2.8
3.0
3.2
0
200
400
600
800

(e)

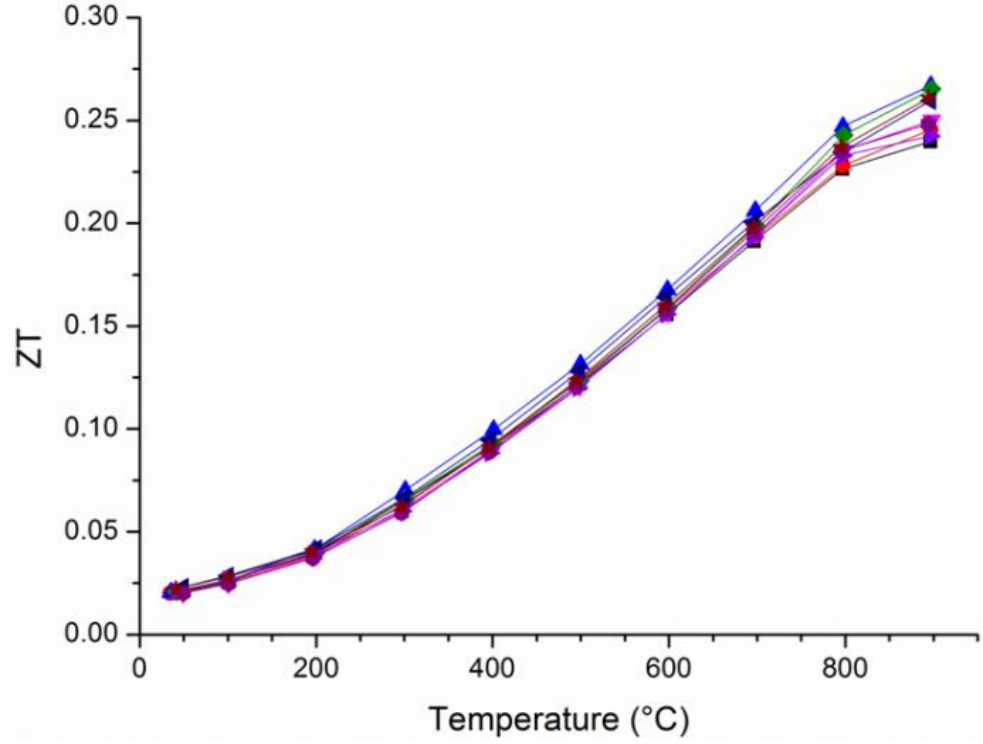
0.30
0.25
0.20
0.15
0.10
0.05
0.00
ZT
0
200
400
600
800
Temperature (°C)

(f)

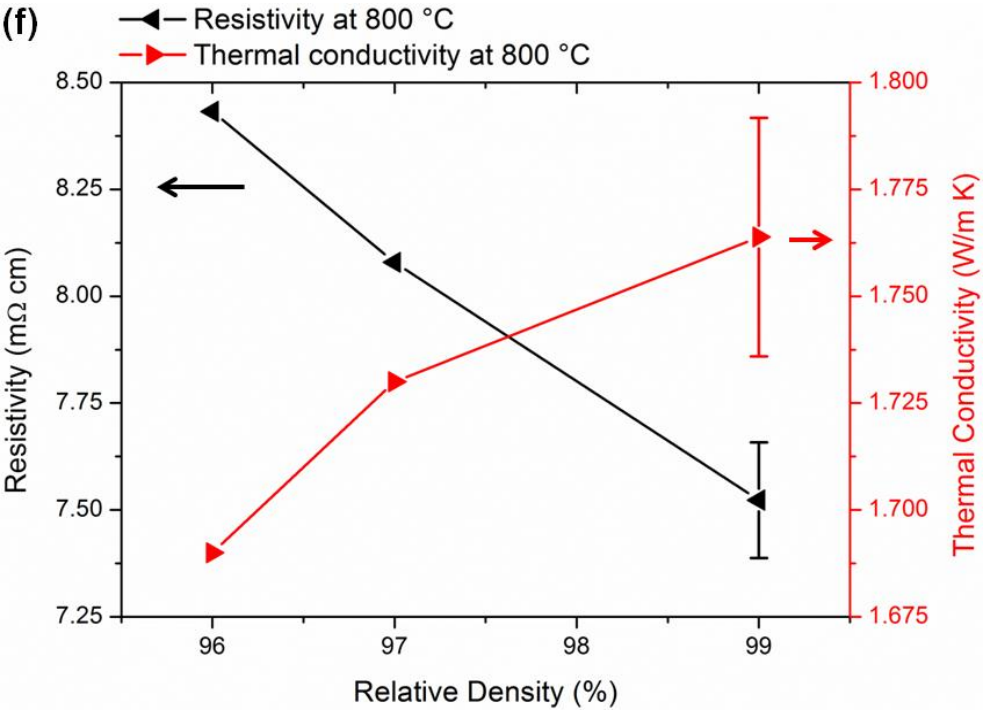
Resistivity at 800 °C
Thermal conductivity at 800 °C
8.50
8.25
8.00
7.75
7.50
7.25
Resistivity (mΩ cm)
1.800
1.775
1.750
1.725
1.700
1.675
Thermal Conductivity (W/m K)
96
97
98
99
Relative Density (%)

Fig. 3.5. Temperature dependence of the SS-synthesized $Ca_3Co_4O_{9+\delta}$ thermoelectric properties with varied SPS sintering temperatures (800 ℃ to 900 ℃) and applied pressures (30 MPa to 70 MPa) (SPS conditions for each sample are presented in Table 3.1): (a) in-plane electrical resistivity, (b) in-plane Seebeck coefficient, (c) in-plane power factor, (d) out-of-plane thermal conductivity, (e) the figure-of-merit, *ZT*, and (f) dependence of electrical resistivity (left black axis) and thermal conductivity (right red axis) on relative density.

The thermoelectric properties of samples densified using various ramping rates are shown in Fig. 3.6. There appears to be no relationship between the bulk density and the ramping rate. The thermoelectric properties of all the investigated SS samples were nearly the same despite the different ramping rates. As seen in Fig. 3.4, although high ramping rates during SPS processing may hinder grain growth, thus resulting in finer grains, this effect is not obvious in this study as indicated also by the thermoelectric properties.

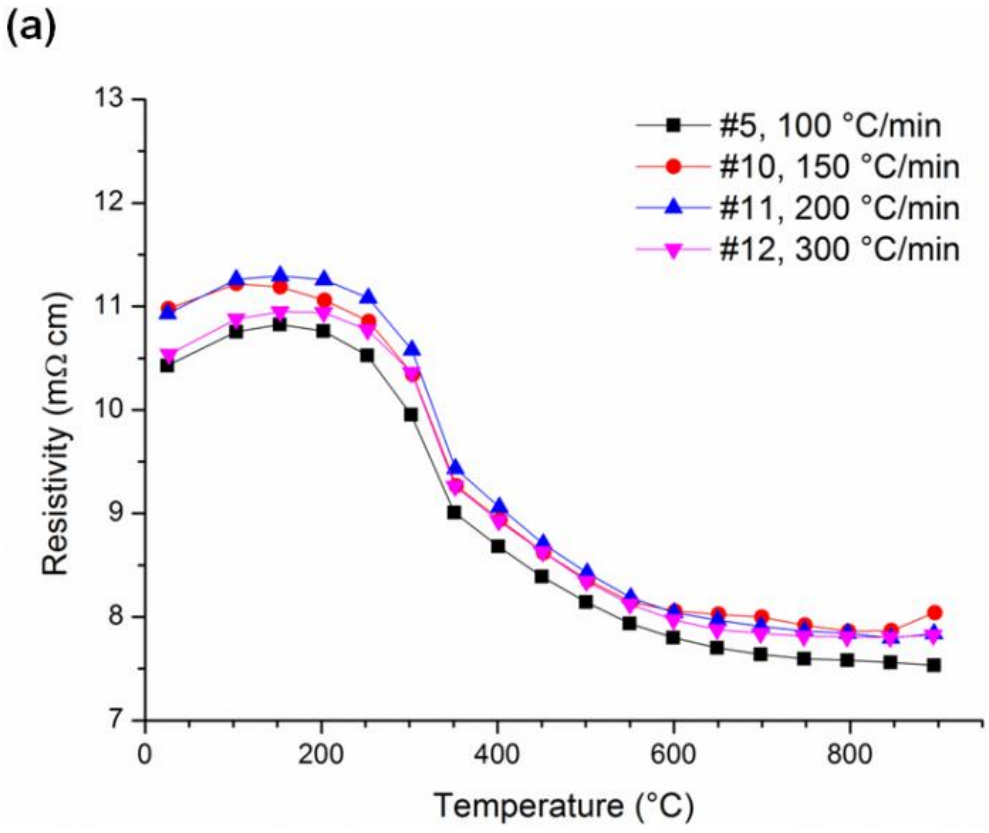

(b)

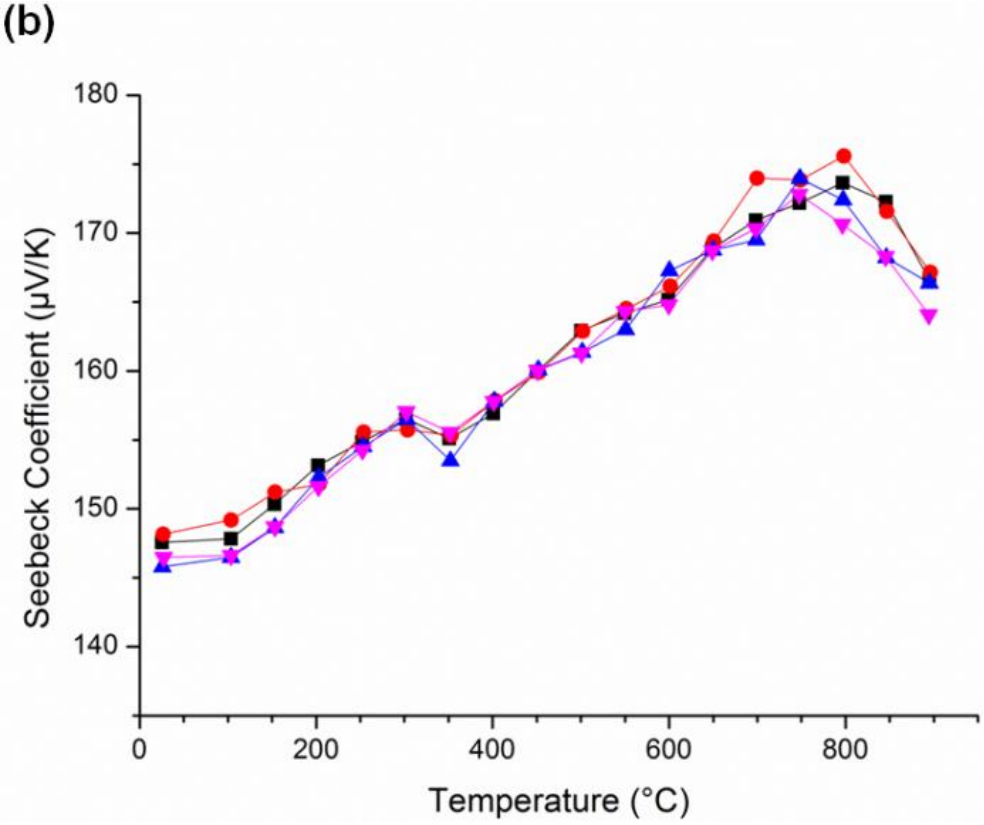
Seebeck Coefficient (μV/K)
180
170
160
150
140
0
200
400
600
800
Temperature (°C)

(c)

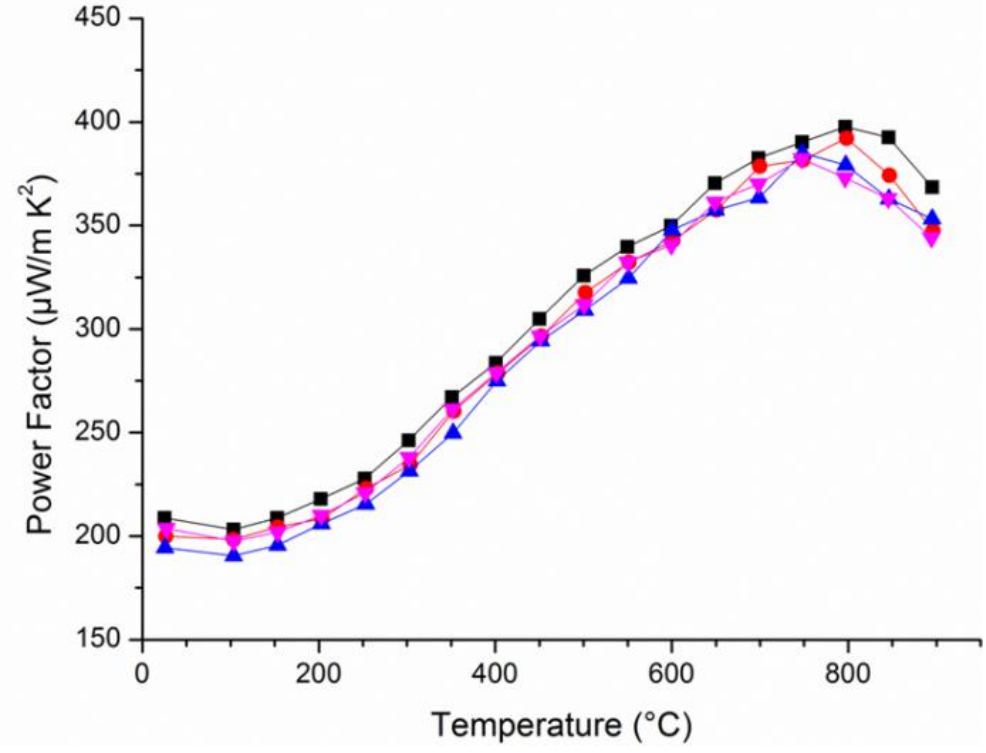
Power Factor (μW/m K²)
450
400
350
300
250
200
150
0
200
400
600
800
Temperature (°C)

(d)

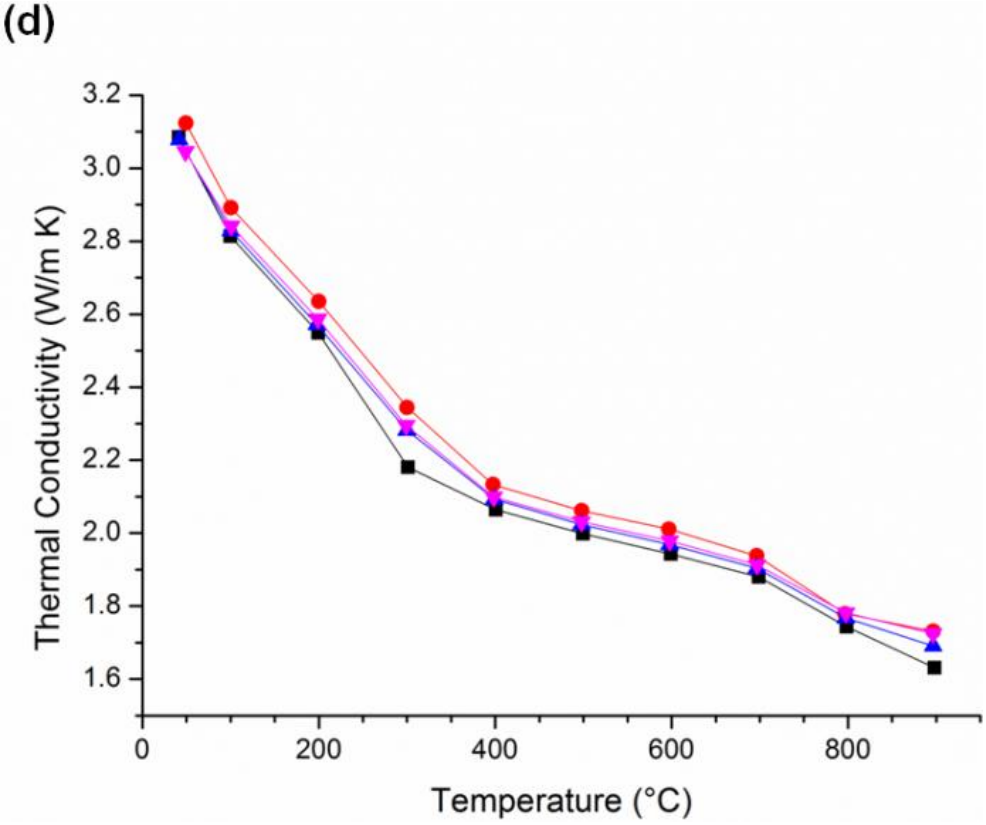
Thermal Conductivity (W/m K)
3.2
3.0
2.8
2.6
2.4
2.2
2.0
1.8
1.6
0
200
400
600
800
Temperature (°C)

(e)

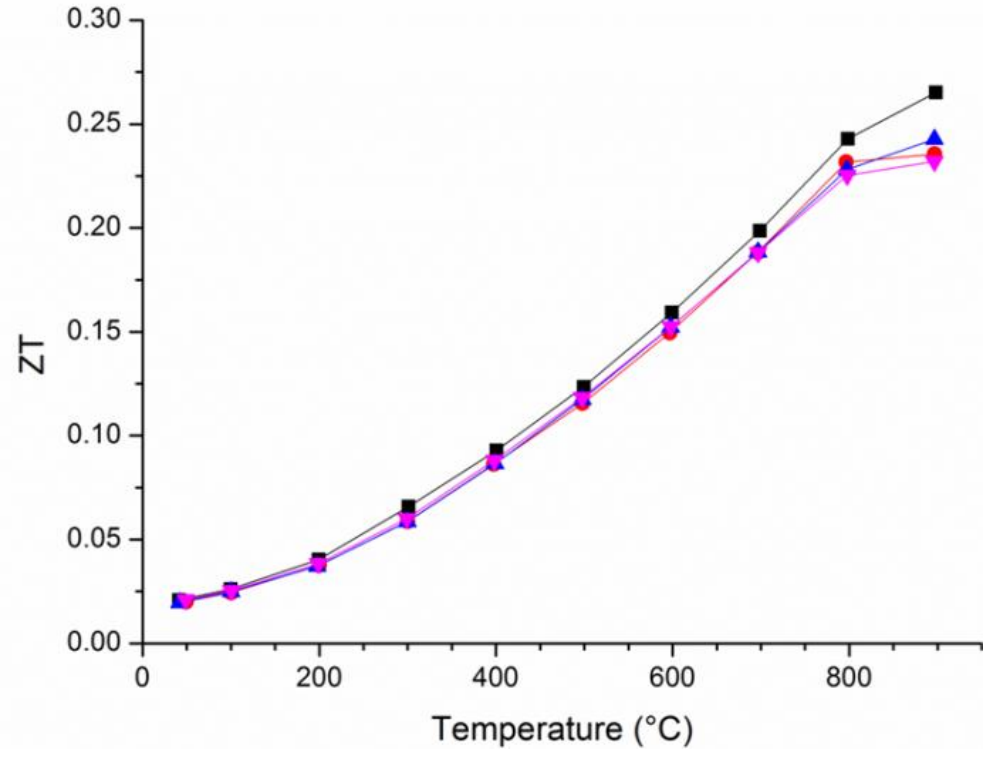
ZT
0.30
0.25
0.20
0.15
0.10
0.05
0.00
0
200
400
600
800
Temperature (°C)

Fig. 3.6. Temperature dependence of the SS-synthesized $Ca_3Co_4O_{9+\delta}$ thermoelectric properties with constant SPS sintering temperature (850 ℃) and applied pressure (50 MPa) but varied ramping rate from 100 ℃/min to 300 ℃/min (SPS conditions for each sample are presented in Table 3.1): (a) in-plane electrical resistivity, (b) in-plane Seebeck coefficient, (c) in-plane power factor, (d) out-of-plane thermal conductivity, and (e) the figure-of-merit, *ZT*.

Taking into account the experimental results presented above, the best conditions to consolidate SS-synthesized $Ca_3Co_4O_{9+\delta}$ powders would be sintering temperature of 850 ℃ with applied pressure of 50 MPa and ramping rate of 100 ℃/min . Increasing the sintering temperature and applied pressure results in no significant improvement of the thermoelectric properties of the material. In addition, no visual texturing as a function of applied load for the samples synthesized by SS could be found by SEM observation. A load of 50 MPa would therefore be a rational starting pressure to obtain a fully consolidated SS-synthesized $Ca_3Co_4O_{9+\delta}$ pellet.

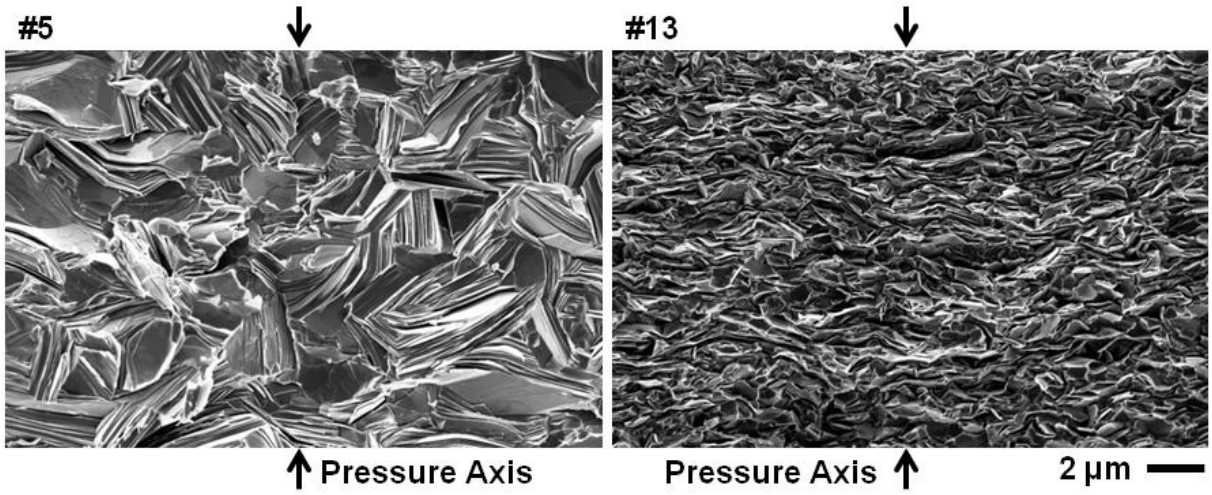

Fig. 3.7. SEM micrographs (20k ×) of fracture surfaces of $Ca_3Co_4O_{9+\delta}$ samples synthesized by SS (left, sample 5) and SG (right, sample 13) with an identical SPS process. The observations were carried out along the in-plane direction, and the SPS applied pressure axis is as described.

In this work, $Ca_3Co_4O_{9+\delta}$ powders were also synthesized by SG. The SPS condition used to consolidate the SG powders was deduced from the process parameters required to consolidate the SS powders, i.e., 850 ℃ sintering temperature, 50 MPa applied pressure, and 100 ℃/min ramping rate. The sample prepared by SG was found to be fully densified, about 99 % of the theoretical density. Figure 3.7 shows a comparison of SEM micrographs of fracture surfaces of both SS- and SG-synthesized $Ca_3Co_4O_{9+\delta}$ densified by the same SPS process. Comparison of

these micrographs reveals an obvious difference in the morphology of the samples. The SG sample showed much smaller lamellar grains (about 600 nm) than the SS one (3.5 μm). It is evident that the SPS consolidation of the SG powders can preserve the fine grain sizes when sintering at 850 ℃ for only several minutes, e.g., 5 min in this work. In addition to the grain size, the texturing is also visible in SG (Fig. 3.7), which is consistent with the XRD results, i.e., an obvious difference of *c*-axis preferred orientation volume fraction of 78 % for SG as compared with 41 % for SS synthesis.

Figure 3.8 shows a comparison of the thermoelectric properties between SG and SS powders consolidated under identical SPS processing conditions. The electrical resistivity for the SG samples showed lower values throughout the whole range of measured temperatures. At 700 ℃ the electrical resistivity was 5.74 $\mathrm{m\Omega \cdot cm}$, which is the lowest reported value so far for $Ca_3Co_4O_{9+\delta}$ [120]. On the other hand, the Seebeck coefficient of the SG sample was comparable to the reported value of the previous work [129]. Because of the lower electrical resistivity compared with SS synthesis, a higher power factor was obtained through the whole measured temperature range, with a maximum value of about 465 $\mu\mathrm{W/m \cdot K^2}$ at 800 ℃. The higher power factor may be a result of pronounced grain alignment. According to Noudem et al., the power factor could be enhanced from 70 $\mu\mathrm{W/m \cdot K^2}$ to 400 $\mu\mathrm{W/m \cdot K^2}$ at 550 ℃ with the improvement of grain alignment by a novel edge-free SPS technique [130]. The measured values of the out-of-plane thermal conductivity were found to be lower than for the sample prepared by SS. This result may be explained by the role of grain boundaries in the transport properties of the material. Finally, the *ZT* at 800 ℃ is found to be about 0.35. However, it is not completely clear what is the effect of the anisotropy on the figure-of-merit.

(a)

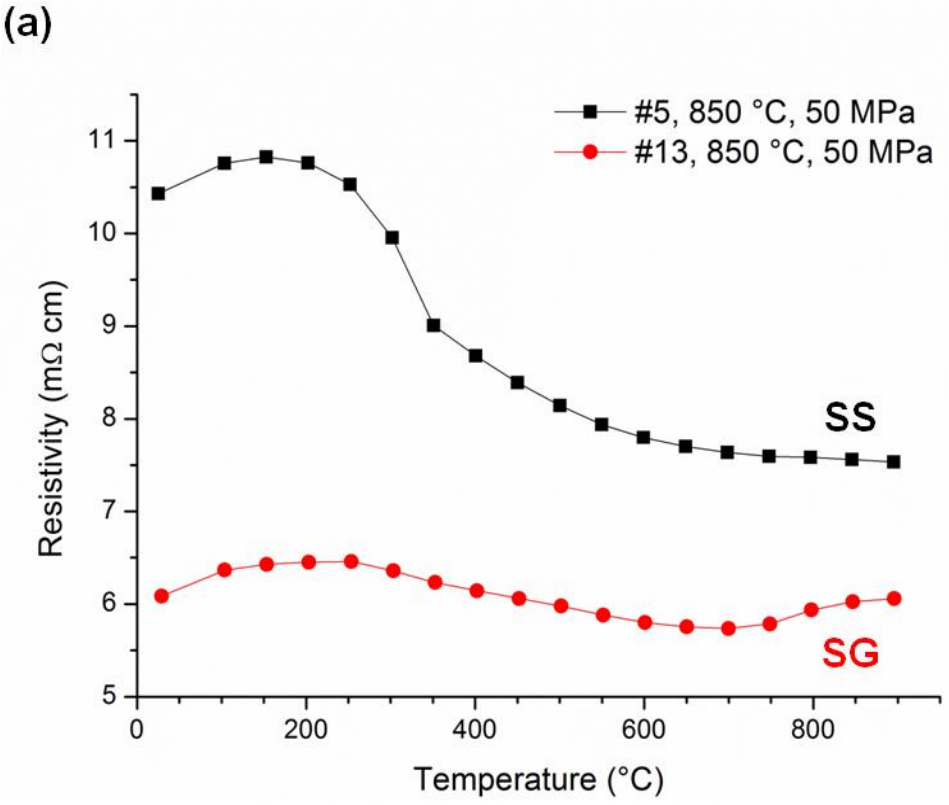
#5, 850 °C, 50 MPa
#13, 850 °C, 50 MPa
SS
SG
Resistivity (mΩ cm)
Temperature (°C)
11
10
9
8
7
6
5
0
200
400
600
800

(b)

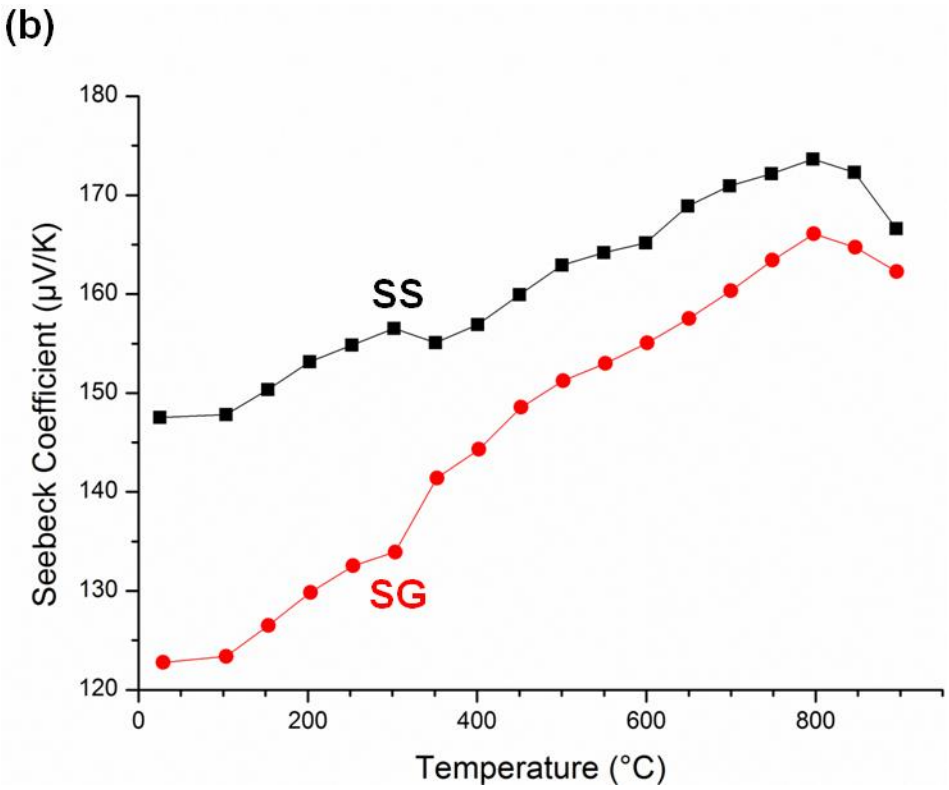
SS
SG
Seebeck Coefficient (μV/K)
Temperature (°C)
180
170
160
150
140
130
120
0
200
400
600
800

(c)

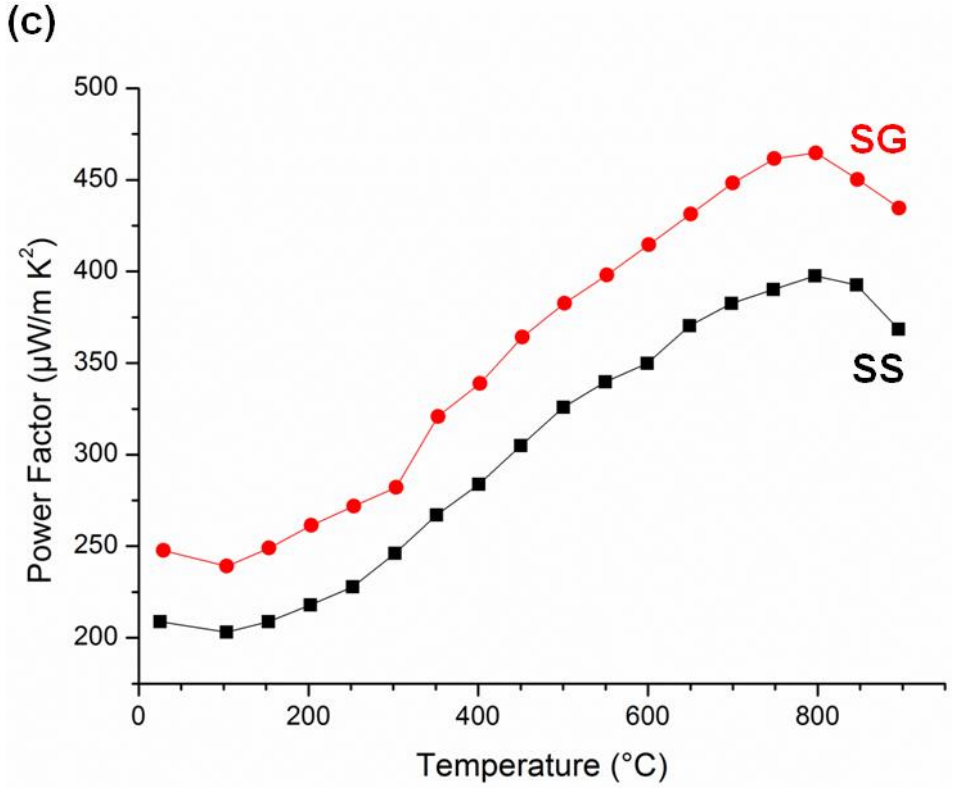
Power Factor (μW/m K²)
Temperature (°C)
SG
SS
500
450
400
350
300
250
200
0
200
400
600
800

(d)

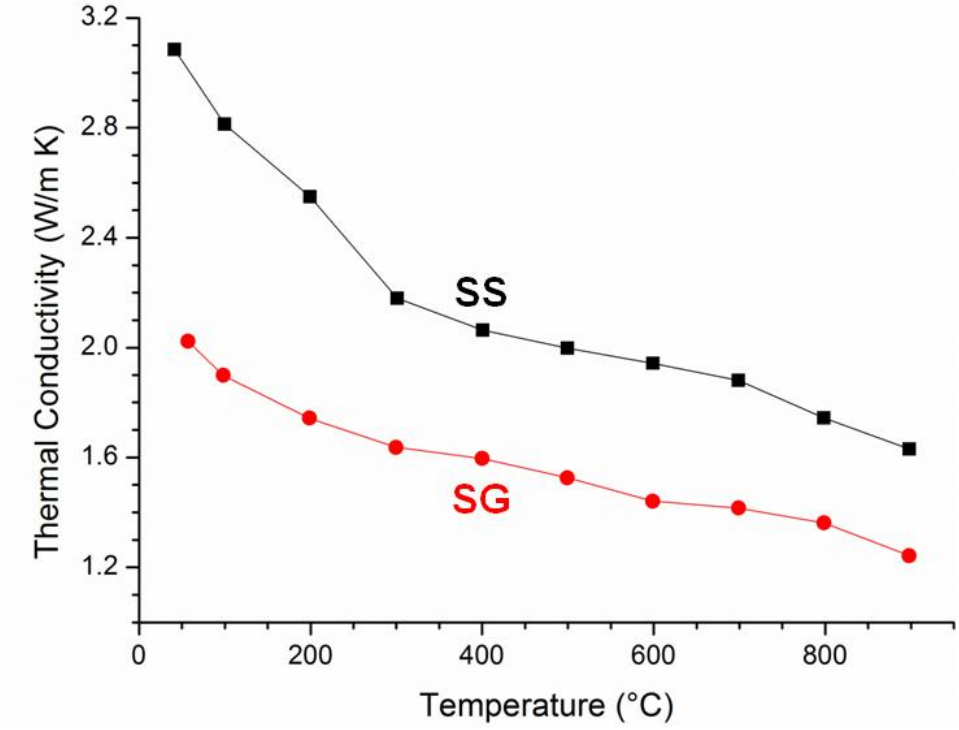
Thermal Conductivity (W/m K)
Temperature (°C)
SS
SG
3.2
2.8
2.4
2.0
1.6
1.2
0
200
400
600
800

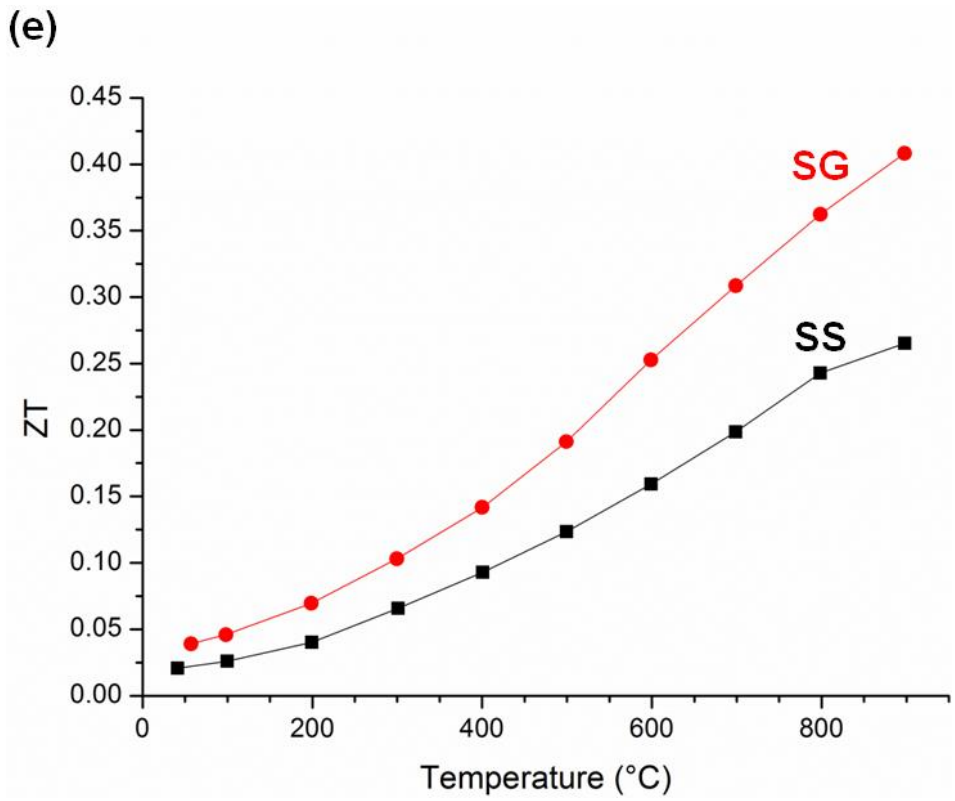

Fig. 3.8. Temperature dependence of the thermoelectric properties: (a) in-plane electrical resistivity, (b) in-plane Seebeck coefficient, (c) in-plane power factor, (d) out-of-plane thermal conductivity, and (e) the figure-of-merit, *ZT*, of $Ca_3Co_4O_{9+\delta}$ samples synthesized by SS (black, sample 5) and SG (red, sample 13) with identical SPS conditions of sintering temperature of 850 ℃, applied pressure of 50 MPa, and ramping rate of 100 ℃/min.

3.4 Conclusion

In this work, the applied pressure and sintering temperature were varied systematically to find optimized spark plasma sintering conditions for consolidation of $Ca_3Co_4O_{9+\delta}$ powders synthesized by solid-state reaction. Samples were evaluated with respect to their thermoelectric transport properties, density, and degree of texturing. Additionally, a sample prepared from SG-synthesized powders and densified using the SPS parameters optimized for the SS powders was likewise evaluated for comparison. With the SS-synthesized $Ca_3Co_4O_{9+\delta}$ starting powders, the bulk density was found to be the key parameter for reducing the electrical resistivity and thus maximizing the power factor. However, the *ZT* remains unchanged at about 0.23 at 800 ℃ for all SS-prepared samples.

For the SG-prepared $Ca_3Co_4O_{9+\delta}$ powders, the sample seems to preserve the particle size during SPS as well as exhibiting a visible degree of texturing. Sintering at 850 ℃ with an applied pressure of 50 MPa during SPS was used to fabricate high-density, fine-grained $Ca_3Co_4O_{9+\delta}$ pellets. Measurements of the thermoelectric properties revealed an enhancement in the electrical resistivity and the power factor to 5.74 mΩ·cm at 700 ℃ and 465 $\mu W/m{\cdot}K^2$ at 800 ℃, respectively. Regarding the Seebeck coefficient, the lower observed values as compared with SS synthesis suggest an intrinsic difference in the carrier concentration resulting from these two synthesis routes, which will be investigated in the future. In summary, SG would be a preferable synthesis method to produce high-performance thermoelectric $Ca_3Co_4O_{9+\delta}$ material. However, the texturing and particle size effects should first be explored and controlled.

Chapter 4

High Temperature Thermoelectric Properties of $Ca_3Co_4O_{9+\delta}$ by Auto-combustion Synthesis and Spark Plasma Sintering

Abstract

A rapid method for the synthesis of $Ca_3Co_4O_{9+\delta}$ powder is introduced. The procedure is a modification of the conventional citrate–nitrate sol–gel method where an auto-combustion process is initiated by a controlled thermal oxidation–reduction reaction. The resulting powders inherit the advantages of a wet chemical synthesis, such as morphological and compositional homogeneity, and fine, well-defined particle sizes coming from the controlled nature of the auto-combustion. Optimized spark plasma sintering (SPS) processing conditions were determined and used to fabricate dense and highly *c*-axis oriented samples. The microstructure and thermoelectric transport properties were determined both parallel (∥) and perpendicular (⊥) to the SPS pressure axis in order to investigate any possible anisotropy variations in the transport properties. At 800 ℃, power factors of 506 $\mu W/m{\cdot}K^2$ (⊥) and 147 $\mu W/m{\cdot}K^2$ (∥), thermal conductivities values of 2.53 $W/m{\cdot}K$ (⊥) and 1.25 $W/m{\cdot}K$ (∥), and resulting figures-of-merit, *ZT*, of 0.21 (⊥) and 0.13 (∥) were observed.

This chapter is published in: N. Wu, T. C. Holgate, N. V. Nong, N. Pryds, and S. Linderoth, "High temperature thermoelectric properties of $Ca_3Co_4O_{9+\delta}$ by auto-combustion synthesis and spark plasma sintering," *J. Eur. Ceram. Soc.*, vol. 34, no. 4, pp. 925–931, Apr. 2014 [44].

4.1 Introduction

Thermoelectric materials provide a mean to convert thermal energy into electrical energy via the Seebeck effect. The performance of a thermoelectric material can be evaluated by the dimensionless figure-of-merit $ZT = S^2T/\rho\kappa$, which consists of the Seebeck coefficient (S), electrical resistivity (ρ), thermal conductivity (κ) and absolute temperature (T). Oxides are one of candidates of high interest for thermoelectric applications due to their low cost, high-temperature stability in air and chemical inertness. Shikano et al. first brought attention to $Ca_3Co_4O_{9+\delta}$ as a high temperature thermoelectric p-type oxide candidate by reporting a ZT of 0.83 (at 800 ℃) for a single crystalline sample [67]. $Ca_3Co_4O_{9+\delta}$ possesses a misfit-layered structure with a CdI_2-type hexagonal CoO_2 subsystem and a rock salt-type Ca_2CoO_3 subsystem that are alternately stacked along the c-axis with identical a, c and β parameters but different and incommensurate $b1$ and $b2$. Therefore, this misfit-layered oxide can be described with the formula $[Ca_2CoO_3][CoO_2]_{b1/b2}$ with a $b1$ to $b2$ ratio of approximately 1.62 [63][66]. The electronic conduction takes place mainly within the CoO_2 layer with the Ca_2CoO_3 layer serving as a charge reservoir, and while it is difficult to determine in which layer the lattice thermal conductivity is higher, the misfit between layers is expected to hinder the cross-plane phonon transport [133]. Therefore, anisotropy in the thermal and electrical transport properties is expected due to the two-dimensional character of this layered structure [63][120][134][135].

At present, the fabrication of pure or doped $Ca_3Co_4O_{9+\delta}$ powders has mainly followed one of two routes: solid-state reaction or wet-chemical synthesis [43][69][70][71][118][125] [128][136]–[138]. The advantages of the solid-state reaction are simplicity and high yield, but the purity and the homogeneity are two major issues of concern. By contrast, wet-chemical synthesis eliminates the drawbacks of the solid-state reaction by atomic scale mixing, but the low yield associated with this process limits the scalability. To retain the advantages of the wet-chemical synthesis, Song et al. reported the use of a polyacrylamide gel synthesis involving fast polymerization in calcium and cobalt nitrate aqueous solution, increasing the yield [136]. Zhang et al. also introduced a co-precipitation method to ensure the homogeneity of the powder [137]. Recently Wang et al. exhibited that via hydrothermal treatment the $Ca_3Co_4O_{9+\delta}$ particle size can be reduced further for better thermoelectric properties [71]. Except for these unique methods, the Pechini method is still widely employed for $Ca_3Co_4O_{9+\delta}$ synthesis, which involves the chelation between citrate and the metal ions originating from dissolved metal nitrates [139]. Following the decomposition of the vaporization of the organic constituents and citrate complexes at elevated temperatures (400–500 ℃), highly homogenous and sub-micron scale oxide powders can be obtained [138]. By this method, not only the atomic scale mixing for chemical homogeneity can be achieved, but also the feasibility of doping is provided by the introduction of dopant cation nitrates [128]. Despite the fact that this method is adaptable to many oxide systems, it still suffers from some practical difficulties, for instance, the resulting gel after drying is very adhesive and difficult to handle. Additionally, the gel swells considerably during the pyrolysis resulting in a

drawn out and uneven reaction rather than a favored rapid single step reaction. The present work sought to overcome these problems by using calcium and cobalt nitrates as the source of the metal ions, which were dissolved in a citric acid aqueous solution according to the Pechini method, but with a modified citrate–nitrate ratio that resulted in a rapid auto-combustion process induced by an exothermal oxidation–reduction reaction. The introduction of the auto-combustion step not only promotes the complete decomposition of the citrate complexes but also suppresses the grain growth by shortening the total reaction time at high temperature. The auto-combustion reaction was followed by the consolidation of the powders using spark plasma sintering (SPS) under different processing conditions. Due to the nature of the processing and the layered crystal structure of the material, the properties along both the parallel (∥) and perpendicular (⊥) directions relative to the SPS pressure axis were studied and are discussed in this paper.

4.2 Experimental Procedure

A stoichiometric ratio of analytical regent grade $Ca(NO_3)_2{\cdot}4H_2O$ (99+ %) and $Co(NO_3)_2{\cdot}6H_2O$ (99+ %) was dissolved in an appropriate amount of distilled water, and a specific amount of citric acid (99+ %) was added to keep the citrate–metal cation molar ratio at 1:1. Additionally, the citrate-to-nitrate molar ratio was tuned by introducing different relative amounts of NH_4NO_3 (98+ %) ranging from 0.28 to 0.50. After initially drying the gel while stirring continuously at 75 ℃ until a uniform viscous gel was obtained, the hot plate temperature was raised to about 250 ℃ until the auto-combustion process was initiated, which was completed within a minute. The resulting powders were calcined at 750 ℃ for 2 h to obtain single phase $Ca_3Co_4O_{9+\delta}$.

Subsequently, the powders were consolidated by a spark plasma sintering (SPS, Dr. Sinter SPS-515S, Fuji Electronic Industrial Co., Ltd.). Powders were poured into a graphite die to fabricate 10 mm-thick pellets with a diameter of 18 mm. A pulsed electric current was then passed through the powders while under vacuum (10^{-3} bar) to consolidate the material. Based on our previous results, a range of the sintering temperatures were chosen from 700 to 850 ℃, with a fixed uniaxial pressure of 50 MPa and a ramping rate of 100 ℃/min. The sintering time was kept constant at 5 min [43].

The SPS samples were cut in different directions as shown in Fig. 4.1 depending on the type of characterizations. The symbols "∥" and "⊥" are used to denote the properties measured along the directions parallel and perpendicular to the SPS pressure axis, respectively.

Simultaneous measurements of thermogravimetry (TG) and differential thermal analysis (DTA) were performed in oxygen with a heating rate of 10 ℃/min on a Netzsch STA-449C. Additionally, the formation of the $Ca_3Co_4O_{9+\delta}$ phase from sol–gel produced precursors was analyzed by differential scanning calorimetry (DSC) using a Netzsch DSC-404C. After auto-igniting the sol–gel, the resulting powders were heated to 425 ℃ to remove any residual

organics. A few milligrams of the product were lightly packed into an alumina-lined platinum crucible and loaded into the DSC. The measurement was performed under flowing air with a heating rate of 10 ℃/min up to 825 ℃.

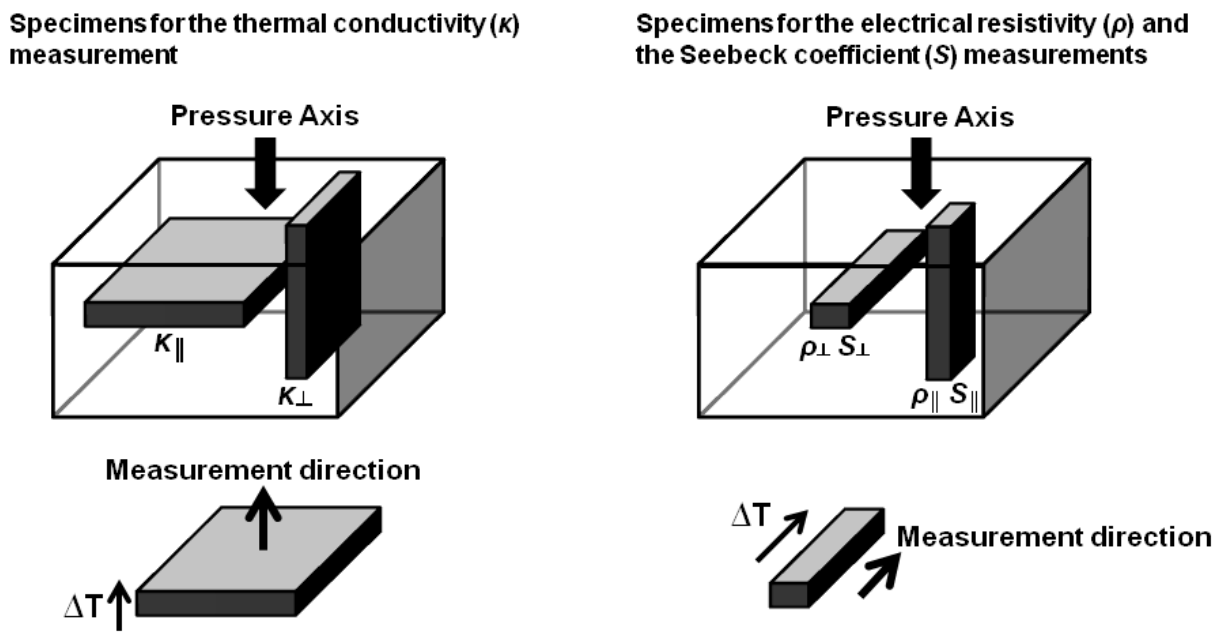

Fig. 4.1. Schematics of samples cut parallel (∥) and perpendicular (⊥) to the SPS pressure axis for the anisotropic thermoelectric properties measurements. The properties S, ρ and κ with subscript ∥ and ⊥ denote the properties measured along directions parallel and perpendicular to the SPS pressure axis.

X-ray diffraction (XRD) patterns were obtained using a Bruker D8 diffractometer with Cu K_α-radiation. Microstructural analysis of the synthesized powders and the fracture surfaces of SPS samples was conducted using a ZEISS Supra 35 scanning electron microscope (SEM). The Seebeck coefficient (S) andelectrical resistivity (ρ) measurements were carried out simultaneously with an ULVAC-RIKO ZEM3 from room temperatureup to 800 ℃ under a low-pressure helium atmosphere.

The thermal conductivity was calculated using the equation $\kappa = \rho \cdot \alpha \cdot c_p$ (where ρ, α and c_p are the density, thermal diffusivity, and specific heat capacity). The thermal diffusivity was obtained under vacuum in a NETZSCH LFA-457 laser flash system. The c_p in this work was taken to be the temperature independent Dulong–Petit value of 0.798 J/g·K. The bulk densities of

the samples were measured by the Archimedes' method and compared with the theoretical density of $Ca_3Co_4O_9$, which is 4.68 g/cm^3 according to Masset et al [63].

4.3 Result and Discussion

According to Pederson's reaction model, the thermal oxidation–reduction reaction in a citrate–nitrate system can be represented by the following [140]:

$$9 \cdot \mathbf{M}(NO_3)_{\boldsymbol{x}} + \left({}^{5}/_{2}\right)\boldsymbol{x} \cdot C_6H_8O_7 \rightarrow 15\boldsymbol{x} \cdot CO_2 + \left({}^{9}/_{2}\right)\boldsymbol{x} \cdot N_2 + 10\boldsymbol{x} \cdot H_2O + 9 \cdot \mathbf{M}O_{\left({}^{\boldsymbol{x}}/_{2}\right)}$$

where $\mathbf{M} = Ca^{2+}$ or Co^{2+}, $\boldsymbol{x} = 2$ for $Ca_3Co_4O_{9+\delta}$, and NO^{3-} acts as the oxidant and citric acid as the fuel. The idealized combustion reaction occurs with a citrate-to-nitrate molar ratio of about 0.28. Through tuning this ratio, the auto-combustion flame propagation and the heat evolution can be controlled. In this work, a series of citrate-to-nitrate molar ratios were chosen from 0.50 to the ideal value 0.28. With a ratio of 0.50, no auto-combustion occurred. In contrast, the flame propagated rapidly and vigorously at the ideal ratio of 0.28. These observations are consistent with the conclusion reported by Roy et al. who studied the $YBa_2Cu_3O_{7-x}$ system [141]; the excessive amounts of citric acid cannot induce the auto-combustion and the maximum heat evolution happens when the citric acid amount is slightly higher than the stoichiometric nitrate requirement. To promote complete chelation, the $Ca_3Co_4O_{9+\delta}$ powders were synthesized from gels with an excess amount of citric acid so that the citrate-to-metal cation molar ratio was 1, and the necessary amount of nitrate required to activate the auto-combustion was provided by NH_4NO_3 to give a citrate-to-nitrate molar ratio of 0.40.

Fig. 4.2(a) shows the TG/DTA curve of a dry $Ca_3Co_4O_{9+\delta}$ gel with a citrate-to-nitrate molar ratio of 0.40. The DTA curve can be divided into three main regions. Below 200 ℃ there are three peaks, one endothermic at 100 ℃ and two exothermic, at 150 and 190 ℃, accompanied by about 75 % weight loss. These peaks can be ascribed to the evaporation of residual water, the partial decomposition of nitrate and the initiation of the auto-combustion reaction, respectively [141]. In the second region from 250 to 350 ℃ one broad exothermic peak can be observed, which may be attributed to the decomposition of residual citric acid and results in an additional ~2 % weight loss. No exothermic peaks were observed between 400 and 500 ℃ indicating no residual citrate complexes. With the incorporation of the auto-combustion reaction, the starting precursors – $CaCO_3$ and Co_3O_4 – can be obtained at relatively low temperatures. The endothermic peak in the DSC curve displayed in Fig. 4.2(b) is a composite peak originating from the breakdown of $CaCO_3$ into CaO followed by the formation of the $Ca_3Co_4O_{9+\delta}$ phase. Although not presented here, comparison of the XRD patterns of the precursors after the initial furnace treatment at 425 ℃ with those of the sample reacted in the DSC confirm the origin of the peak to be a result of the formation of $Ca_3Co_4O_{9+\delta}$.

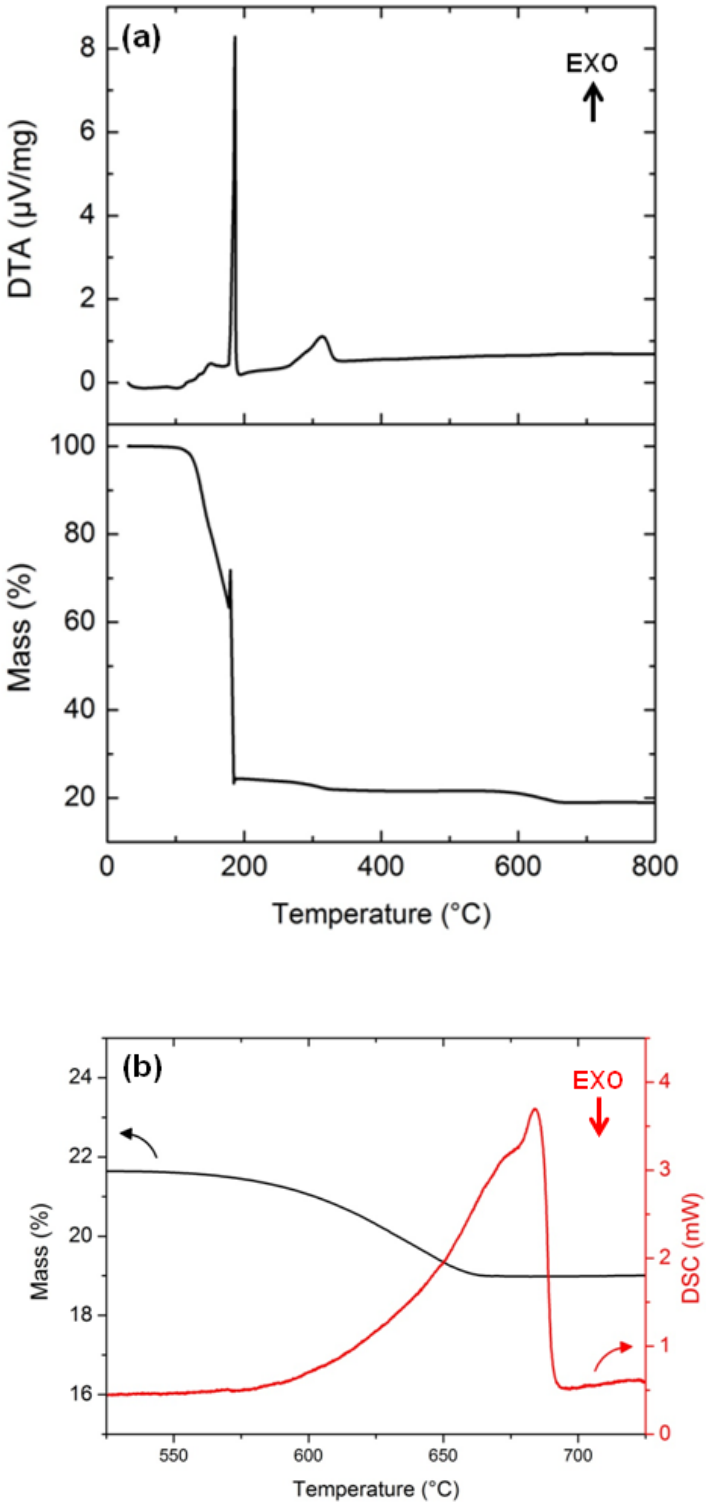

Fig. 4.2. (a) TG/DTA curves of the dry $Ca_3Co_4O_{9+\delta}$ citrate–nitrate gel, and (b) the enlarged region of the TGA curve from (a) overlaid with the independently DSC measurement exhibiting a complex peak originating from the thermal decomposition of $CaCO_3$ to CaO and the formation of the $Ca_3Co_4O_{9+\delta}$ phase.

XRD patterns of the $Ca_3Co_4O_{9+\delta}$ powders as-synthesized and after SPS consolidation at 850 ℃ are shown in Fig. 4.3. All the peaks could be indexed as $Ca_3Co_4O_9$ according to the JCPDSPDF # 21-0139 of $Ca_9Co_{12}O_{28}$ and the XRD patterns reported in the literature, indicating the purity and obvious texturing of these samples [63]. The inset in Fig. 4.3 displays the SEM micrographs of as-synthesized $Ca_3Co_4O_{9+\delta}$ particles with the average particle size of ~300 to 400 nm and a plate-like morphology. Fig. 4.4 shows a set of SEM micrographs of the sintered fracture surfaces after SPS processing at 850 ℃ for 5 min, which were observed along directions parallel and perpendicular to the SPS pressure axis. The platelet morphology and textured microstructure is observable in these two micrographs, which is also consistent with the anisotropic XRD results. All samples exhibited densities more than 99 % of the theoretical density, and these values agree with Liu et al., Kenfaui et al. and our previous works [43][68][142].

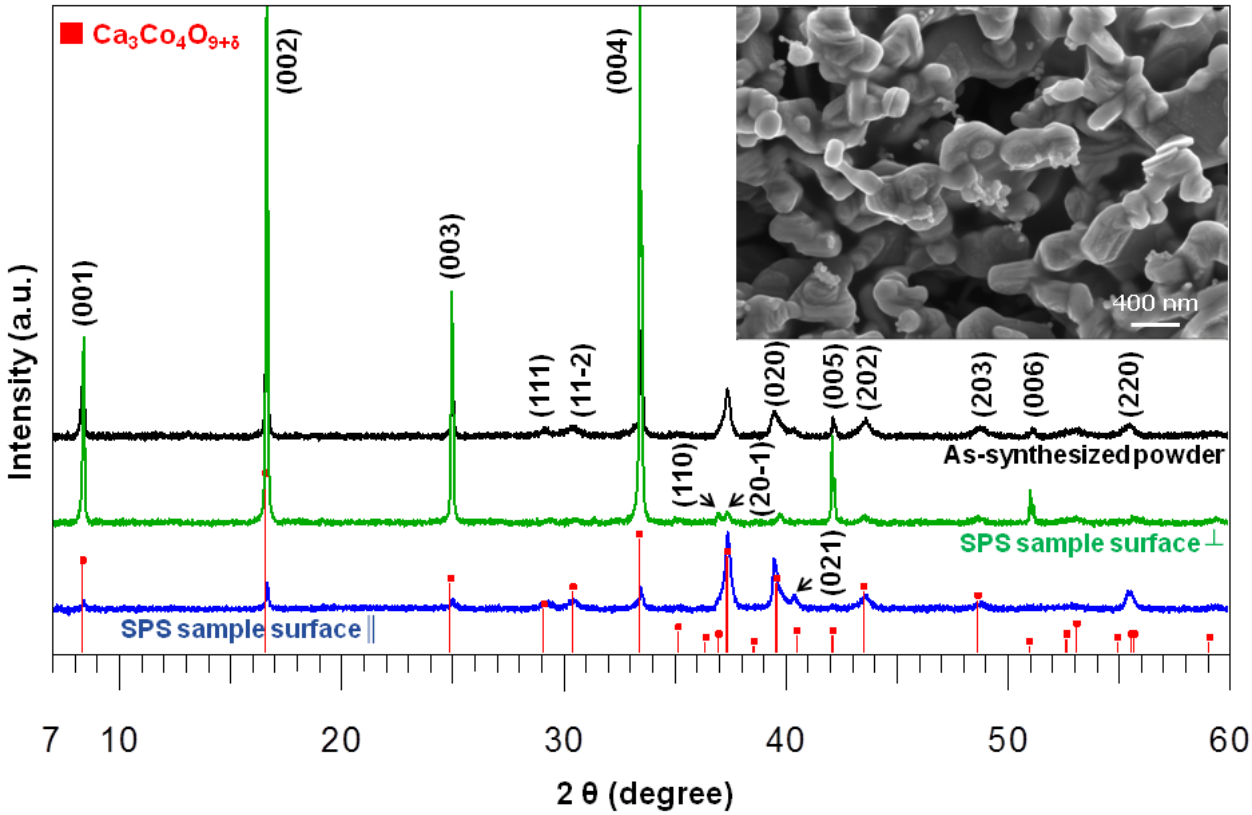

Fig. 4.3. XRD patterns of the as-synthesized $Ca_3Co_4O_{9+\delta}$ powders and the SPS consolidated samples. The red line pattern is from JCPDS PDF # 21-0139 for $Ca_3Co_4O_{9+\delta}$ phase identification. The inset is the SEM micrograph of the as-synthesized powders.

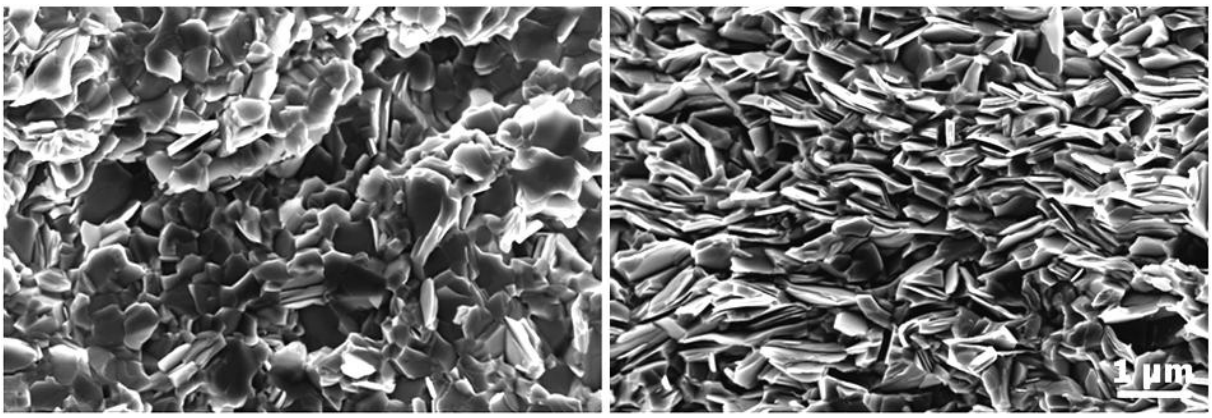

Fig. 4.4. SPS sample microstructure micrographs observed along directions parallel (left) and perpendicular (right) to the SPS pressure axis.

Due to the layered structure of $Ca_3Co_4O_{9+\delta}$ and the morphological anisotropy observed in this study, the thermoelectric properties were measured along both ⊥ and ∥ directions. Among samples which were densified by SPS at 700, 750, 800 and 850 ℃, the maximum deviation from the averages in the ⊥ direction electrical resistivity, the Seebeck coefficient and the thermal conductivity are 2.5 %, 1.1 % and 2.2 %, respectively, as measured at 700 ℃ (detailed data can be found in the appendix). These are all within the error of the measurements, and so to be consistent with our previous work on optimizing the SPS processing conditions for solid-state prepared $Ca_3Co_4O_{9+\delta}$. For simplicity, Fig. 4.5 shows only the results of the measurements performed on the sample processed by SPS at 850 ℃ for 5 minutes under 50 MPa of pressure [43]. The electrical resistivity in the plane perpendicular to the SPS pressure axis ($\rho_{\perp}$) varied between 5.24 mΩ·cm and 5.72 mΩ·cm throughout the measured temperature regime with a minimum value of 5.24 mΩ·cm at 650 ℃. These results are lower than those observed by Zhang et al. on a sample synthesized by the conventional citrate–nitrate method – 6.13 mΩ·cm cm at 700 ℃ [120]. To our knowledge, so far this is the lowest electrical resistivity value for pure polycrystalline $Ca_3Co_4O_{9+\delta}$ with the normal SPS processing. The electrical resistivity measured along the ∥ direction ($\rho_{\parallel}$) was found to be 15.32 mΩ·cm at 700 ℃, which is below the previous reported value of about 18 mΩ·cm at that temperature [120]. The low magnitude and high anisotropy of the electrical resistivity can be explained as a result of the enhanced morphological texturing of the sample. A quantitative analysis of the texturing can be obtained by assessing the volume fraction, $\boldsymbol{\alpha}_{(00l)}$, of *c*-axis oriented grains in the samples after SPS processing using the following equation [143]:

$$\boldsymbol{\alpha}_{(00l)} = \sum(\boldsymbol{I}_{00l}/\boldsymbol{I}^{*}_{00l}) \Big/ \sum(\boldsymbol{I}_{hkl}/\boldsymbol{I}^{*}_{hkl}),$$

where $\boldsymbol{I}_{hkl}$ stands for the measured intensity of the (hkl) peaks from the XRD spectrum of the surface perpendicular to the SPS pressure axis of the consolidated samples and $\boldsymbol{I}^{*}_{hkl}$ for those of the as-synthesized $Ca_3Co_4O_{9+\delta}$ powders. The auto-combustion powders exhibit a significant $\boldsymbol{\alpha}_{(00l)}$ value of up to 91 %, which is consistent with high degree of texturing indicated by the SEM observations. Due to the plate-like morphology of the as-synthesized $Ca_3Co_4O_{9+\delta}$ powders shown in the inset of Fig. 4.3, asymmetric necking during sintering occurs resulting in anisotropic surface energies that in turn produce torques to drive the grain rotation [144]. Therefore, sintering with small plate-like $Ca_3Co_4O_{9+\delta}$ particles may enhance microstructural anisotropy as the higher density of grain boundaries results in a higher concentration of grain rotation driving forces and therefore a higher degree of grain alignment. A benefit of the auto-combustion reaction is the rapid formation of the starting precursors at relatively low temperatures. This allows for the subsequent calcination period needed to achieve the $Ca_3Co_4O_{9+\delta}$ phase formation to be kept relatively short (2 h in this work). This limits the high temperature (above 700 ℃) particle size growth and therefore results in the enhancement of the anisotropy of the microstructure and the thermoelectric properties of the consolidated bulk samples. This conclusion corresponds well to Chen et al. work on the relationship between varied $Ca_3Co_4O_{9+\delta}$ calcination temperatures and particle sizes, which points out that the smallest $Ca_3Co_4O_{9+\delta}$ particle size calcinated at lower temperature after sintering exhibited the better grain alignment and higher thermoelectric performance [145]. The similar electrical conductivity improvement resulted from enhancing texturing also can be observed from other works. Both of Liu et al. and Kenfaui et al. works agreed that the SPS densification could improve the thermoelectric properties with grain orientation and higher bulk density [142][146]. With the assistance of the magnetic alignment technique and SPS processing, Zhou et al. reported a $\rho_{\perp}$ of about 6 mΩ·cm at 700 ℃ – exhibiting an improvement of about 30 % compared with the less textured sample [147]. Lin et al. later proposed that fabricating $Ca_3Co_4O_{9+\delta}$ by the SPS and a dynamic forging process can increase grain orientation, also increasing the electrical conductivity by about 30 % [148]. Recently, Noudem et al. enhanced the texturing by a modified SPS processing – so-called "edge-free" spark plasma sintering, and at 550 ℃ a 30 % improvement in the electrical resistivity (7 mΩ·cm) and a power factor of 400 $\mu W/m{\cdot}K^2$ was obtained [130]. Except SPS processing, the reactive-templated grain growth (RTGG) method is a means to achieve highly texturing $Ca_3Co_4O_{9+\delta}$ and it also demonstrated that the lowest electrical resistivity was from the most texturing sample, yielding a resistance of 3.8 mΩ·cm at about 800 ℃ [149]–[152].

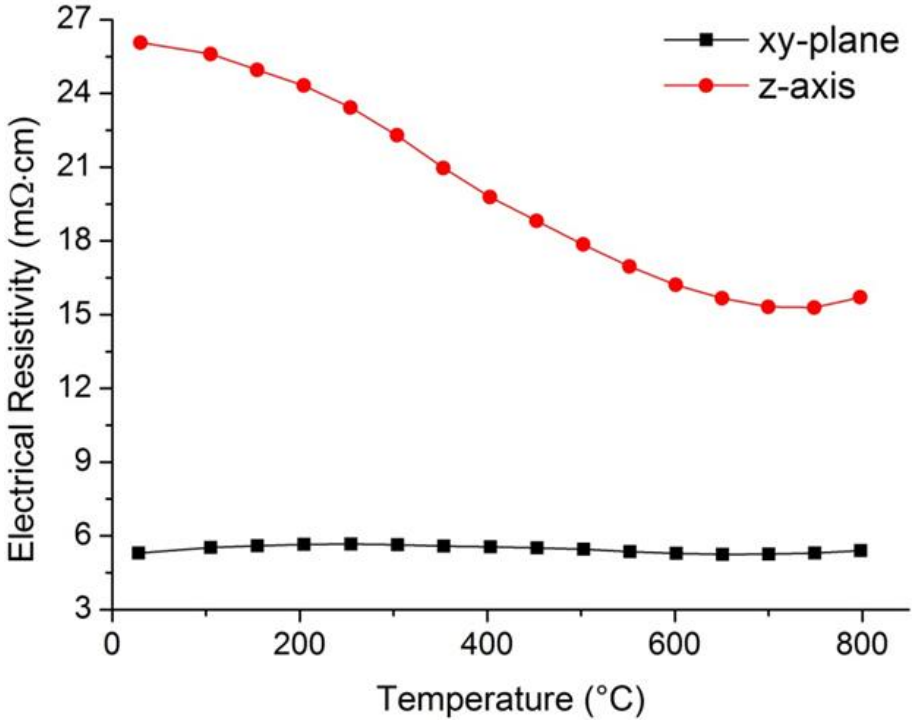
xy-plane
z-axis
Electrical Resistivity (mΩ·cm)
27
24
21
18
15
12
9
6
3
0
200
400
600
800
Temperature (°C)

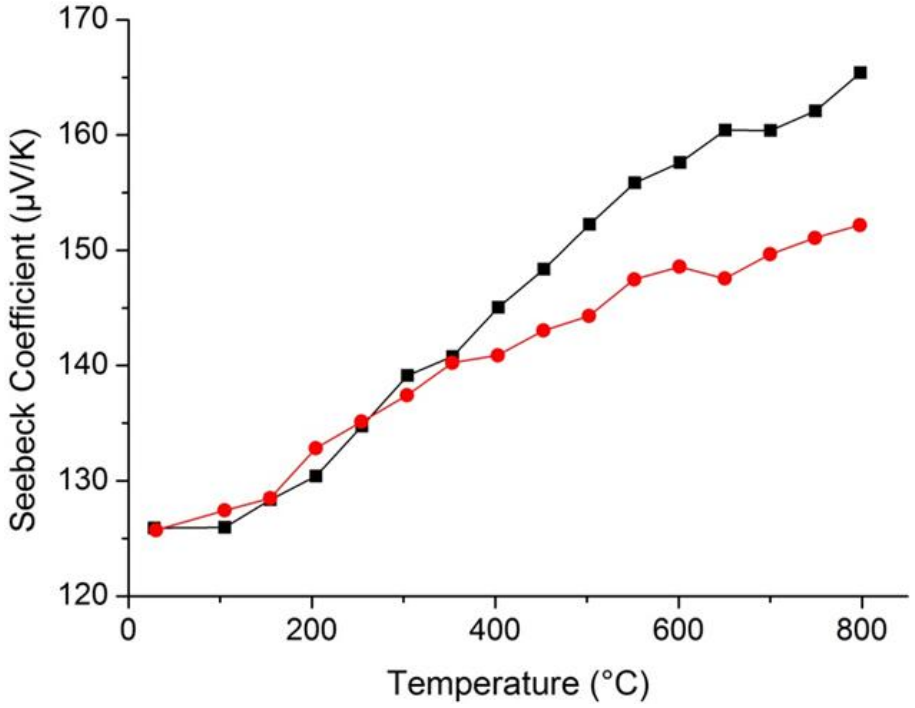
Seebeck Coefficient (μV/K)
170
160
150
140
130
120
0
200
400
600
800
Temperature (°C)

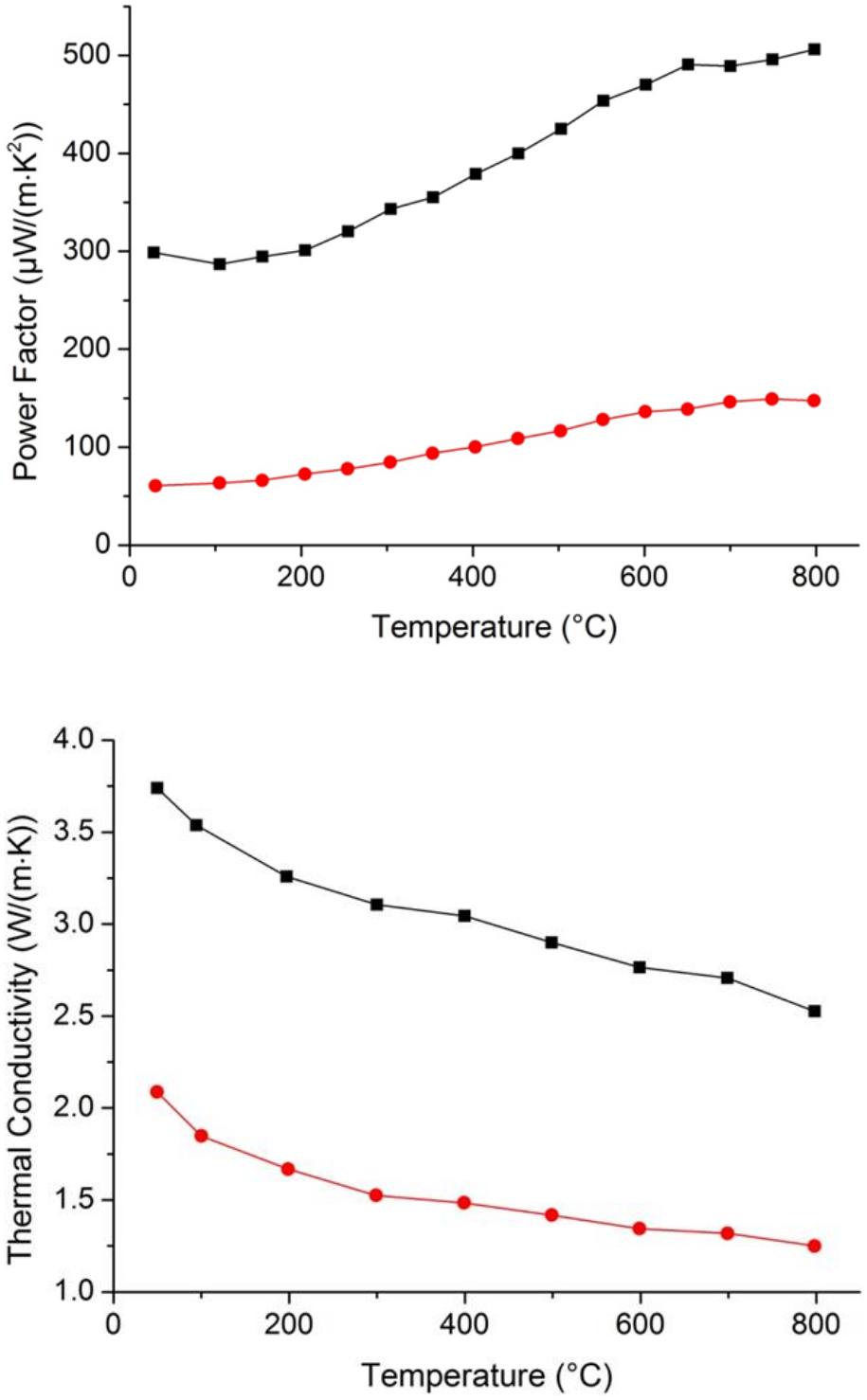

Fig. 4.5. The temperature dependence of the thermoelectric properties measured along the ⊥ and ∥ directions.

The temperature dependence of the Seebeck coefficient and power factor ($PF = S^2/\rho$) along both directions can also be seen in Fig. 4.5. The Seebeck coefficient increases with temperature, and the anisotropy between ⊥ and ∥ directions is not as pronounced as much as the electrical resistivity, which is consistent with the results of Tani et al. and Zhang et al. reporting the Seebeck coefficient to be insensitive to the grain orientation [120][149]. The highest Seebeck coefficient value of 165 $\mu V/\mathrm{K}$ was measured at 800 ℃ within the ⊥ direction, which is comparable with reported values of samples synthesized by wet-chemical methods [120][136][137]. Due to the lower ρ and higher S within the ⊥ plane, $PF_{\perp}$ remains higher than $PF_{\parallel}$ throughout the whole temperature range with amaximum value of $PF_{\perp} \approx 500\ \mu\mathrm{W/m{\cdot}K^2}$ at 800 ℃. At 700 ℃ the value is ~490 $\mu\mathrm{W/m{\cdot}K^2}$ – about 10 % higher than reported for samples produced by the conventional citrate-nitrate reaction (about 445 $\mu\mathrm{W/m{\cdot}K^2}$) with similar SPS condition [120]. This enhanced $PF_{\perp}$, which was obtained by the auto-combustion synthesis and normal SPS processing, approaches that of samples prepared by more time costly processes such as the RTGG processing and repeated hot-pressing [135][149][150][152].

The thermal conductivities (κ) measured along ⊥ and ∥ directions shown also in Fig. 4.5 decrease with the temperature, which is comparable with the reported results from $Ca_3Co_4O_{9+\delta}$ single crystal and polycrystalline samples [67][135]. κ contains both the electronic (κ_e) and the lattice (κ_L) contributions (i.e., $\kappa = \kappa_e + \kappa_L$), but by applying the Wiedemann–Franz relationship, $\kappa_e = L_0 T/\rho$, where the Lorenz factor is taken as $L_0 = 2.44\times10^{-8}\ \mathrm{V^2/K^2}$, the lattice contribution was calculated and accounts for more than 80 % of the total in both directions [67][133][153]. Since $Ca_3Co_4O_{9+\delta}$ consists of alternating misfit-layers of CoO_2 and Ca_2CoO_3, anisotropy in the thermal and electrical transport properties is expected. Although achieving lower $\rho_{\perp}$ by enhancing grain alignment is a promising and effective route to obtaining higher $PF_{\perp}$, it will lead to the increase of the κ_e contribution in total κ and compromise the thermoelectric performance in $ZT_{\perp}$, which may be observed from works with the RTGG processing and repeated hot-pressing [135][150]. The relationship of the degree of texturing and the anisotropy in the transport properties will be the focus of future studies.

Fig. 4.6 displays the temperature dependence of ZT calculated for both directions. At 800 ℃, $ZT_{\perp}$ and $ZT_{\parallel}$ were found to be 0.21 and 0.13, respectively, and these values are among the highest ZT values reported for pure bulk polycrystalline $Ca_3Co_4O_{9+\delta}$ comparable to those synthesized via the hydrothermal treatment ($ZT_{\perp} \approx 0.27$ at 750 ℃ [71]), or processed with the RTGG ($ZT_{\perp} \approx 0.26$ at 800 ℃ [149][152]) and repeated hot-pressing ($ZT_{\perp} \approx 0.24$ at 800 ℃ [135]). However, it should be noted that the in-plane thermal conductivity used for the calculation of $ZT_{\perp}$ of the sample produced by the RTGG was measured on a sample exhibiting a lower electrical conductivity (and therefore a lower electronic contribution to the thermal conductivity) than the sample from which the power factor was taken [150]. Also, the value of $ZT_{\perp}$ at 800 ℃ of the sample prepared by repeated hot-pressing was extrapolated from a fit equation provided in the reference – the measured data only extends to 650 ℃ [135]. When

considering that the ratio of $ZT_{\perp}/ZT_{\parallel}$ and $PF_{\perp}/PF_{\parallel}$ are 1.62 and 3.44, the ⊥ plane can be expected to be a preferred direction for preparing thermoelectric legs.

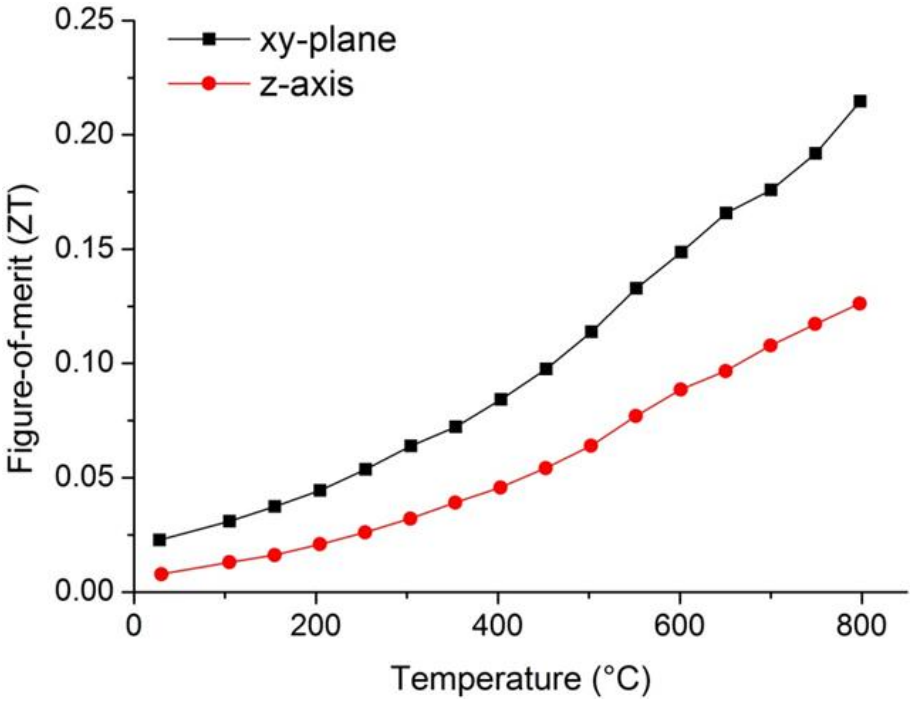

Fig. 4.6. The temperature dependence of the *ZT* measured along the ⊥ and ∥ directions.

4.4 Conclusion

In this work, a new rapid synthesis method of producing $Ca_3Co_4O_{9+\delta}$ fine powders using an auto-combustion synthesis method is demonstrated. The auto-combustion is induced by carefully tuning the ratio of citrate to nitrate based on the conventional sol–gel process. The synthesized $Ca_3Co_4O_{9+\delta}$ powders were consolidated by SPS and the anisotropic thermoelectric properties were measured parallel and perpendicular to the SPS pressure axis. The auto-combustion synthesis provides an efficient and rapid method for producing pure polycrystalline $Ca_3Co_4O_{9+\delta}$ with a high power factor and *ZT* in the plane perpendicular to the SPS pressure axis of about 500 $\mu W/m{\cdot}K^2$ and 0.21 at 800 ℃, respectively. Moreover, the auto-combustion synthesis can be applied not only to pure but also doped $Ca_3Co_4O_{9+\delta}$ for further thermoelectric performance improvement.

4.5 Supplementary Data

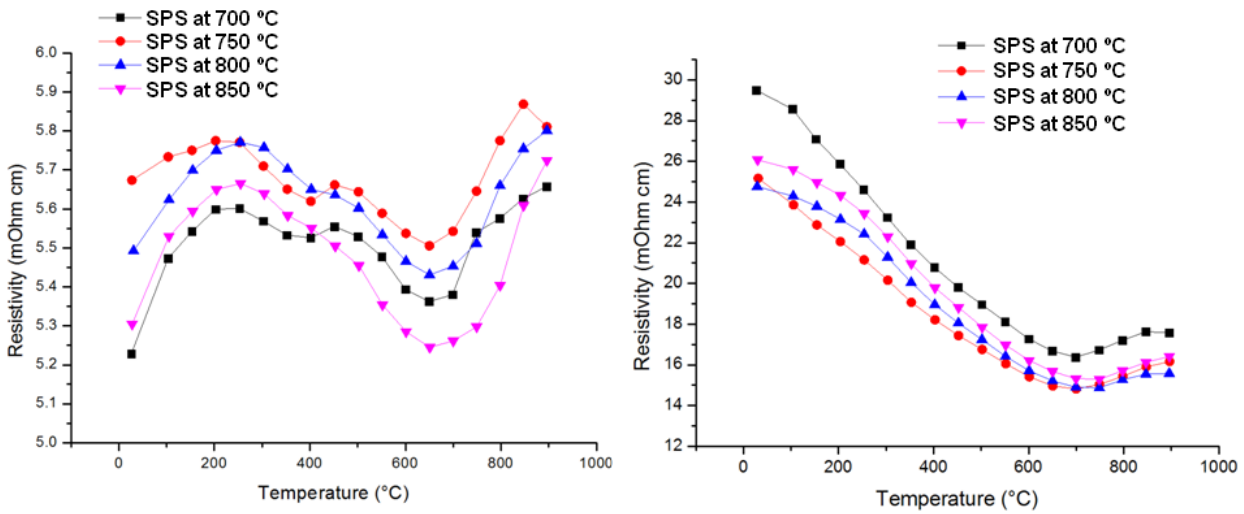

Temperature dependence of the electrical resistivity measured along the ⊥ (left) and ∥ (right) directions with varied SPS sintering temperatures (700 ℃ to 850 ℃).

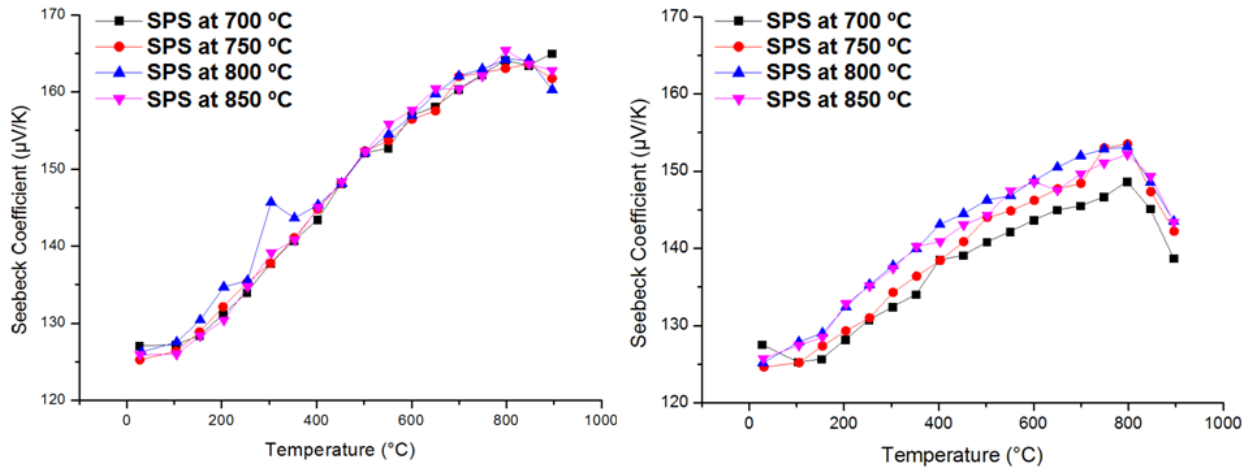

Temperature dependence of the Seebeck coefficient measured along the ⊥ (left) and ∥ (right) directions with varied SPS sintering temperatures (700 ℃ to 850 ℃).

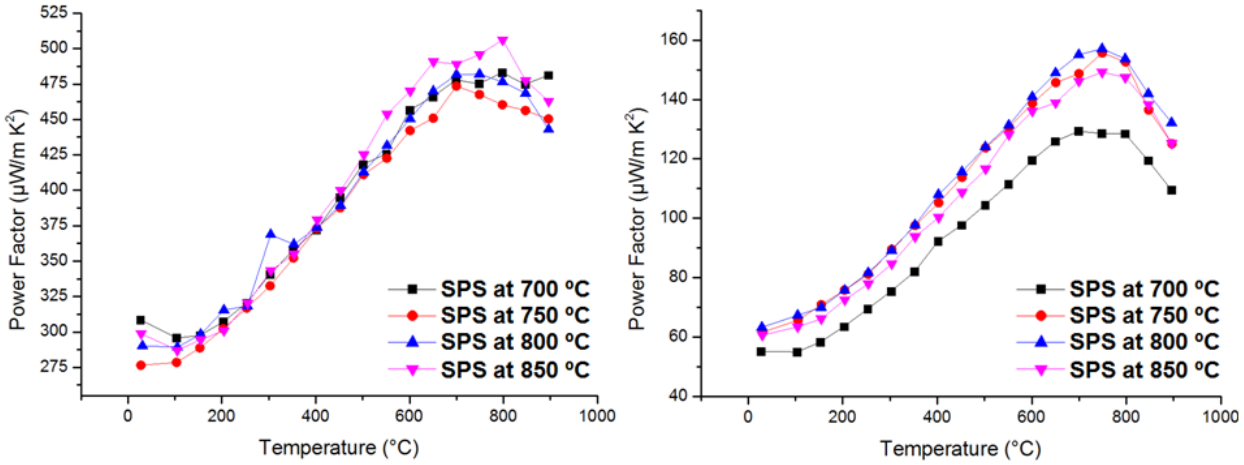

Temperature dependence of the in-plane ($PF_{\perp}$, left) and out-of-plane ($PF_{\parallel}$, right) power factor with varied SPS sintering temperatures (700 ℃ to 850 ℃).

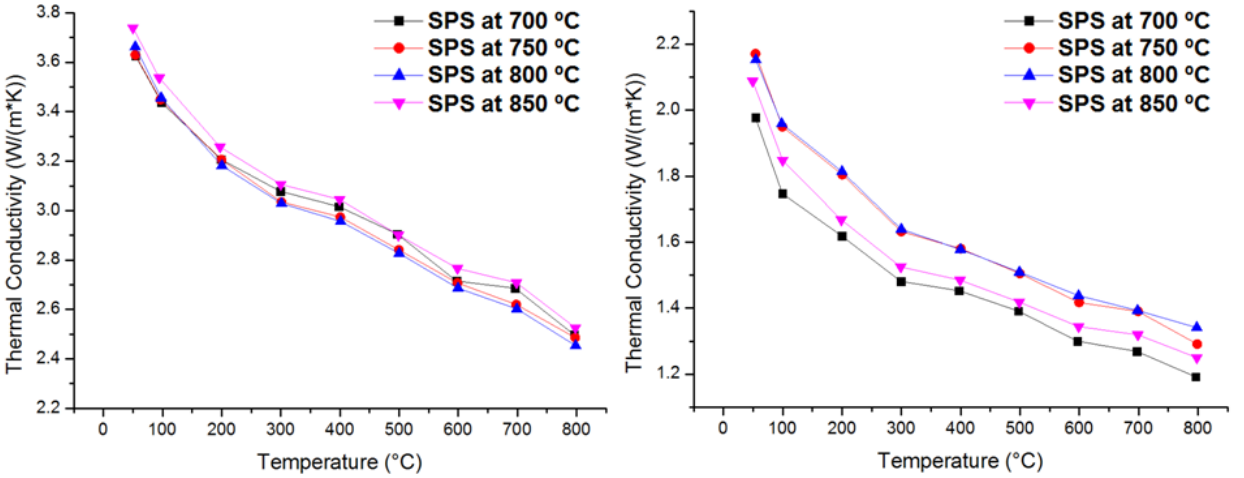

Temperature dependence of the thermal conductivity measured along the ⊥ (left) and ∥ (right) directions with varied SPS sintering temperatures (700 ℃ to 850 ℃).

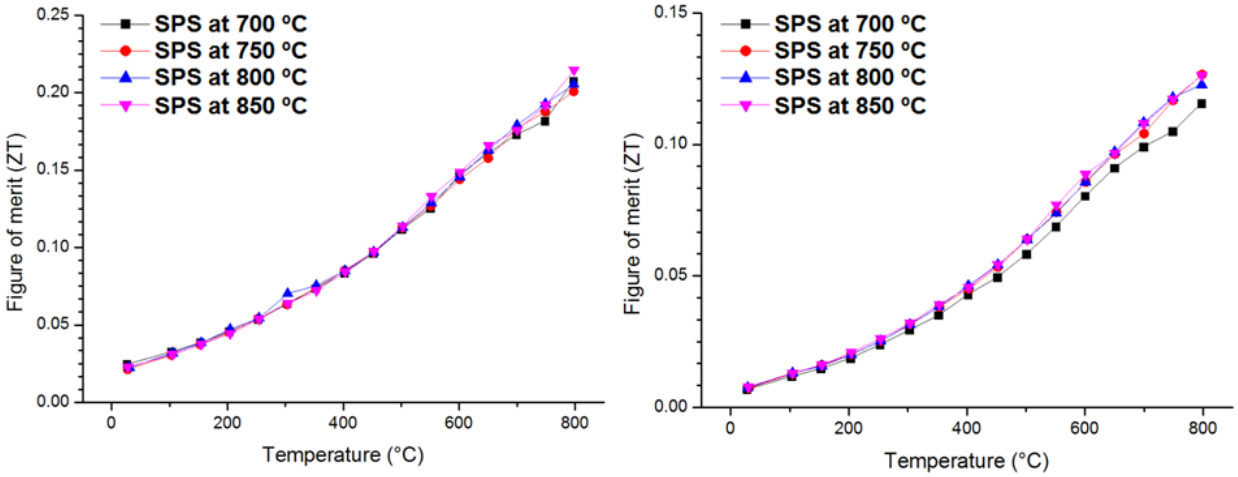

Temperature dependence of the in-plane ($ZT_{\perp}$, left) and out-of-plane ($ZT_{\parallel}$, right) figure-of-merit with varied SPS sintering temperatures (700 ℃ to 850 ℃).

Chapter 5

Effects of Y and Fe co-doping on the High Temperature Thermoelectric Properties of $Ca_3Co_4O_{9+\delta}$

Abstract

A series of Fe and Y co-doped $Ca_{3-x}Y_xCo_{4-y}Fe_yO_{9+\delta}$ ($0 \leq x \leq 0.3$, $0 \leq y \leq 0.1$) samples synthesized by auto-combustion reaction and followed by a spark plasma sintering (SPS) processing with the effects of Fe and Y doping on the high temperature (room temperature to 800 ℃) thermoelectric properties were systematically investigated. For the Fe-doped system ($x = 0$, $y \leq 0.1$), the electrical resistivity (ρ) decreased over the whole measured temperature range, while the Seebeck coefficient (S) remained almost the same. For the co-doped system, at any fixed Fe doping content, both ρ and S tended to increase with increasing Y dopants, however, the effect is more substantial on ρ than on S, particularly in the low temperature regime. In contrast to ρ and S, the in-plane thermal conductivity (κ) is only slightly influenced by Y and Fe substitutions. Among all the investigated samples, the co-doped sample with $x = 0.1$ and $y = 0.03$ showed a decrease of ρ, 13 % enhanced power factor over the measured temperature range, and 17 % improved ZT at 800 ℃ as compared to un-doped $Ca_3Co_4O_{9+\delta}$.

This chapter is prepared as a journal article: N. Wu, N. V. Nong, N. Pryds, and S. Linderoth, "Effects of Y and Fe co-doping on the High Temperature Thermoelectric Properties of $Ca_3Co_4O_{9+\delta}$".

5.1 Introduction

Thermoelectric (TE) materials arouse a great deal of interest owing to the possibility of directly converting thermal energy into electrical energy via the Seebeck effect. The efficiency of TE materials can is proportional to the dimensionless figure-of-merit $ZT = S^2T/\rho\kappa$, which consists of the Seebeck coefficient (S), electrical resistivity (ρ), thermal conductivity (κ) and absolute temperature (T). Oxides are one of the promising candidate material classes for high temperature TE applications due to low cost, abundance of the constituent elements, and high-temperature structural and chemical stabilities in air [67][70]. In this class, p-type $Ca_3Co_4O_{9+\delta}$ has gained much attention after the discovery by Shikano et al. with a ZT of 0.83 (at 800 ℃) for a single crystalline sample as a promising high temperature thermoelectric p-type oxide material [67].

$Ca_3Co_4O_{9+\delta}$ (abbreviated Co349 in the following text) possesses a misfit-layered structure with a CdI_2-type hexagonal CoO_2 subsystem and a rock salt-type Ca_2CoO_3 subsystem that are alternately stacked along the c-axis with identical a, c and β parameters but different and incommensurate b parameters. Therefore, this misfit-layered oxide can be described as $[Ca_2CoO_3][CoO_2]_{(b1/b2)}$ with a $b1$ to $b2$ ratio of approximately 1.62, where $b1$ to $b2$ are two lattice parameters for the rock salt and CoO_2 subsystems respectively [63][66]. As a p-type material, the hole charge conduction takes place mainly within the CoO_2 layer with the Ca_2CoO_3 layer serving as a charge reservoir, and the misfit between layers is expected to hinder the phonon transport [133][154].

Though Co349 single crystals have been known to exhibit competitive ZT values at high temperatures, polycrystalline Co349 exhibits a much lower ZT value of about 0.2 at 800 ℃ [44]. To improve the ZT of the polycrystalline Co349, many efforts have been made by atomic substitutions for Ca or Co with the purpose of adjusting the carrier concentration or hindering phonon transport via mass fluctuation in order to optimize ZT [70][71][119][121][122][153] [155]–[163]. On the basis of the reported data, it shows that the substitution of Y on the Ca-site results in some improvements of the TE properties of Co349 [121][122][153]. Y^{3+} substitution for Ca^{2+} ions would reduce the Co effective oxidation states in Co349 leading to a decrease in the hole (i.e., Co^{4+}) concentration and therefore an enhancement of S. Additionally, since Y^{3+} is heavier than Ca^{2+}, Y substitution may diminish the phonon mean free path resulting in the reduction of κ. An optimal Y doping content of 0.2 was often reported [122][153]. Y dopants may therefore induce merits to enhance S and reduce κ, but the increase of ρ still remains a critical issue that need to be mitigated to achieve an enhancement in ZT [121][122][153].

Many reports have surveyed the transition metals such as Cr, Mn, Fe, Ni, Cu, and Zn as possible dopants for Co with respect to the TE properties of Co349 [119][158][159][161]–[163]. The influence of substitutions on the Co-site is more complicated than on the Ca-site in Co349 due to the intrinsic feature of multiple oxidation states of the transition metals as dopants as well

as the presence of the two non-equivalent Co sites in the Ca_2CoO_3 and CoO_2 subsystems [38][39][119][158]–[161]. Among the above mentioned dopants, the Fe-doped $Ca_3Co_{4-x}Fe_xO_{9+\delta}$ ($x \leq 0.2$) system was reported to show a simultaneous increase of S and decrease of ρ in the temperature regime below room temperature [161][163]. The reason for S increase was interpreted to be due to a strong electron correlation effect, while the decrease in ρ was attributed to the change in carrier concentration [158][161][162].

In this work, a series of Co349 with various Fe/Y co-doping contents were prepared in order to investigate the effect of these elements on the high temperature thermoelectric properties. Firstly, a series of the Fe-doped $Ca_3Co_{4-y}Fe_yO_{9+\delta}$ ($0 \leq y \leq 0.1$) was investigated, and secondly, Fe/Y co-doped $Ca_{3-x}Y_xCo_{4-y}Fe_yO_{9+\delta}$ ($0 \leq x \leq 0.3$, $0 \leq y \leq 0.1$) systems were prepared and characterized. The thermoelectric properties from room temperature to 800 ℃ and the co-doping effects are presented and discussed.

5.2 Experimental Procedure

Polycrystalline $Ca_3Co_4O_{9+\delta}$ samples with Fe doping, and Fe/Y co-doping were prepared by an auto-combustion synthesis technique similar to that which is described in Ref. [44]. A stoichiometric ratio of analytical regent grade (99+ %) $Ca(NO_3)_2{\cdot}4H_2O$, $Co(NO_3)_2{\cdot}6H_2O$, $Y(NO_3)_3{\cdot}6H_2O$ and $Fe(NO_3)_3{\cdot}9H_2O$ were dissolved in de-ionized water with a specific amount of citric acid (99+ %) to keep the citrate–metal cation molar ratio at 1. Additionally, the citrate-to-nitrate molar ratio was maintained at 0.40 by introducing NH_4NO_3 (98+ %). After drying the solution until a uniform viscous gel was obtained, the hot plate temperature was raised to about 250 ℃ to initiate the auto-combustion process. The resulting powders were calcined at 750 ℃ for 2 hours to obtain single phase $Ca_3Co_4O_{9+\delta}$ as confirmed by X-ray diffraction.

Subsequently, the powders were consolidated by a spark plasma sintering (SPS, Dr. Sinter SPS-515S, Fuji Electronic Industrial Co., Ltd.). Powders were poured into a 12.7 mm diameter graphite die to fabricate 10 mm-thick pellets. A pulsed electric current was then passed through the powders under vacuum (10^{-3} bar) to consolidate the material. Based on previous results, the sintering temperature was chosen to be 800 ℃, with a fixed uniaxial pressure of 50 MPa and a ramping rate of 100 ℃/min. The sintering time was kept constant for 5 min [43][44].

X-ray powder diffraction (XRD) patterns at room temperature were collected using a Bruker D8 diffractometer with Cu K_α-radiation to identify the phase composition of as-synthesized powders and SPS-sintered bulks. TE transport properties presented in this work were measured along the direction perpendicular to the SPS pressure axis (in-plane) [44]. The Seebeck coefficient (S) and electrical resistivity (ρ) measurements were carried out simultaneously with an ULVAC-RIKO ZEM3 from room temperature up to 800 ℃ under a low-pressure helium atmosphere. The thermal conductivity was calculated using the equation $\kappa = \rho \cdot \alpha \cdot c_p$ (where ρ, α and c_p are the density, thermal diffusivity and specific heat capacity, respectively). The thermal

diffusivity was obtained under vacuum in a NETZSCH LFA-457 laser flash system. The c_p in this work was taken to be the temperature independent Dulong–Petit limit. The bulk density of each sample was obtained with a Micromeritics AccuPyc 1340 gas pycnometer as an average of ten measurements. All samples exhibited densities more than 99 % of the theoretical densities. The theoretical density 4.68 g/cm^3 for the un-doped Co349 was determined based on the lattice parameters from Masset et al. [63]. Variations in the TE properties (ρ, S, κ) of multiple samples taken from the same composition remained below 1 %, which was taken into consideration in the subsequent comparison and discussion.

5.3 Result and Discussion

XRD analysis revealed that all Fe-doped and Fe/Y co-doped samples are single phase of Co349. Fig. 5.1 shows typical XRD patterns obtained for the as-synthesized and the SPS-sintered samples of the un-doped Co349, Fe-doped $Ca_3Co_{3.9}Fe_{0.1}O_{9+\delta}$ (Fig. 5.1(a)) and co-doped $Ca_{2.7}Y_{0.3}Co_{3.9}Fe_{0.1}O_{9+\delta}$ (Fig. 5.1(b)). All peaks were indexed as $Ca_3Co_4O_{9+\delta}$ according to the JCPDS PDF # 21-0139 and the XRD pattern reported by Masset et al. [63]. Fig. 5.2 shows a set of SEM micrographs of fracture surfaces of the un-doped Co349 and co-doped $Ca_{2.7}Y_{0.3}Co_{3.9}Fe_{0.1}O_{9+\delta}$ after the SPS processing. A fine platelet morphology with elongation along the direction perpendicular to the SPS pressure axis is observed in these two micrographs. All samples exhibit high densities of more than 99 % of the theoretical density. These values are in agreement with the works of Liu et al. and Kenfaui et al. as well as our previous work [44][68][142].

Fig. 5.3 shows the resistivity (ρ) as a function of temperature for the Fe-doped $Ca_3Co_{4-y}Fe_yO_{9+\delta}$ with $0 \leq y \leq 0.1$ (Fig. 5.3(a)) and for the Fe/Y co-doped $Ca_{3-x}Y_xCo_{4-y}Fe_yO_{9+\delta}$ series with $0.1 \leq x \leq 0.3$ and $0.03 \leq y \leq 0.1$ (Fig. 3(b–d)). The resistivity of the un-doped sample is also plotted for comparison. The Fe-doped samples exhibit lower resistivity values than the un-doped Co349 over the whole measured temperature range (Fig. 5.3(a)). This resulting decrease in ρ upon Fe doping is similar to the reported observations below room temperature [158][159][161]–[163]. Wu and Liu et al. have reported that the decrease in ρ with Fe dopant content $y \leq 0.10$ below room temperature is associated with the increasing carrier concentration due to the oxygen content change [158][162]. Additionally, it was also reported that the structure of the conducting CoO_2 layer becomes more ordered upon Fe doping, resulting in the increase of the carrier mobility owing to the suppression of scattering sites [158]. In Fig. 5.3(a), however, no clear monotonic change in ρ was observed with Fe dopant content. The lowest value was obtained with a Fe dopant content of 0.05 in the temperature range above 300 °C.

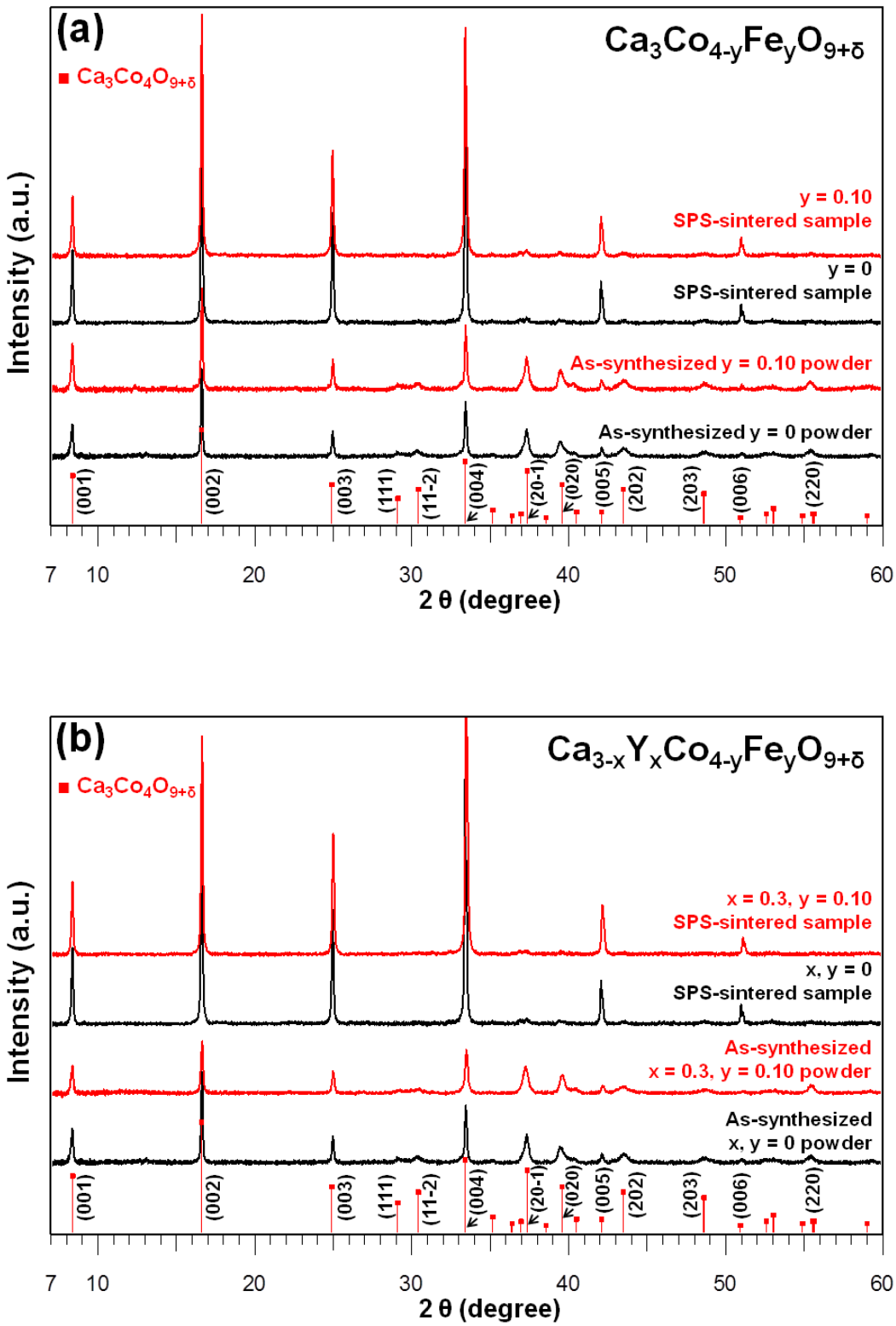

Fig. 5.1. XRD patterns of the as-synthesized powders and SPS-sintered pellets of the un-doped Co349, $Ca_3Co_{3.9}Fe_{0.1}O_{9+\delta}$ (a) and $Ca_{2.7}Y_{0.3}Co_{3.9}Fe_{0.1}O_{9+\delta}$ (b). The peaks with indices at the bottom are for the $Ca_3Co_4O_{9+\delta}$ phase identified by JCPDS PDF # 21-0139.

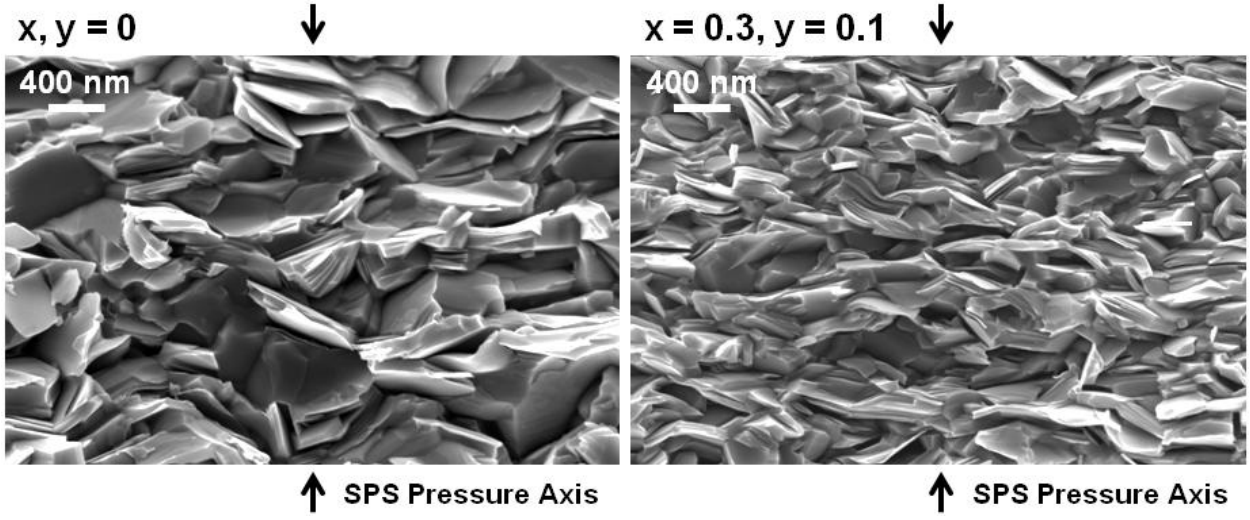

Fig. 5.2. SEM images of the fracture surface of a typical SPS-sintered un-doped Co349 (left) and co-doped $Ca_{2.7}Y_{0.3}Co_{3.9}Fe_{0.1}O_{9+\delta}$ (right) samples observed along the direction perpendicular to the SPS pressure axis.

In Fig. 5.3(b–d), a clear tendency of the increasing ρ with Y dopant content can be observed for all co-doped systems. Similar observations were also found by Wang et al. on Y-doped Co349 [153]. A possible reason was suggested that the trivalent Y^{3+} substitutions for the divalent Ca^{2+} ions may reduce the Co^{4+} (hole) concentration in order to balance the net valence of the system, leading to the increase in ρ [121][122][153]. However, it should be noted that with $x \geq 0.05$, ρ values are usually higher than those of the un-doped Co349 [121][122][153]. In the Fe/Y co-doped system, the sample with $x = 0.1$ and $y = 0.03$ showed a lower ρ value than the un-doped Co349 over the whole measured temperature range. With the same Y dopant content of $x = 0.1$ (Fig. 5.3(b–d)), ρ tended to increase with Fe dopant content.

Fig. 5.4 shows the Seebeck coefficient (S) at room temperature, 400 and 750 ℃ as a function of dopant contents for the Fe-doped $Ca_3Co_{4-y}Fe_yO_{9+\delta}$ and co-doped systems. For Fe-doped system (Fig. 5.4(a)), although the Fe dopant content was varied, similar S values as the un-doped Co349 can be observed over the whole temperature range. Wang et al. and Liu et al. have shown that S of the Fe-doped system below room temperature was enhanced accompanied with decreasing ρ [161][163]. The explanation for the increase in S upon Fe doping was contributed from the strong electronic correlation with a larger electronic specific heat [161][164]. The observed insensitivity of S to Fe substitution above room temperature (Fig. 5.4(a)), according to the modified Heikes formula [38], might stem from no significant Co^{4+}/Co^{3+} concentration change and the fact that the Co spin-state observed by Wu et al. and Liu et al. is maintained [158][162].

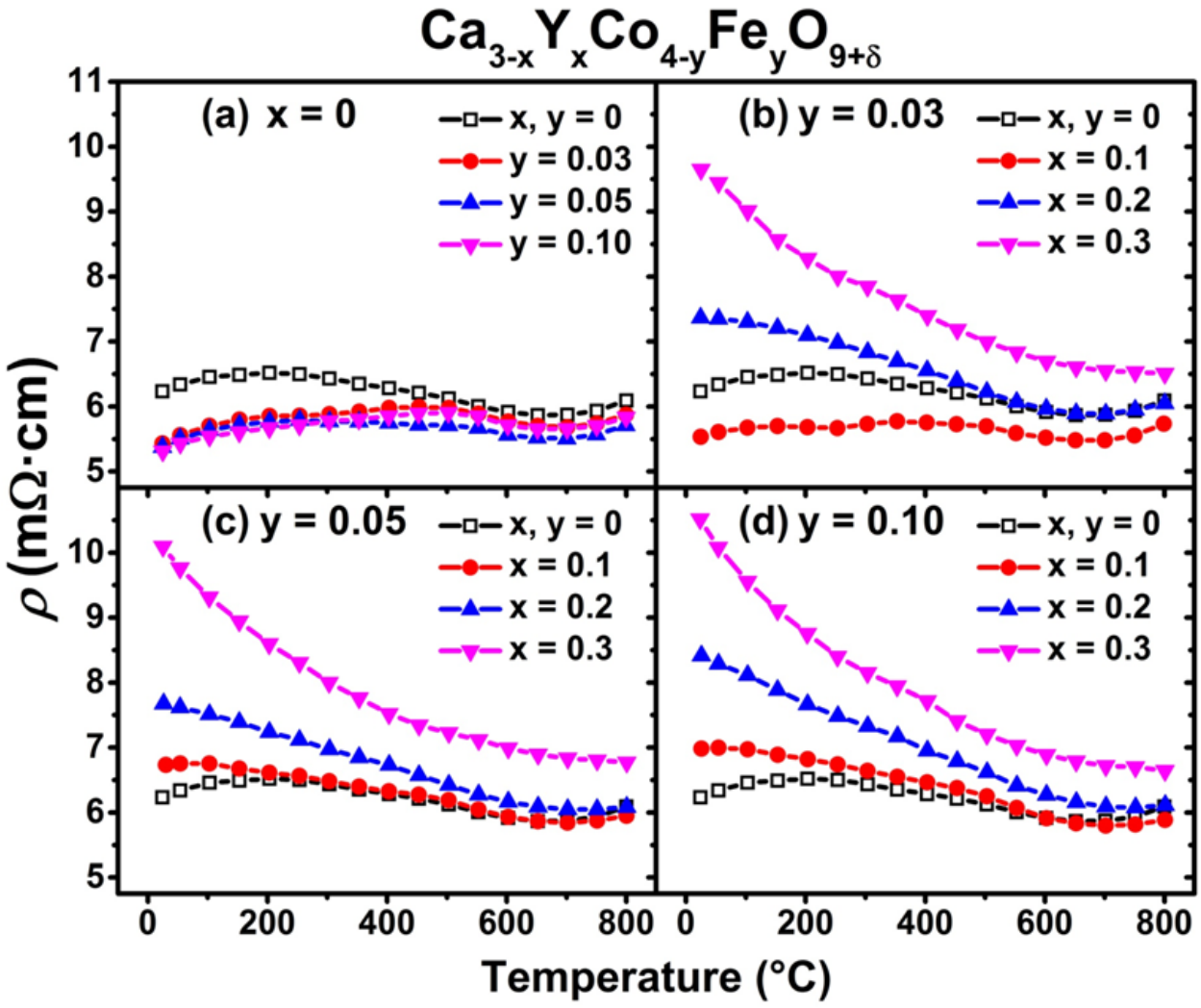

Fig. 5.3. The temperature dependent electrical resistivity (ρ) of the un-doped and $Ca_{3-x}Y_xCo_{4-y}Fe_yO_{9+\delta}$ series. The samples with varied dopant content are sorted into four groups: (a) Fe-doped $Ca_3Co_{4-y}Fe_yO_{9+\delta}$ samples with y = 0.03, 0.05, and 0.10. Samples of the fixed Fe content (b) y = 0.03, (c) y = 0.05 and (d) y = 0.10 with x varying from 0.1, 0.2 and 0.3. Open symbol denotes ρ of the un-doped Co349 as a reference.

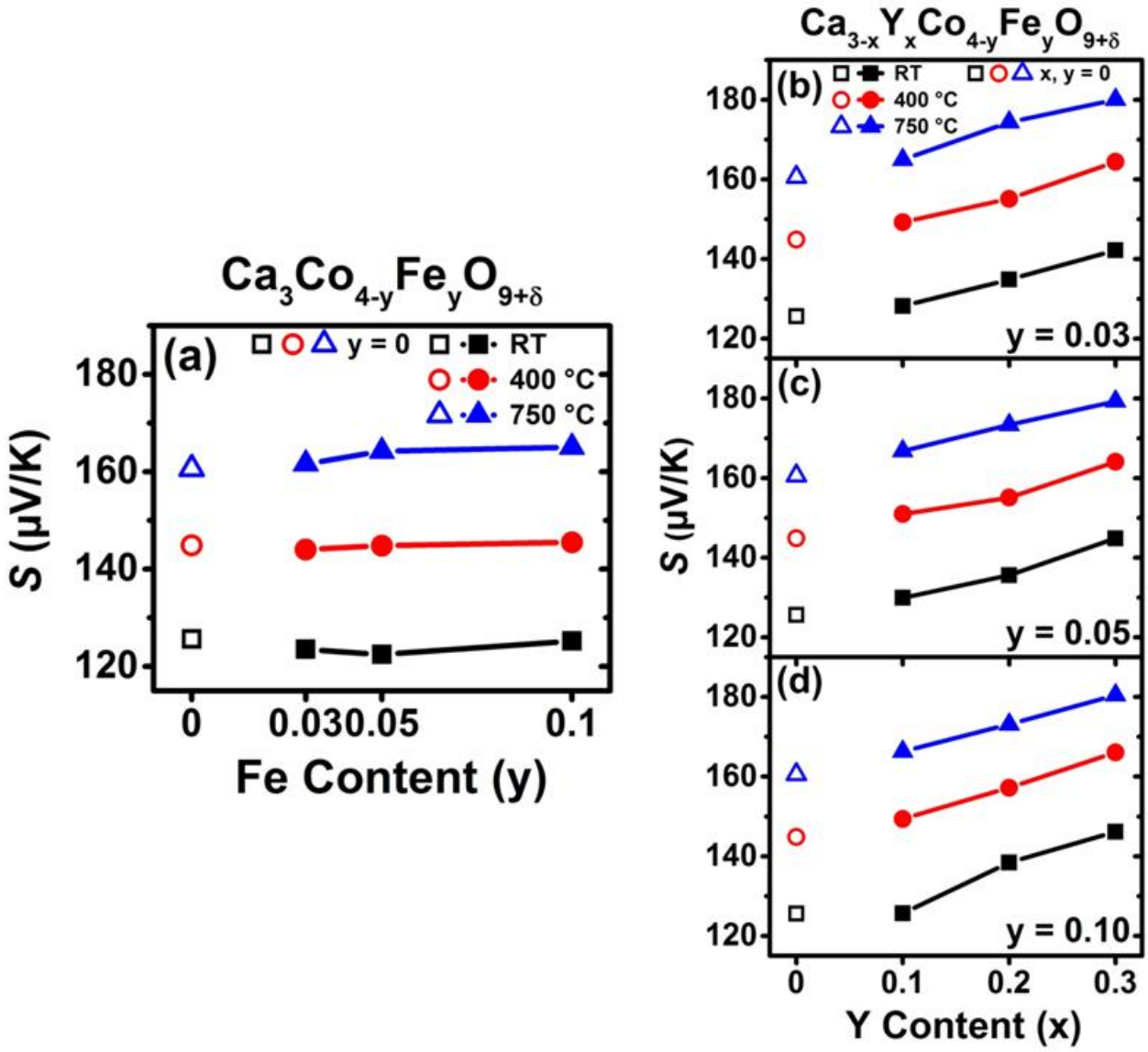

Fig. 5.4. The dependence on doping of the Seebeck coefficient (*S*) of the un-doped and $Ca_{3-x}Y_xCo_{4-y}Fe_yO_{9+\delta}$ series. The samples with varied dopant content are sorted into four groups: (a) Fe-doped $Ca_3Co_{4-y}Fe_yO_{9+\delta}$ samples with y = 0.03, 0.05, and 0.10. Samples of the fixed Fe content (b) y = 0.03, (c) y = 0.05 and (d) y = 0.10 with x varying from 0.1, 0.2 and 0.3. Open symbol denotes *S* of the un-doped Co349 as a reference.

As for the co-doped system, a clear tendency of the increase in *S* with Y dopant content was observed at any typical temperatures of room temperature, 400 ℃, and 750 ℃. The increase in *S* coupled with the increase in ρ could be due to the decrease in hole concentration caused by the substitution of Y^{3+} for Ca^{2+}. A similar behavior was also observed in the case of the Y-doped Co349 [121][122][153]. This resulting trend further demonstrates that the doping merits may be inherited to the co-doped system.

Fig. 5.5 presents the power factor (*PF*) as a function of temperature for the Fe-doped and Fe/Y co-doped systems studied in this work. *PF* of the un-doped Co349 sample was also plotted as a reference. For the Fe-doped samples, as a result of the reduction in ρ combined with an unchanged *S*, *PF* was enhanced throughout the investigated temperatures. Additionally, since Y doping resulted in an increase in *S*, accompanying with the reduced ρ by Fe doping, the *PF* could be further enhanced by a proper co-doping. Accordingly, the *PF* was found to be enhanced in the co-doped samples in Fig. 5.5. The co-doped sample with the lowest ρ, $Ca_{2.9}Y_{0.1}Co_{3.97}Fe_{0.03}O_{9+\delta}$, exhibited the highest *PF* values over the whole measured temperatures. Wang et al. have concluded that in the doping range $x \leq 0.25$, the Y dopant content of $x = 0.1$ greatly deteriorated the *PF* due to the overwhelming increase in ρ [122]. Therefore, the reduction of ρ is believed as the contribution from Fe doping and which is crucial to the *PF* enhancement.

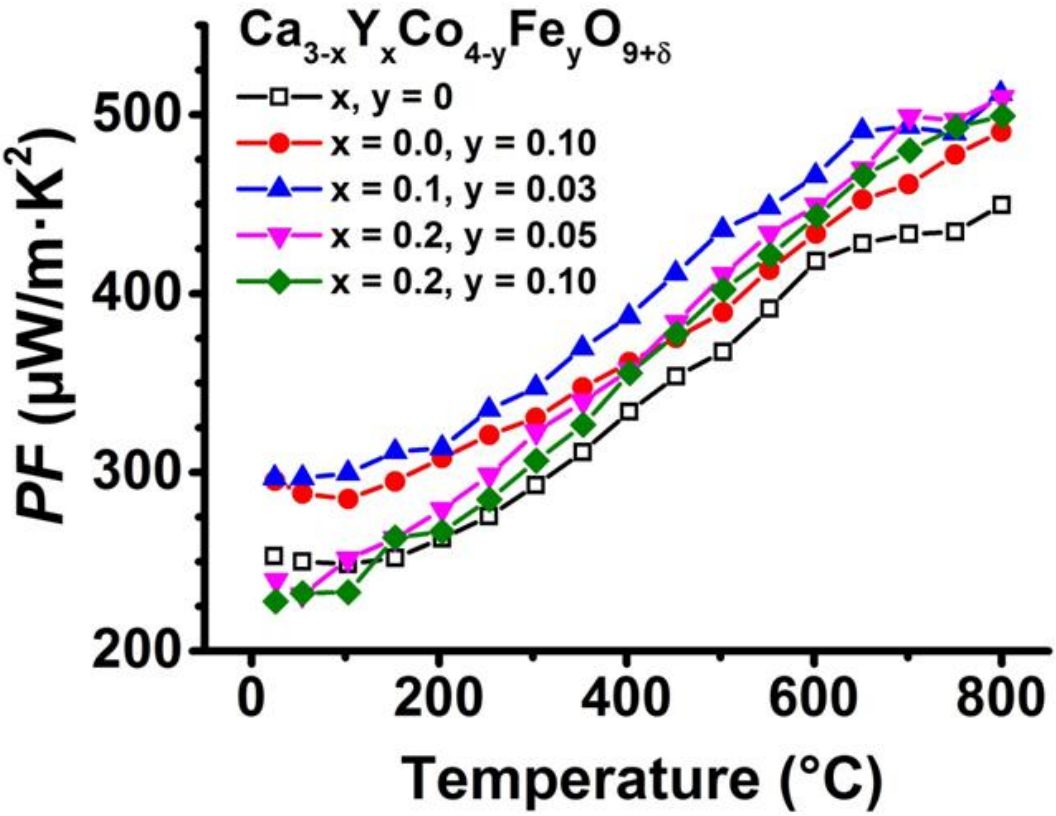

Fig. 5.5. The temperature dependent power factor (*PF*) of typical samples that are representatives of the Fe-doped (x = 0, y = 0.1) and co-doped systems (x = 0.1, y = 0.03; x = 0.2, y = 0.05; x = 0.2, y = 0.1). Open symbols denote the *PF* of the un-doped Co349 as a reference.

Fig. 5.6 shows the thermal conductivity (κ) for the selected $Ca_{3-x}Y_xCo_{4-y}Fe_yO_{9+\delta}$ samples (with the measurement direction as indicated in the figure). Since the total thermal conductivity (κ) contains both the electronic conductivity (κ_e) and the lattice conductivity (κ_L), namely $\kappa = \kappa_e + \kappa_L$. With the Wiedemann–Franz relationship, $\kappa_e = L_0 \cdot T/\rho$, where the Lorenz number is taken to be $L_0 = 2.44\times10^{-8}\ V^2/K^2$, it was found that the lattice contribution accounts for more than 80 % of the total thermal conductivity as observed in other studies [67][153][154]. All the samples for x, y ≤ 0.10 exhibited similar κ values to the un-doped Co349 sample over the whole temperature range. Since the minor mass difference between Fe and Co atoms, Fe substitution was not expected to be an effective phonon scattering site. The decreasing κ for the samples with higher Y dopant content (e.g., x = 0.2 or 0.3) could be attributed to the heavy Y^{3+}substitution for Ca^{2+} leading to a reduction in κ_L, as well as the observed evident microstructure changes in Fig. 5.2.

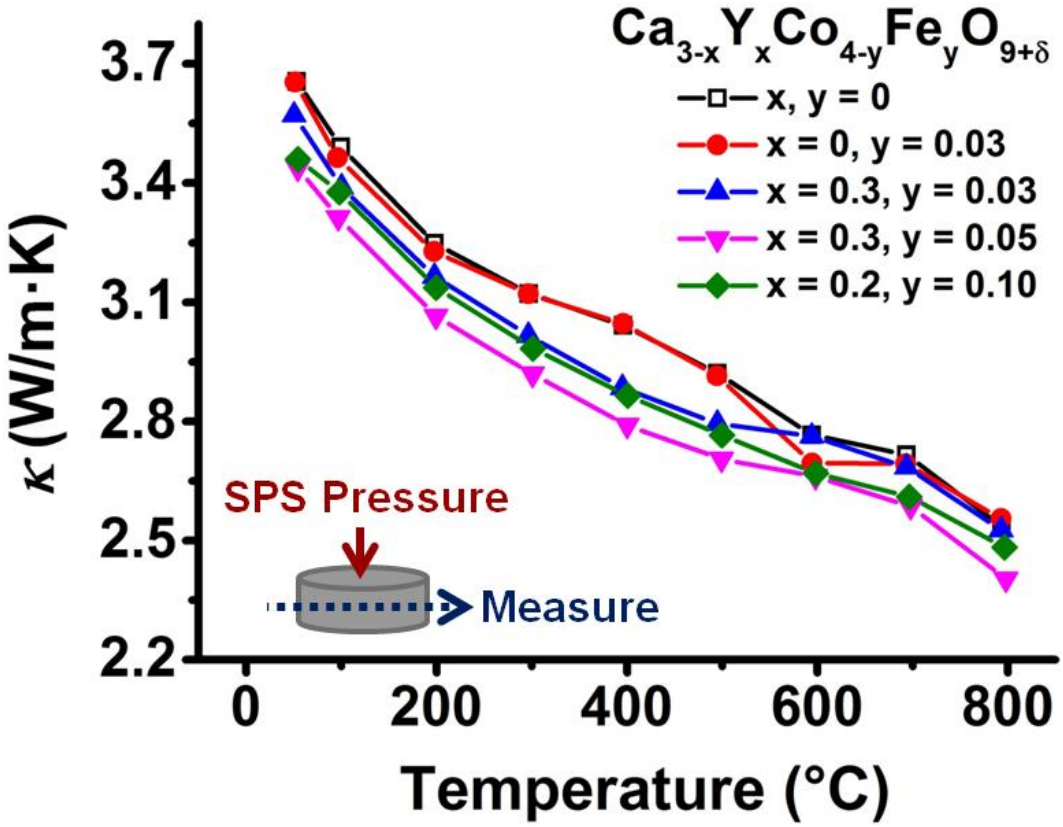

Fig. 5.6. The temperature dependent thermal conductivity (κ) of $Ca_{3-x}Y_xCo_{4-y}Fe_yO_{9+\delta}$ samples which exhibited lower values in the four respective groups described in Fig. 5.3 and 5.4: the Fe-doped Co349 and co-doped samples with y = 0.03 to 0.10. Open symbols denote κ values of the un-doped Co349 as a reference. The measurement was performed along the direction perpendicular to the SPS pressure axis for in-plane κ.

Finally, the *ZT* was calculated for all investigated samples using the in-plane (measured along the direction perpendicular to SPS pressure axis) Seebeck coefficient (*S*), electrical resistivity (ρ) and thermal conductivity (κ). Fig. 5.7 presents the *ZT* as a function of temperature for the un-doped and a typical co-doped $Ca_{2.9}Y_{0.1}Co_{3.97}Fe_{0.03}O_{9+\delta}$ samples, showing an enhancement over the whole studied temperatures. At 800 ℃, the *ZT* value of the $Ca_{2.9}Y_{0.1}Co_{3.97}Fe_{0.03}O_{9+\delta}$ sample was 0.22 and which is about 18 % higher than that of un-doped Co349.

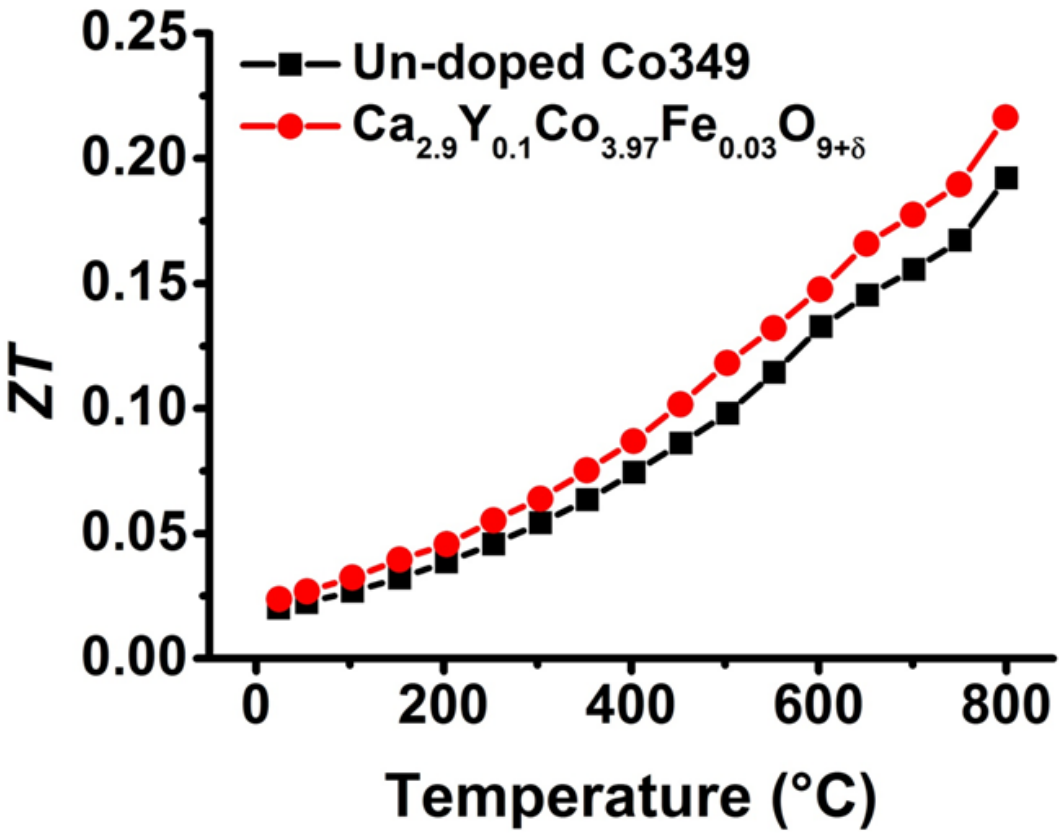

Fig. 5.7. The temperature dependent *ZT* of the un-doped Co349 and $Ca_{2.9}Y_{0.1}Co_{3.97}Fe_{0.03}O_{9+\delta}$.

5.4 Conclusion

The Fe-doped and Fe/Y co-doped $Ca_{3-x}Y_xCo_{4-y}Fe_yO_{9+\delta}$ ($0 \leq x \leq 0.3$, $0 \leq y \leq 0.1$) systems were systematically investigated in terms of Fe and Y doping at the Co- and Ca-sites of Co349, respectively. The Fe substitution at the Co-sites effectively reduces the electrical resistivity (ρ) in the high temperature region, while the Seebeck coefficient (*S*) is influenced only slightly. Y substitution for Ca^{2+} leads to an increase in the Seebeck coefficient but also in the electrical resistivity. With proper additional Fe doping, the rising ρ was compensated, together with the improved *S* leading to an improvement of the *PF*. Among all investigated systems, the co-doping effects of Fe and Y were most effective for the sample with $x = 0.1$ and $y = 0.03$ (i.e., $Ca_{2.9}Y_{0.1}Co_{3.97}Fe_{0.03}O_{9+\delta}$). The maximum power factor reaches a value of 510 $\mu W/m{\cdot}K^2$, which is among the highest value reported so far on the Co349 system at 800 ℃. Although the *ZT* enhancement is only minor due to no significant reduction in the overall κ, the more significant increase in the *PF* owing to the reduction in ρ along with an increase in *S* renders Fe/Y co-doped Co349 a promising candidate for applications where the power output density is more important than the overall conversion efficiency.

Chapter 6

Effects of Ce doping in $Ca_3Co_4O_{9+\delta}$ on High Temperature Thermoelectric Properties

Abstract

A series of $Ca_{3-x}Ce_xCo_4O_{9+\delta}$ ($0 \leq x \leq 0.1$) samples were synthesized by auto-combustion reaction and followed by a spark plasma sintering (SPS) processing. The effects of Ce doping on high temperature (room temperature to 800 ℃) thermoelectric properties are systematically investigated. The electrical resistivity (ρ) and Seebeck coefficient (S) increased with Ce dopant content over the whole measured temperature range, while the in-plane thermal conductivity (κ) was only slightly influenced. Among all investigated samples, Ce doping showed a slight decrease in the power factor (PF) but similar figure-of-merit (ZT) values to the un-doped sample, suggesting the potential for the Seebeck coefficient enhancement in co-doped $Ca_3Co_4O_{9+\delta}$.

6.1 Introduction

Thermoelectric (TE) materials attract much attention as the ability to extract electrical power from thermal energy via the Seebeck effect. To evaluate the performance of TE materials the dimensionless figure-of-merit ZT ($= S^2T/\rho\kappa$) is applied which involves the Seebeck coefficient (S), electrical resistivity (ρ), thermal conductivity (κ) and absolute temperature (T). For TE applications used in high temperature region, oxide materials are one of distinct candidates due to its high-temperature structural and chemical stabilities, in addition, low cost, resource abundant [67][70]. In this category, p-type $Ca_3Co_4O_{9+\delta}$ arouses a great interest after the discovery by Shikano et al. with a ZT of 0.83 (at 800 ℃) for a single crystalline sample as a promising high temperature thermoelectric p-type oxide material [67].

Misfit-layered $Ca_3Co_4O_{9+\delta}$ (abbreviation Co349 used in the following text) consists of a CdI_2-type hexagonal CoO_2 subsystem and a rock salt-type Ca_2CoO_3 subsystem which are alternately stacked along the c-axis with identical a, c and β parameters but differ from incommensurate b parameters. This misfit-layered oxide therefore can be expressed as $[Ca_2CoO_3][CoO_2]_{(b1/b2)}$ with a $b1$ to $b2$ ratio of approximately 1.62, where $b1$ to $b2$ are two lattice parameters for the rock salt and CoO_2 subsystems respectively [63][66]. As a p-type material, the hole charge conduction occurs mainly in the CoO_2 subsystem with the Ca_2CoO_3 layer acting as a charge reservoir, and the misfit between layers is expected to hinder the phonon transport [133][154].

Although a decent ZT value has been shown for the Co349 single crystal at high temperature, the Co349 polycrystalline exhibits much lower ZT value of 0.2 at 800 ℃ [43][44]. To improve the ZT of the polycrystalline Co349, many efforts have been made by either chemical ion substitutions for Ca to adjust the carrier concentration or by fluctuate phonon transportation [69]–[71][122][156][157][165]–[167]. The rare-earth ions (La, Pr, Dy, Ho, Er, Yb and Lu) as substitutions at Ca-site of Co349 system have been reported by Wang et al. and Nong et al. [69]–[71], which showed the capability to enhance the ZT value in high temperature region owing to the simultaneous increase in S and the decrease in the lattice thermal conductivity (κ_L). The similar thermoelectric tendencies, the increase in S and reduced κ, also appeared in the studies of Ce substitution for Ca ion in Co349 at low temperature range (below 350 K) conducted by Tang et al. [166][167]. Ce doping resulted in the enhanced ZT values from about 0.003 for the un-doped Co349 to 0.016 for the sample $Ca_{2.9}Co_4O_{9+\delta}$ at 335 K, suggesting the potential for improving Co349 TE properties; however, the effects of Ce dopant at high temperature range remains unknown.

In order to investigate the effects of Ce doping on high temperature thermoelectric properties, a series of the Ce-doped $Ca_{3-x}Ce_xCo_4O_{9+\delta}$ ($0 \leq x \leq 0.1$) were prepared. The thermoelectric properties were then measured and are presented from room temperature to 800 ℃ and the Ce doping effects in this temperature range are discussed.

6.2 Experimental Procedure

Polycrystalline Ce-doped $Ca_3Co_4O_{9+\delta}$ samples were synthesized by the auto-combustion reaction as the described in Ref. [44]. A stoichiometric ratio of analytical regent grade (99+ %) $Ca(NO_3)_2{\cdot}4H_2O$, $Co(NO_3)_2{\cdot}6H_2O$, $Ce(NO_3)_3{\cdot}6H_2O$ were dissolved in distilled water with a specific amount of citric acid (99+ %) for the citrate–metal cation molar ratio at 1. Additionally, the citrate-to-nitrate molar ratio was tuned by introducing NH_4NO_3 (98+ %) to 0.40. After a uniform viscous gel was obtained, the auto-combustion process was initiated by raising the temperature to about 250 ℃ and which was completed within a minute. The resulting powders were calcined at 750 ℃ for 2 hours to obtain single phase $Ca_3Co_4O_{9+\delta}$ as identified by X-ray diffraction.

The powders were subsequently consolidated by a spark plasma sintering (SPS, Dr. Sinter SPS-515S, Fuji Electronic Industrial Co., Ltd.) to a size of 10 mm-thick pellets. The sintering conditions applied on the doped Co349 were chosen to be 800 ℃ for 5 min with a fixed uniaxial pressure of 50 MPa and a ramping rate of 100 ℃/min based on our previous results [43][44].

X-ray powder diffraction (XRD) patterns were collected at room temperature using a Bruker D8 diffractometer with Cu K_α-radiation to identify the phase of the as-synthesized powders and SPS-sintered pellets. TE properties (in-plane TE properties) presented in this work were collected along the direction perpendicular to the SPS pressure axis [44]. The Seebeck coefficient (S) and electrical resistivity (ρ) measurements, at the same direction, were carried out with an ULVAC-RIKO ZEM3 from room temperature up to 800 ℃ under a low-pressure helium atmosphere. The thermal conductivity was calculated by the equation $\kappa = \rho \cdot \alpha \cdot c_p$ (where ρ, α and c_p are the density, thermal diffusivity and specific heat capacity, respectively). The thermal diffusivity was obtained under vacuum in a NETZSCH LFA-457 laser flash system. The c_p in this work was taken to be the temperature independent Dulong-Petit values. The bulk density was measured with a Micromeritics AccuPyc 1340 gas pycnometer. All samples exhibited densities of more than 99 % of the theoretical densities. The theoretical density 4.68 g/cm^3 for the un-doped Co349 was determined based on the lattice parameters from Masset et al. [63]. TE properties (ρ, S, κ) shown in this work include less than 1 % measurement error and it was taken into consideration in the sequential comparison and discussion.

6.3 Result and Discussion

XRD patterns for the as-synthesized Ce-doped $Ca_{3-x}Ce_xCo_4O_{9+\delta}$ ($0 \leq x \leq 0.1$) samples are shown in Fig. 6.1. For a Ce doping content of $x = 0.10$, the XRD pattern revealed the existence of secondary phase CeO_2, as indexed "♦" according to JCPDS PDF # 01-081-0792 suggesting the maximum Ce doping level in Co349 system. Except for the $x = 0.10$ sample, all peaks were indexed as $Ca_3Co_4O_{9+\delta}$ according to JCPDS PDF # 21-0139 and the XRD pattern reported in the

literature [63]. Fig. 6.2 shows a set of SEM micrographs of fracture surfaces for the un-doped (x = 0) and the doped x = 0.07 samples after the SPS processing. These micrographs were taken along the perpendicular direction of the SPS pressure axis. Fine platelet morphology elongated perpendicular to the SPS pressure axis was found in these two micrographs. It should be noted that no obvious difference in the morphology is evident from these micrographs, as also indicated by the XRD patterns (Fig. 6.1), which show no distinct difference in the intensity of the peaks for these two compositions. All samples prepared as described in the experiments section with the auto-combustion reaction and followed by the SPS processing exhibited high samples densities of more than 99 % theoretical density; these values are in agreement with our previous work [44].

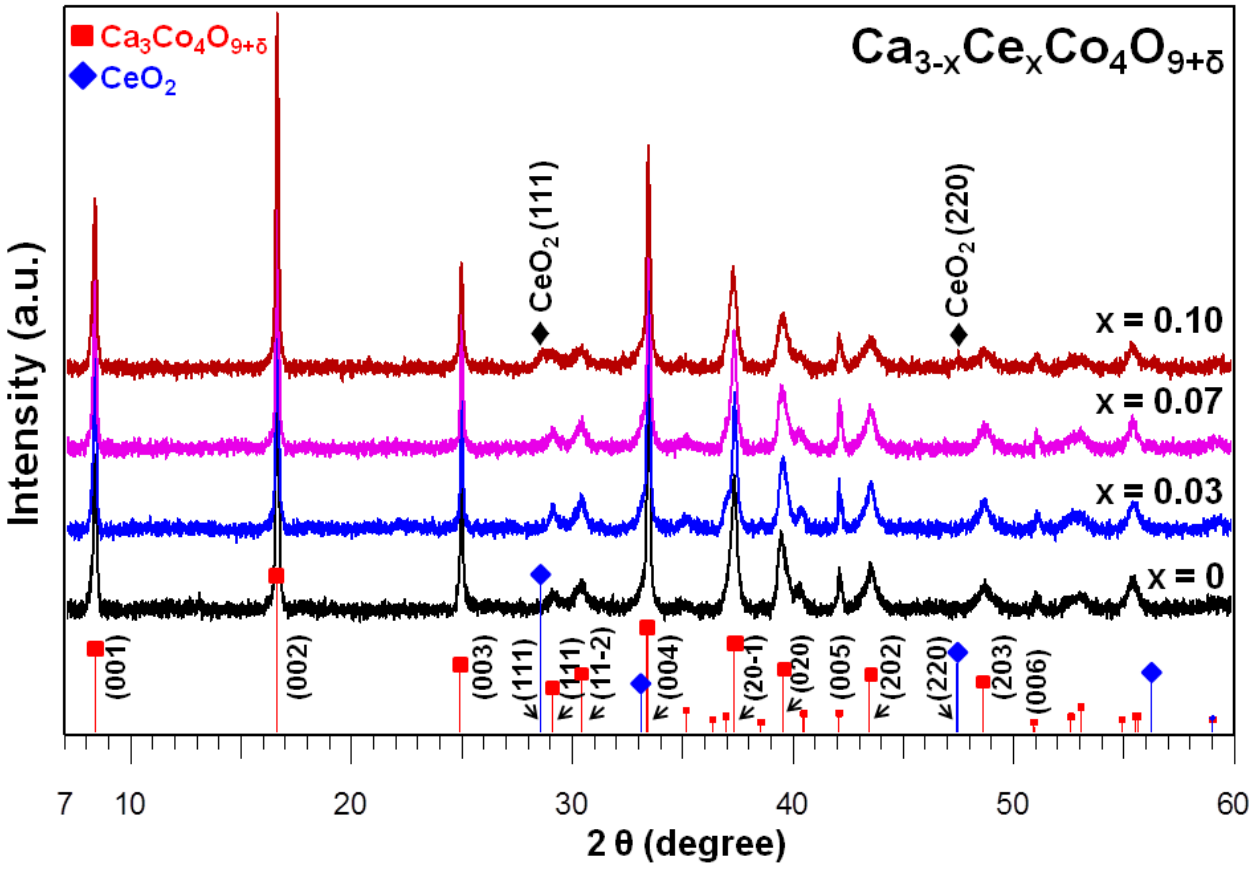

Fig. 6.1. XRD patterns of the as-synthesized Ce-doped $Ca_{3-x}Ce_xCo_4O_{9+\delta}$ ($0 \leq x \leq 0.1$) samples. The red (■) and blue (♦) line patterns with indices at the bottom are from JCPDS PDF # 21-0139 and 01-081-0792 for $Ca_3Co_4O_{9+\delta}$ and CeO_2 phase identification respectively.

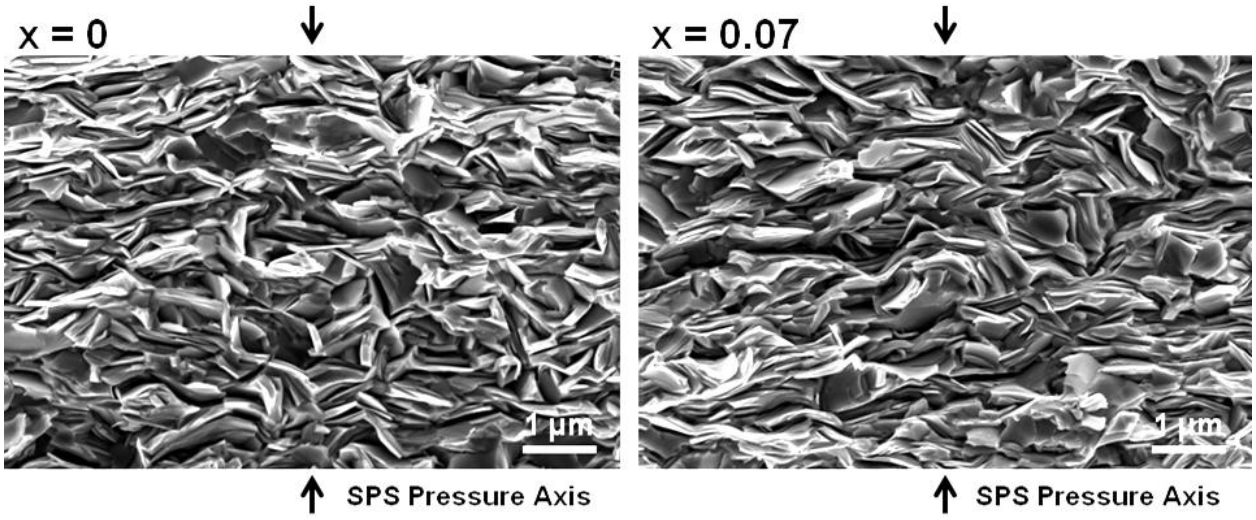

Fig. 6.2. SEM micrographs of fracture surfaces observed along the direction perpendicular to the SPS pressure axis for the SPS-sintered un-doped Co349 (left) and $Ca_{2.93}Ce_{0.07}Co_4O_{9+\delta}$ (right) samples.

Fig. 6.3 shows the electrical resistivity (ρ) as a function of temperature for the Ce-doped $Ca_{3-x}Ce_xCo_4O_{9+\delta}$ ($0 \leq x \leq 0.1$). The un-doped Co349 exhibited the lowest ρ while ρ is found to increase with increasing the Ce dopant content. Ce substitution may exist at Ca-site in Co349 as Ce^{3+} or Ce^{4+}. Owing to the similarity of Ce^{3+} and Ca^{2+} ionic radii (1.01 Å and 1.00 Å in six-coordination respectively) [168], it is plausible that Ce dopant substitutes for Ca^{2+} ion as a trivalent Ce, and consequently results in the decrease in the amount of the hole carrier Co^{4+} for net valence balance. This is consistent with the results of Tang et al. who estimated the valance of the Co by effective magnetic moment measurements at low temperature and found that Ce doping may reduce the Co^{4+} concentration [166]. The increasing ρ induced by Ce doping might be attributed to the decrease in the carrier concentration.

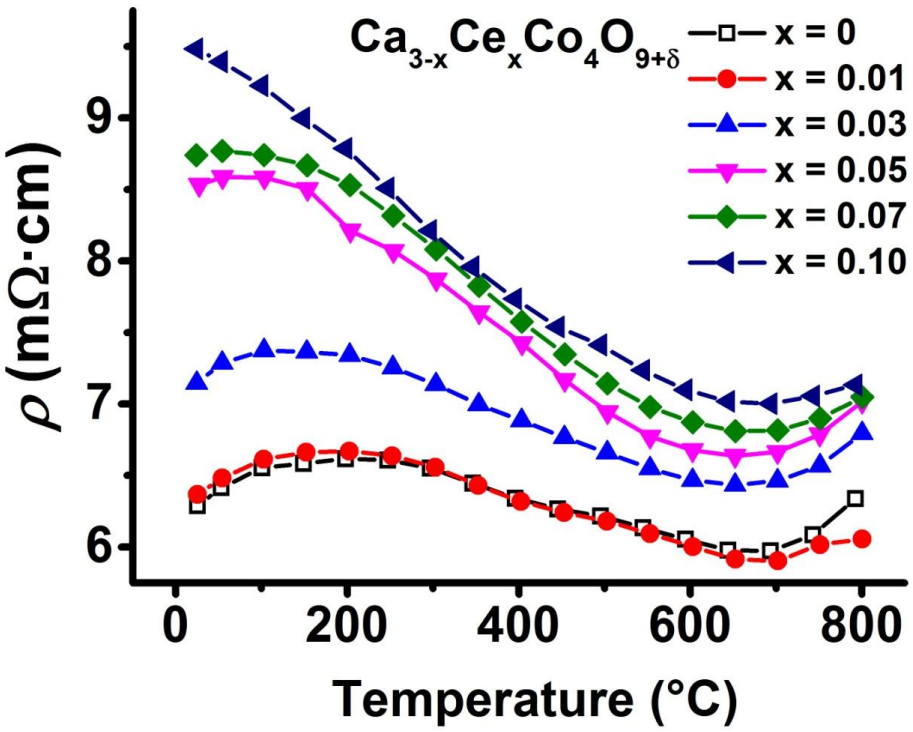

Fig. 6.3. Electrical resistivity (ρ) as a function of temperature for $Ca_{3-x}Ce_xCo_4O_{9+\delta}$ ($0 \leq x \leq 0.1$).

The Seebeck coefficient (S) as a function of temperature for the Ce-doped samples is shown in Fig. 6.4. The monotonic increase in S with Ce doping content is clear. At high temperature region the Seebeck coefficient (S) of Co349 can be expressed as

$$S(T \to \infty) = \frac{k_B}{(-e)} \cdot \ln\left(\frac{g_3}{g_4} \cdot \frac{C}{1-C}\right), \tag{6.1}$$

where C denotes the Co^{4+} concentration and the values of g_3 and g_4 are numbers of configurations including spin and orbit degrees of freedom for Co^{3+} and Co^{4+}, respectively [38]. When the temperature is sufficiently high, the electronic correlation can be neglected, namely $k_BT \gg t$ where t is the transfer integral of an electron between neighboring sites and k_B is Boltzmann constant, S is therefore temperature independent and is only determined by the ratio of g_3/g_4 and the relative Co^{4+} concentration [35][38]. Based on the fact that the average oxidation state of Co ions in CoO_2 subsystem of the un-doped Co349 is +3.5 with $C = 0.5$ [154], in Fig. 6.4 at high temperatures the un-doped Co349 exhibited $S \approx 165$ μV/K which is close to the upper limit $S = 154\ \mu V/K$ derived from Eq. 6.1 for $g_3/g_4 = 1/6$ suggesting that both the Co^{3+} and Co^{4+} ions in CoO_2 subsystem are in low spin state [38]. Upon Ce doping, the increase

in S at high temperatures from 160 to 180 $\mu V/\mathrm{K}$ might be interpreted as a result of the decrease in the carrier concentration which leads to the changed C value in Eq. 6.1 and the increase in the electrical resistivity in Fig. 6.3, and along with the maintained spin states of Co ions, meaning the unchanged g_3/g_4 ratio which is consistent with Tang et al. speculation [167].

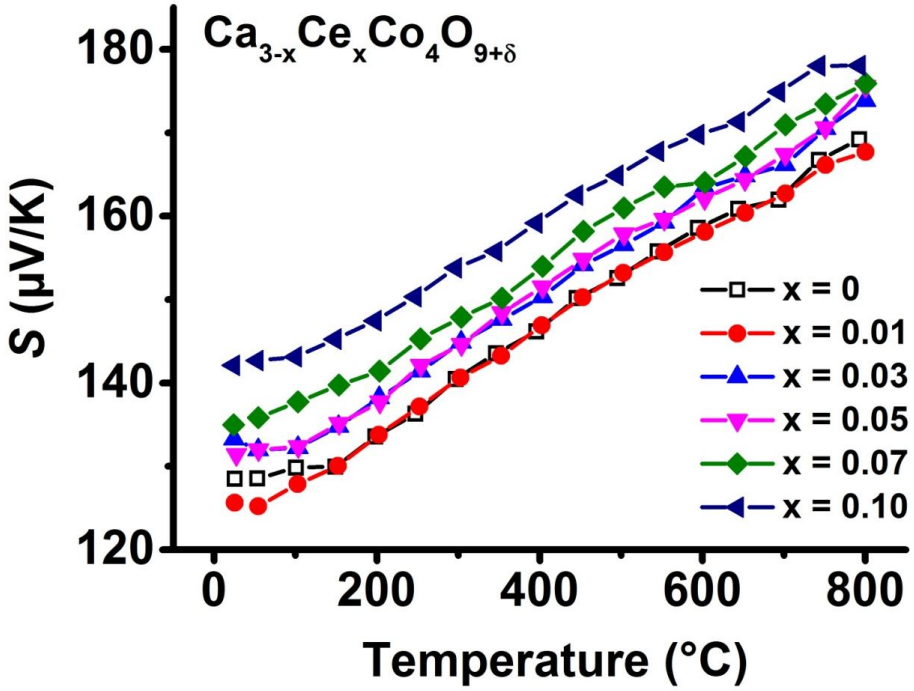

Fig. 6.4. Temperature dependence of the Seebeck coefficient (S) of $Ca_{3-x}Ce_xCo_4O_{9+\delta}$ ($0 \leq x \leq 0.1$).

The power factor (PF) as a function of temperature for the Ce-doped samples was calculated and plotted in Fig. 6.5. As a result of Ce doping which causes the increase in both ρ and S, the power factor of Ce doped samples was compromised throughout the whole temperature range. The PF was mainly influenced by the increase of S. These is no obvious trend for the decrease of the PF with increasing the Ce dopant but it seems that the maximum PF achieved at $x = 0$ and 0.01.

Fig. 6.6 shows the thermal conductivity (κ) for $Ca_{3-x}Ce_xCo_4O_{9+\delta}$ samples (the measurement direction is indicated in the figure). Since the total thermal conductivity (κ) contains both the electronic conductivity (κ_e) and the lattice conductivity (κ_L), namely $\kappa = \kappa_e + \kappa_L$. In Co349 system, more than 80 % of the total thermal conductivity is accounted for by the lattice contribution when applying the Wiedemann–Franz relationship, $\kappa_e = L_0 \cdot T/\rho$ where the Lorenz

factor is taken as $L_0 = 2.44\times10^{-8}\ \mathrm{V^2/K^2}$ for Co349 [67][133]. Except the x = 0.10 sample, the Ce-doped samples in Fig. 6.6 showed slightly lower thermal conductivity values over the entire studied temperature range than the un-doped Co349 sample. The lowest thermal conductivity found in x = 0.05 and 0.07 samples might demonstrate the fluctuated phonon transport by heavier Ce dopants. The sample with x = 0.10 exhibited slightly higher value of κ than the un-doped Co349 sample which is believed to be contributed from the secondary phase CeO_2 [169].

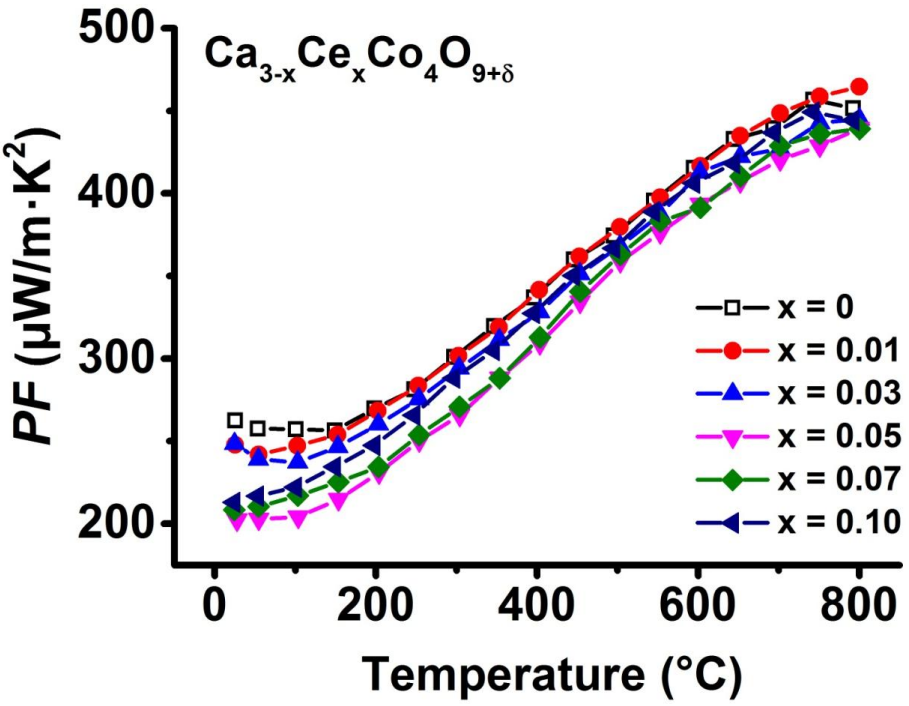

Fig. 6.5. The temperature dependent power factor (*PF*) of $Ca_{3-x}Ce_xCo_4O_{9+\delta}$ ($0 \leq x \leq 0.1$).

ZT values shown in Fig. 6.7 were calculated by the properties along the direction perpendicular to SPS pressure axis. All Ce-doped Co349 samples were found to exhibit similar *ZT* values throughout the whole temperature range regardless of the amount of Ce dopant. The reduction of ρ is probably the critical limiting factor for achieving *ZT* enhancement.

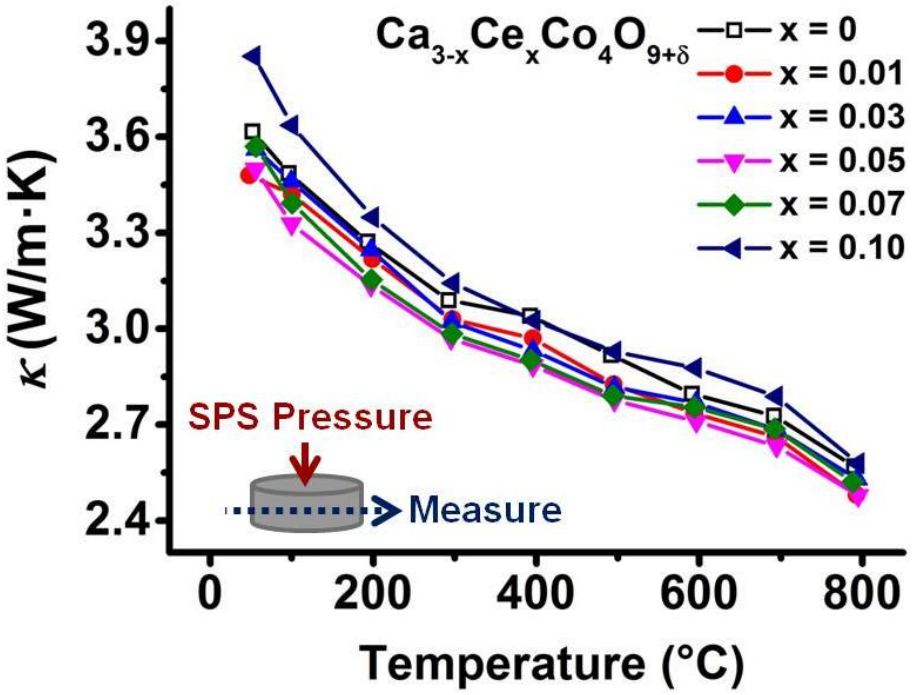

Fig. 6.6. The temperature dependent thermal conductivity (κ) of $Ca_{3-x}Ce_xCo_4O_{9+\delta}$ ($0 \leq x \leq 0.1$). The measurement was performed along the direction perpendicular to the SPS pressure axis to give in-plane κ.

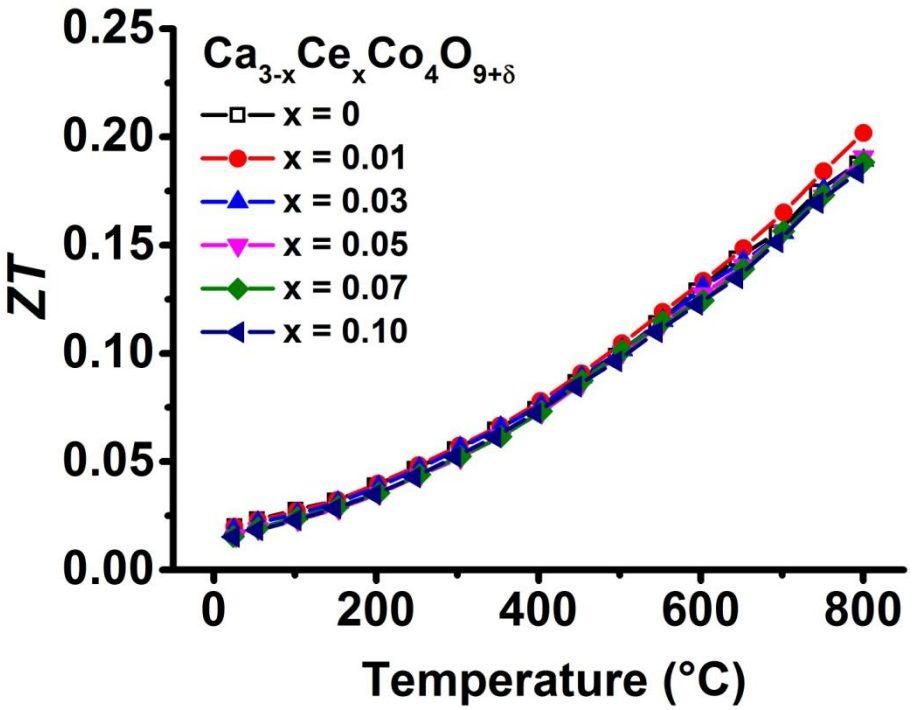

Fig. 6.7. The temperature dependent *ZT* of $Ca_{3-x}Ce_xCo_4O_{9+\delta}$ ($0 \leq x \leq 0.1$).

6.4 Conclusion

The Ce-doped $Ca_{3-x}Ce_xCo_4O_{9+\delta}$ ($0 \leq x \leq 0.1$) system was systematically investigated in the temperature range from room temperature to 800 ℃. The trivalent Ce substitution for Ca^{2+} might result in the decrease of the carrier concentration leading to a simultaneous increase in the electrical resistivity (ρ) and Seebeck coefficient (S), but the slight decrease in the power factor (PF). Similar ZT values for all Ce-doped samples suggest that the reduction of ρ is crucial to the TE performance. Coupling with another dopant to suppress the increased ρ, for instance Fe doping at Co-site in Co349, the potential of Ce dopant on the Seebeck coefficient enhancement can be utilized in a co-doped Co349 system.

Summary

The p-type misfit-layered cobaltate $Ca_3Co_4O_{9+\delta}$ has been investigated and discussed, with the focus on the spark plasma sintering (SPS) processing conditions, synthesis development and the introduction of extrinsic dopants.

The research began with the study of the effects of varying the SPS processing conditions and syntheses. The applied pressure, sintering temperature and ramping rate were varied systematically to approach optimized SPS conditions for consolidation of $Ca_3Co_4O_{9+\delta}$ powders synthesized by solid-state reaction with characterizations of the thermoelectric transport properties, density, and degree of texturing. The bulk density was found to be the key parameter for reducing the electrical resistivity (ρ) and thus maximizing the power factor, achieving 400 $\mu W/m{\cdot}K^2$ at 800 ℃. However, the figure-of-merit (*ZT*) was independent of the solid-state reaction preparations.

The $Ca_3Co_4O_{9+\delta}$ powder synthesized by citrate–nitrate sol–gel reaction and densified by the concluded optimal SPS parameters for the solid-state reaction-synthesized powder was likewise evaluated for comparison. The pellet sintered at 850 ℃ with an applied pressure of 50 MPa preserved the smaller particle size during SPS as well as exhibited a visible degree of texturing. Measurements of the thermoelectric properties revealed an enhancement in the electrical conductivity and the power factor (*PF*) which reached 465 $\mu W/m{\cdot}K^2$ at 800 ℃. This can be attributed to the better grain alignment caused by the smaller particle sizes. Therefore, sol–gel reaction is suggested to be a preferable synthesis for high-performance thermoelectric $Ca_3Co_4O_{9+\delta}$.

A new developed rapid synthesis method of producing $Ca_3Co_4O_{9+\delta}$ fine powders using an auto-combustion synthesis was demonstrated. The auto-combustion process was initiated by a carefully controlled thermal oxidation–reduction reaction. The features of a wet chemical synthesis, such as morphological and compositional homogeneity, and fine, well-defined particle sizes are inherited. With the optimized SPS processing conditions and careful characterizations for anisotropic thermoelectric properties, the auto-combustion synthesis for pure polycrystalline $Ca_3Co_4O_{9+\delta}$ exhibited a high power factor and *ZT* in the plane perpendicular to the SPS pressure axis of about 500 $\mu W/m{\cdot}K^2$ and 0.21 at 800 ℃, respectively. Furthermore, the auto-combustion synthesis is able to be applied to doped $Ca_3Co_4O_{9+\delta}$ for further thermoelectric performance improvement.

Fe-doped and Fe/Y co-doped $Ca_{3-x}Y_xCo_{4-y}Fe_yO_{9+\delta}$ ($0 \leq x \leq 0.3,\ 0 \leq y \leq 0.1$) samples synthesized by the newly developed auto-combustion reaction followed by SPS processing with the effects of Fe and Y doping on the high temperature thermoelectric properties were systematically investigated. In the high temperature region, Fe doping effectively reduces the

electrical resistivity while only slightly influencing on the Seebeck coefficient (*S*). Y doping leads to an increase in the Seebeck coefficient but also in the electrical resistivity. With proper additional Fe doping, the co-doped system is able to compensate the rising the electrical resistivity, leading to an improvement of the power factor along with the improved Seebeck coefficient. The co-doping effects of Fe and Y were most effective for the sample with $x = 0.1$ and $y = 0.03$ (i.e., $Ca_{2.9}Y_{0.1}Co_{3.97}Fe_{0.03}O_{9+\delta}$). The maximum power factor reaches a value of 510 $\mu W/m{\cdot}K^2$, which is among the highest value reported so far for polycrystalline $Ca_3Co_4O_{9+\delta}$ at 800 ℃. The *ZT* enhancement is only minor due to no significant reduction in the total thermal conductivity (κ); however, the more significant increase in the power factor as the reduced electrical resistivity along with the increased Seebeck coefficient renders Fe/Y co-doped $Ca_3Co_4O_{9+\delta}$ a promising candidate for applications where the power output density is more important than the overall conversion efficiency.

The investigation of rare-earth element Ce doping in $Ca_3Co_4O_{9+\delta}$ aimed to explore the effects on high temperature thermoelectric properties. With the auto-combustion reaction synthesis and a SPS processing, Ce-doped $Ca_3Co_4O_{9+\delta}$ exhibited the increased electrical resistivity and Seebeck coefficient with increasing Ce doping content over the whole measured temperature range, while the in-plane thermal conductivity (κ) was only slightly influenced. Since the introduction of Ce leads to a small decrease in the power factor but also reduction in the thermal conductivity resulting in the *ZT* values being similar to the un-doped $Ca_3Co_4O_{9+\delta}$, the *ZT* may be enhanced in rare-earth and transition metal (e.g., Ce and Fe) co-doped $Ca_3Co_4O_{9+\delta}$ through decoupling of the otherwise interdependent electronic and thermal transport properties.

Bibliography

[1] V. V. Tyagi, N. A. A. Rahim, N. A. Rahim, and J. A. L. Selvaraj, "Progress in solar PV technology: Research and achievement," *Renew. Sustain. Energy Rev.*, vol. 20, pp. 443–461, 2013.

[2] B. K. Ndimba, R. J. Ndimba, T. S. Johnson, R. Waditee-Sirisattha, M. Baba, S. Sirisattha, Y. Shiraiwa, G. K. Agrawal, and R. Rakwal, "Biofuels as a sustainable energy source: an update of the applications of proteomics in bioenergy crops and algae," *J. Proteomics*, vol. 93, pp. 234–44, Nov. 2013.

[3] D. Y. C. Leung and Y. Yang, "Wind energy development and its environmental impact: A review," *Renewable and Sustainable Energy Reviews*, vol. 16. pp. 1031–1039, 2012.

[4] S. Chu and A. Majumdar, "Opportunities and challenges for a sustainable energy future," *Nature*, vol. 488. pp. 294–303, 2012.

[5] M. Zebarjadi, K. Esfarjani, M. S. Dresselhaus, Z. F. Ren, and G. Chen, "Perspectives on thermoelectrics: from fundamentals to device applications," *Energy Environ. Sci.*, vol. 5, no. 1, p. 5147, 2012.

[6] S. B. Riffat and X. Ma, "Thermoelectrics: A review of present and potential applications," *Applied Thermal Engineering*, vol. 23. pp. 913–935, 2003.

[7] K. Saqr and M. Musa, "Critical review of thermoelectrics in modern power generation applications," *Therm. Sci.*, vol. 13, no. 3, pp. 165–174, 2009.

[8] G. H. Rinehart, "Design characteristics and fabrication of radioisotope heat sources for space missions," *Prog. Nucl. Energy*, vol. 39, no. 3–4, pp. 305–319, Jan. 2001.

[9] G. L. Bennett, "Mission interplanetary: Using radioisotope power to explore the solar system," *Energy Convers. Manag.*, vol. 49, no. 3, pp. 382–392, Mar. 2008.

[10] M. S. El-Genk, H. H. Saber, and T. Caillat, "Efficient segmented thermoelectric unicouples for space power applications," *Energy Convers. Manag.*, vol. 44, no. 11, pp. 1755–1772, Jul. 2003.

[11] D. M. Rowe, "Applications of nuclear-powered thermoelectric generators in space," *Applied Energy*, vol. 40. pp. 241–271, 1991.

[12] A. Bianchini, M. Pellegrini, and C. Saccani, "Thermoelectric Cells Cogeneration from Biomass Power Plant," *Energy Procedia*, vol. 45, pp. 268–277, 2014.

[13] S. Kumar, S. D. Heister, X. Xu, J. R. Salvador, and G. P. Meisner, "Thermoelectric Generators for Automotive Waste Heat Recovery Systems Part II: Parametric Evaluation and Topological Studies," *J. Electron. Mater.*, vol. 42, pp. 944–955, 2013.

[14] J. Yang and F. R. Stabler, "Automotive Applications of Thermoelectric Materials," *J. Electron. Mater.*, vol. 38, no. 7, pp. 1245–1251, Feb. 2009.

[15] T. Kyono, R. O. Suzuki, and K. Ono, "Conversion of unused heat energy to electricity by means of thermoelectric generation in condenser," *IEEE Trans. Energy Convers.*, vol. 18, no. 2, pp. 330–334, Jun. 2003.

[16] F. J. DiSalvo, "Thermoelectric Cooling and Power Generation," *Science*, vol. 285. pp. 703–706, 1999.

[17] D. Nemir and J. Beck, "On the Significance of the Thermoelectric Figure of Merit Z," *J. Electron. Mater.*, vol. 39, no. 9, pp. 1897–1901, Jan. 2010.

[18] G. Sebald, D. Guyomar, and A. Agbossou, "On thermoelectric and pyroelectric energy harvesting," *Smart Materials and Structures*, vol. 18. p. 125006, 2009.

[19] T. J. Seebeck, "Ueber die magnetische Polarisation der Metalle und Erze durch Temperatur-Differenz," *Ann. Phys.*, vol. 82, no. 2, pp. 133–160, 1826.

[20] J. Martin, T. Tritt, and C. Uher, "High temperature Seebeck coefficient metrology," *Journal of Applied Physics*, vol. 108. 2010.

[21] J. C. A. Peltier, "Nouvelles expériences sur la caloricité des courants électrique," *Ann. Chim. Phys.*, vol. 56, pp. 371–386, 1834.

[22] W. Thomson, "On a mechanical theory of thermo-electric currents," *Proc. R. Soc. Edinburgh*, pp. 91–98, 1851.

[23] W. Thomson, "Account of Researches in Thermo-Electricity," *Proc. R. Soc. London*, pp. 49–58, 1854.

[24] G. J. Snyder and E. S. Toberer, "Complex thermoelectric materials," *Nat. Mater.*, vol. 7, pp. 105–114, 2008.

[25] E. Altenkirch, "Über den Nutzeffekt der Thermosäulen," *Phys. Zeitschrift*, vol. 10, pp. 560–580, 1909.

[26] E. Altenkirch, "Elektrothermische Kälteerzeugung und reversible elektrische Heizung," *Phys. Zeitschrift*, vol. 12, pp. 920–924, 1911.

[27] G. Snyder and T. Ursell, "Thermoelectric Efficiency and Compatibility," *Phys. Rev. Lett.*, vol. 91, no. 14, p. 148301, Oct. 2003.

[28] P. Drude, “Zur Elektronentheorie der Metalle,” *Ann. Phys.*, vol. 306, no. 3, pp. 566–613, 1900.

[29] P. Drude, “Zur Elektronentheorie der Metalle; II. Teil. Galvanomagnetische und thermomagnetische Effecte,” *Ann. Phys.*, vol. 308, no. 11, pp. 369–402, 1900.

[30] S. M. Sze and M.-K. Lee, *Semiconductor Devices: Physics and Technology*. Wiley, 2013.

[31] S. Kara, Ed., *Electromotive Force and Measurement in Several Systems*. InTech, 2011.

[32] M. Cutler and N. Mott, “Observation of Anderson Localization in an Electron Gas,” *Phys. Rev.*, vol. 181, no. 3, pp. 1336–1340, May 1969.

[33] J. M. Ziman, *Principles of the Theory of Solids*. Cambridge University Press, 1972.

[34] A. Altland and B. Simons, *Condensed Matter Field Theory*. Cambridge University Press, 2006.

[35] P. Chaikin and G. Beni, “Thermopower in the correlated hopping regime,” *Phys. Rev. B*, vol. 13, no. 2, pp. 647–651, Jan. 1976.

[36] A. Oguri and S. Maekawa, “Electrical resistivity, thermal conductivity, and thermopower in the U=∞ Hubbard model,” *Phys. Rev. B*, vol. 41, no. 10, pp. 6977–6988, Apr. 1990.

[37] G. Pálsson and G. Kotliar, “Thermoelectric Response Near the Density Driven Mott Transition,” *Phys. Rev. Lett.*, vol. 80, no. 21, pp. 4775–4778, May 1998.

[38] W. Koshibae, K. Tsutsui, and S. Maekawa, “Thermopower in cobalt oxides,” *Phys. Rev. B*, vol. 62, no. 11, pp. 6869–6872, Sep. 2000.

[39] R. F. Klie, Q. Qiao, T. Paulauskas, A. Gulec, A. Rebola, S. Öğüt, M. P. Prange, J. C. Idrobo, S. T. Pantelides, S. Kolesnik, B. Dabrowski, M. Ozdemir, C. Boyraz, D. Mazumdar, and A. Gupta, “Observations of Co^{4+} in a Higher Spin State and the Increase in the Seebeck Coefficient of Thermoelectric Ca_{3}Co_{4}O_{9},” *Phys. Rev. Lett.*, vol. 108, no. 19, p. 196601, May 2012.

[40] R. Kubo, M. Yokota, and S. Nakajima, “Statistical-Mechanical Theory of Irreversible Processes. II. Response to Thermal Disturbance,” *Journal of the Physical Society of Japan*, vol. 12. pp. 1203–1211, 1957.

[41] I. G. Austin and N. F. Mott, “Polarons in crystalline and non-crystalline materials,” *Advances in Physics*, vol. 18. pp. 41–102, 1969.

[42] K. Sano and Y. Ōno, “Ferromagnetism and Superconductivity in the Multi-orbital Hubbard Model: Hund’s Rule Coupling versus Crystal-Field Splitting,” *J. Phys. Soc. Japan*, vol. 72, no. 8, pp. 1847–1850, Aug. 2003.

[43] N. Wu, T. C. Holgate, N. V. Nong, N. Pryds, and S. Linderoth, "Effects of Synthesis and Spark Plasma Sintering Conditions on the Thermoelectric Properties of $Ca_3Co_4O_{9+\delta}$," *J. Electron. Mater.*, vol. 42, no. 7, pp. 2134–2142, Apr. 2013.

[44] N. Wu, T. C. Holgate, N. V. Nong, N. Pryds, and S. Linderoth, "High temperature thermoelectric properties of $Ca_3Co_4O_{9+\delta}$ by auto-combustion synthesis and spark plasma sintering," *J. Eur. Ceram. Soc.*, vol. 34, no. 4, pp. 925–931, Apr. 2014.

[45] A. Bulusu and D. G. Walker, "Review of electronic transport models for thermoelectric materials," *Superlattices and Microstructures*, vol. 44. pp. 1–36, 2008.

[46] G. S. Nolas, D. T. Morelli, and T. M. Tritt, "SKUTTERUDITES: A Phonon-Glass-Electron Crystal Approach to Advanced Thermoelectric Energy Conversion Applications," *Annu. Rev. Mater. Sci.*, vol. 29, no. 1, pp. 89–116, Aug. 1999.

[47] J. P. Doumerc, M. Blangero, M. Pollet, D. Carlier, J. Darriet, R. Berthelot, C. Delmas, and R. Decourt, "Transition-metal oxides for thermoelectric generation," in *Journal of Electronic Materials*, 2009, vol. 38, pp. 1078–1082.

[48] A. P. Gonçalves, E. B. Lopes, G. Delaizir, J. B. Vaney, B. Lenoir, A. Piarristeguy, A. Pradel, J. Monnier, P. Ochin, and C. Godart, "Semiconducting glasses: A new class of thermoelectric materials?," *J. Solid State Chem.*, vol. 193, pp. 26–30, Sep. 2012.

[49] B. C. Sales, D. Mandrus, and R. K. Williams, "Filled Skutterudite Antimonides: A New Class of Thermoelectric Materials," *Science*, vol. 272. pp. 1325–1328, 1996.

[50] X. Shi, J. Yang, J. R. Salvador, M. Chi, J. Y. Cho, H. Wang, S. Bai, J. Yang, W. Zhang, and L. Chen, "Multiple-filled skutterudites: high thermoelectric figure of merit through separately optimizing electrical and thermal transports," *J. Am. Chem. Soc.*, vol. 133, no. 20, pp. 7837–46, May 2011.

[51] C. Fu, H. Xie, Y. Liu, T. J. Zhu, J. Xie, and X. B. Zhao, "Thermoelectric properties of FeVSb half-Heusler compounds by levitation melting and spark plasma sintering," *Intermetallics*, vol. 32, pp. 39–43, Jan. 2013.

[52] G. S. Nolas, J. L. Cohn, G. A. Slack, and S. B. Schujman, "Semiconducting Ge clathrates: Promising candidates for thermoelectric applications," *Appl. Phys. Lett.*, vol. 73, pp. 178–180, 1998.

[53] X. Yan, M. X. Chen, S. Laumann, E. Bauer, P. Rogl, R. Podloucky, and S. Paschen, "Thermoelectric properties of Ba-Cu-Si clathrates," *Phys. Rev. B - Condens. Matter Mater. Phys.*, vol. 85, 2012.

[54] B. Poudel, Q. Hao, Y. Ma, Y. Lan, A. Minnich, B. Yu, X. Yan, D. Wang, A. Muto, D. Vashaee, X. Chen, J. Liu, M. S. Dresselhaus, G. Chen, and Z. Ren, "High-thermoelectric

performance of nanostructured bismuth antimony telluride bulk alloys," *Science*, vol. 320, pp. 634–638, 2008.

[55] J. P. Heremans, V. Jovovic, E. S. Toberer, A. Saramat, K. Kurosaki, A. Charoenphakdee, S. Yamanaka, and G. J. Snyder, "Enhancement of thermoelectric efficiency in PbTe by distortion of the electronic density of states," *Science*, vol. 321, pp. 554–557, 2008.

[56] L.-D. Zhao, S.-H. Lo, Y. Zhang, H. Sun, G. Tan, C. Uher, C. Wolverton, V. P. Dravid, and M. G. Kanatzidis, "Ultralow thermal conductivity and high thermoelectric figure of merit in SnSe crystals," *Nature*, vol. 508, pp. 373–7, 2014.

[57] R. Venkatasubramanian, E. Siivola, T. Colpitts, and B. O'Quinn, "Thin-film thermoelectric devices with high room-temperature figures of merit," *Nature*, vol. 413, pp. 597–602, 2001.

[58] K. F. Hsu, S. Loo, F. Guo, W. Chen, J. S. Dyck, C. Uher, T. Hogan, E. K. Polychroniadis, and M. G. Kanatzidis, "Cubic $AgPb_mSbTe_{2+m}$: bulk thermoelectric materials with high figure of merit," *Science*, vol. 303, pp. 818–821, 2004.

[59] M. S. Dresselhaus, G. Chen, M. Y. Tang, R. Yang, H. Lee, D. Wang, Z. Ren, J. P. Fleurial, and P. Gogna, "New directions for low-dimensional thermoelectric materials," *Adv. Mater.*, vol. 19, pp. 1043–1053, 2007.

[60] W. Xie, A. Weidenkaff, X. Tang, Q. Zhang, J. Poon, and T. Tritt, "Recent Advances in Nanostructured Thermoelectric Half-Heusler Compounds," *Nanomaterials*, vol. 2, no. 4, pp. 379–412, Nov. 2012.

[61] K. Biswas, J. He, I. D. Blum, C.-I. Wu, T. P. Hogan, D. N. Seidman, V. P. Dravid, and M. G. Kanatzidis, "High-performance bulk thermoelectrics with all-scale hierarchical architectures," *Nature*, vol. 489, no. 7416, pp. 414–8, Sep. 2012.

[62] I. Terasaki, Y. Sasago, and K. Uchinokura, "Large thermoelectric power in $NaCo_2O_4$ single crystals," *Physical Review B*, vol. 56. pp. R12685–R12687, 1997.

[63] A. Masset, C. Michel, A. Maignan, M. Hervieu, O. Toulemonde, F. Studer, B. Raveau, and J. Hejtmanek, "Misfit-layered cobaltite with an anisotropic giant magnetoresistance: $Ca_3Co_4O_9$," *Phys. Rev. B*, vol. 62, no. 1, pp. 166–175, Jul. 2000.

[64] H. Ohta, K. Sugiura, and K. Koumoto, "Recent progress in oxide thermoelectric materials: p-type $Ca_3Co_4O_{9+\delta}$ and n-type $SrTiO3^{-}$," *Inorg. Chem.*, vol. 47, no. 19, pp. 8429–36, Oct. 2008.

[65] M. Schrade, H. Fjeld, T. G. Finstad, and T. Norby, "Electronic Transport Properties of $[Ca_2CoO_{3-\delta}]_q[CoO_2]$," *J. Phys. Chem. C*, vol. 118, no. 6, pp. 2908–2918, Feb. 2014.

[66] Y. Miyazaki, M. Onoda, T. Oku, M. Kikuchi, Y. Ishii, Y. Ono, Y. Morii, and T. Kajitani, "Modulated Structure of the Thermoelectric Compound $[Ca_2CoO_3]_{0.62}CoO_2$," *J. Phys. Soc. Japan*, vol. 71, no. 2, pp. 491–497, Feb. 2002.

[67] M. Shikano and R. Funahashi, "Electrical and thermal properties of single-crystalline $(Ca_2CoO_3)_{0.7}CoO_2$ with a $Ca_3Co_4O_9$ structure," *Appl. Phys. Lett.*, vol. 82, no. 12, p. 1851, 2003.

[68] D. Kenfaui, G. Bonnefont, D. Chateigner, G. Fantozzi, M. Gomina, and J. G. Noudem, "$Ca_3Co_4O_9$ ceramics consolidated by SPS process: Optimisation of mechanical and thermoelectric properties," *Mater. Res. Bull.*, vol. 45, no. 9, pp. 1240–1249, Sep. 2010.

[69] N. V. Nong, C.-J. Liu, and M. Ohtaki, "High-temperature thermoelectric properties of late rare earth-doped $Ca_3Co_4O_{9+\delta}$," *J. Alloys Compd.*, vol. 509, no. 3, pp. 977–981, Jan. 2011.

[70] N. V. Nong, N. Pryds, S. Linderoth, and M. Ohtaki, "Enhancement of the thermoelectric performance of p-type layered oxide $Ca_3Co_4O_{9+\delta}$ through heavy doping and metallic nanoinclusions," *Adv. Mater.*, vol. 23, no. 21, pp. 2484–90, Jun. 2011.

[71] Y. Wang, Y. Sui, F. Li, L. Xu, X. Wang, W. Su, and X. Liu, "Thermoelectrics in misfit-layered oxides $[(Ca,Ln)_2CoO_3]_{0.62}[CoO_2]$: From bulk to nano," *Nano Energy*, vol. 1, no. 3, pp. 456–465, May 2012.

[72] P. Liu, G. Chen, Y. Cui, H. Zhang, F. Xiao, L. Wang, and H. Nakano, "High temperature electrical conductivity and thermoelectric power of Na_xCoO_2," *Solid State Ionics*, vol. 179, no. 39, pp. 2308–2312, Dec. 2008.

[73] P. H. Tsai, T. Norby, T. T. Tan, R. Donelson, Z. D. Chen, and S. Li, "Correlation of oxygen vacancy concentration and thermoelectric properties in $Na_{0.73}CoO_{2-\delta}$," *Appl. Phys. Lett.*, vol. 96, no. 14, p. 141905, 2010.

[74] L. Wang, M. Wang, and D. Zhao, "Thermoelectric properties of c-axis oriented Ni-substituted $NaCoO_2$ thermoelectric oxide by the citric acid complex method," *J. Alloys Compd.*, vol. 471, no. 1–2, pp. 519–523, Mar. 2009.

[75] P. H. Tsai, T. S. Zhang, R. Donelson, T. T. Tan, and S. Li, "Power factor enhancement in Zn-doped $Na_{0.8}CoO_2$," *J. Alloys Compd.*, vol. 509, pp. 5183–5186, 2011.

[76] M. Ito and D. Furumoto, "Microstructure and thermoelectric properties of $Na_xCo_2O_4$/Ag composite synthesized by the polymerized complex method," *J. Alloys Compd.*, vol. 450, no. 1–2, pp. 517–520, Feb. 2008.

[77] D. Chen, H. Chen, A. Maljuk, A. Kulakov, H. Zhang, P. Lemmens, and C. Lin, "Single-crystal growth and investigation of Na_xCoO_2 and $Na_xCoO_2 \cdot yH_2O$," *Phys. Rev. B*, vol. 70, no. 2, p. 024506, Jul. 2004.

[78] D. Xiao, W. Zhu, Y. Ran, N. Nagaosa, and S. Okamoto, "Interface engineering of quantum Hall effects in digital transition metal oxide heterostructures," *Nature Communications*, vol. 2. p. 596, 2011.

[79] S. Ohta, T. Nomura, H. Ohta, and K. Koumoto, "High-temperature carrier transport and thermoelectric properties of heavily La- or Nb-doped $SrTiO_3$ single crystals," *J. Appl. Phys.*, vol. 97, p. 034106, 2005.

[80] L. Zhang, T. Tosho, N. Okinaka, and T. Akiyama, "Thermoelectric Properties of Combustion-Synthesized Lanthanum-Doped Strontium Titanate," *Mater. Trans.*, vol. 48, no. 5, pp. 1079–1083, 2007.

[81] H. Muta, K. Kurosaki, and S. Yamanaka, "Thermoelectric properties of rare earth doped SrTiO3," *J. Alloys Compd.*, vol. 350, pp. 292–295, 2003.

[82] J. Liu, C. L. Wang, H. Peng, W. B. Su, H. C. Wang, J. C. Li, J. L. Zhang, and L. M. Mei, "Thermoelectric Properties of Dy-Doped $SrTiO_3$ Ceramics," *J. Electron. Mater.*, vol. 41, no. 11, pp. 3073–3076, Aug. 2012.

[83] H. C. Wang, C. L. Wang, W. Bin Su, J. Liu, Y. Sun, H. Peng, and L. M. Mei, "Doping effect of la and Dy on the thermoelectric properties of $SrTiO_3$," *J. Am. Ceram. Soc.*, vol. 94, pp. 838–842, 2011.

[84] Y. Wang, K. H. Lee, H. Ohta, and K. Koumoto, "Thermoelectric properties of electron doped $SrO(SrTiO_3)_n$ (n = 1, 2) ceramics," *J. Appl. Phys.*, vol. 105, no. 10, p. 103701, May 2009.

[85] K. Koumoto, Y. Wang, R. Zhang, A. Kosuga, and R. Funahashi, "Oxide Thermoelectric Materials: A Nanostructuring Approach," *Annual Review of Materials Research*, vol. 40. pp. 363–394, 2010.

[86] K. H. Lee, S. W. Kim, H. Ohta, and K. Koumoto, "Ruddlesden-Popper phases as thermoelectric oxides: Nb-doped $SrO(SrTiO_3)_n$ (n = 1, 2)," *J. Appl. Phys.*, vol. 100, no. 6, p. 063717, Sep. 2006.

[87] Y. Wang, K. H. Lee, H. Hyuga, H. Kita, H. Ohta, and K. Koumoto, "Enhancement of thermoelectric performance in rare earth-doped $Sr_3Ti_2O_7$ by symmetry restoration of TiO_6 octahedra," *J. Electroceramics*, vol. 24, no. 2, pp. 76–82, Mar. 2008.

[88] Y. F. Wang, K. H. Lee, H. Ohta, and K. Koumoto, "Fabrication and thermoelectric properties of heavily rare-earth metal-doped $SrO(SrTiO_3)_n$ (n = 1, 2) ceramics," *Ceram. Int.*, vol. 34, no. 4, pp. 849–852, May 2008.

[89] Y. Wang, Y. Sui, and W. Su, "High temperature thermoelectric characteristics of $Ca_{0.9}R_{0.1}MnO_3$ (R = La, Pr, … , Yb)," *J. Appl. Phys.*, vol. 104, no. 9, p. 093703, Nov. 2008.

[90] Y. Wang, Y. Sui, X. Wang, and W. Su, "Enhancement of thermoelectric efficiency in (Ca,Dy)MnO_3–(Ca,Yb)MnO_3 solid solutions," *Appl. Phys. Lett.*, vol. 97, no. 5, p. 052109, Aug. 2010.

[91] X. Meng, S. Hao, J. Li, Q. Fu, and D. Fu, "Preparation of $Ca_{0.8}Sm_{0.2}MnO_3$ powders and effects of calcination temperature on structure and electrical property," *Powder Technol.*, vol. 224, pp. 96–100, Jul. 2012.

[92] J. Lan, Y.-H. Lin, H. Fang, A. Mei, C.-W. Nan, Y. Liu, S. Xu, and M. Peters, "High-Temperature Thermoelectric Behaviors of Fine-Grained Gd-Doped $CaMnO_3$ Ceramics," *J. Am. Ceram. Soc.*, vol. 93, no. 8, pp. 2121–2124, Aug. 2010.

[93] S. Populoh, M. Trottmann, M. H. Aguire, and A. Weidenkaff, "Nanostructured Nb-substituted $CaMnO_3$ n-type thermoelectric material prepared in a continuous process by ultrasonic spray combustion," *J. Mater. Res.*, vol. 26, no. 15, pp. 1947–1952, Jul. 2011.

[94] E. Guilmeau, A. Maignan, and C. Martin, "Thermoelectric oxides: Effect of doping in delafossites and zinc oxide," in *Journal of Electronic Materials*, 2009, vol. 38, pp. 1104–1108.

[95] M. Ohtaki, T. Tsubota, K. Eguchi, and H. Arai, "High-temperature thermoelectric properties of $(Zn_{1-x}Al_x)O$," *J. Appl. Phys.*, vol. 79, no. 3, p. 1816, Feb. 1996.

[96] Y. Kinemuchi, M. Mikami, K. Kobayashi, K. Watari, and Y. Hotta, "Thermoelectric Properties of Nanograined ZnO," *J. Electron. Mater.*, vol. 39, no. 9, pp. 2059–2063, Dec. 2009.

[97] K. Park, J. K. Seong, and G. H. Kim, "NiO added $Zn_{1-x}Ni_xO$ ($0 \leq x \leq 0.05$) for thermoelectric power generation," *J. Alloys Compd.*, vol. 473, no. 1–2, pp. 423–427, Apr. 2009.

[98] K. Park and K. Y. Ko, "Effect of TiO_2 on high-temperature thermoelectric properties of ZnO," *J. Alloys Compd.*, vol. 430, no. 1–2, pp. 200–204, Mar. 2007.

[99] H. Yamaguchi, Y. Chonan, M. Oda, T. Komiyama, T. Aoyama, and S. Sugiyama, "Thermoelectric Properties of ZnO Ceramics Co-Doped with Al and Transition Metals," *J. Electron. Mater.*, vol. 40, no. 5, pp. 723–727, Feb. 2011.

[100] K. Park, K. Y. Ko, W.-S. Seo, W.-S. Cho, J.-G. Kim, and J. Y. Kim, "High-temperature thermoelectric properties of polycrystalline $Zn_{1-x-y}Al_xTi_yO$ ceramics," *J. Eur. Ceram. Soc.*, vol. 27, no. 2–3, pp. 813–817, Jan. 2007.

[101] M. Ohtaki, K. Araki, and K. Yamamoto, "High thermoelectric performance of dually doped ZnO ceramics," in *Journal of Electronic Materials*, 2009, vol. 38, pp. 1234–1238.

[102] N. Ma, J.-F. Li, B. P. Zhang, Y. H. Lin, L. R. Ren, and G. F. Chen, "Microstructure and thermoelectric properties of $Zn_{1-x}Al_xO$ ceramics fabricated by spark plasma sintering," *J. Phys. Chem. Solids*, vol. 71, no. 9, pp. 1344–1349, Sep. 2010.

[103] H. Cheng, X. J. Xu, H. H. Hng, and J. Ma, "Characterization of Al-doped ZnO thermoelectric materials prepared by RF plasma powder processing and hot press sintering," *Ceram. Int.*, vol. 35, no. 8, pp. 3067–3072, Dec. 2009.

[104] P. Jood, R. J. Mehta, Y. Zhang, G. Peleckis, X. Wang, R. W. Siegel, T. Borca-Tasciuc, S. X. Dou, and G. Ramanath, "Al-doped zinc oxide nanocomposites with enhanced thermoelectric properties," *Nano Lett.*, vol. 11, no. 10, pp. 4337–42, Oct. 2011.

[105] E. Combe, S. D. Bhame, E. Guilmeau, F. Boschini, and R. Cloots, "Synthesis of In2−xGexO3 nanopowders for thermoelectric applications," *J. Mater. Res.*, vol. 27, no. 02, pp. 500–505, Dec. 2011.

[106] J. Lan, Y.-H. Lin, Y. Liu, S. Xu, and C.-W. Nan, "High Thermoelectric Performance of Nanostructured In_2O_3-Based Ceramics," *J. Am. Ceram. Soc.*, vol. 95, no. 8, pp. 2465–2469, Aug. 2012.

[107] Y. Masuda, M. Ohta, W.-S. Seo, W. Pitschke, and K. Koumoto, "Structure and Thermoelectric Transport Properties of Isoelectronically Substituted $(ZnO)_5In_2O_3$," *J. Solid State Chem.*, vol. 150, pp. 221–227, 2000.

[108] S. Isobe, T. Tani, Y. Masuda, W.-S. Seo, and K. Koumoto, "Thermoelectric Performance of Yttrium-substituted $(ZnO)_5In_2O_3$ Improved through Ceramic Texturing," *Jpn. J. Appl. Phys.*, vol. 41, no. Part 1, No. 2A, pp. 731–732, Feb. 2002.

[109] Y. Liu, L.-D. Zhao, Y. Liu, J. Lan, W. Xu, F. Li, B.-P. Zhang, D. Berardan, N. Dragoe, Y.-H. Lin, C.-W. Nan, J.-F. Li, and H. Zhu, "Remarkable enhancement in thermoelectric performance of BiCuSeO by Cu deficiencies," *J. Am. Chem. Soc.*, vol. 133, no. 50, pp. 20112–5, Dec. 2011.

[110] L. D. Zhao, D. Berardan, Y. L. Pei, C. Byl, L. Pinsard-Gaudart, and N. Dragoe, "$Bi_{1-x}Sr_xCuSeO$ oxyselenides as promising thermoelectric materials," *Appl. Phys. Lett.*, vol. 97, no. 9, p. 092118, Sep. 2010.

[111] J. Li, J. Sui, Y. Pei, C. Barreteau, D. Berardan, N. Dragoe, W. Cai, J. He, and L.-D. Zhao, "A high thermoelectric figure of merit ZT > 1 in Ba heavily doped BiCuSeO oxyselenides," *Energy Environ. Sci.*, vol. 5, no. 9, p. 8543, Aug. 2012.

[112] J. Sui, J. Li, J. He, Y.-L. Pei, D. Berardan, H. Wu, N. Dragoe, W. Cai, and L.-D. Zhao, "Texturation boosts the thermoelectric performance of BiCuSeO oxyselenides," *Energy Environ. Sci.*, vol. 6, no. 10, p. 2916, Sep. 2013.

[113] F. Li and J.-F. Li, “Effect of Ni substitution on electrical and thermoelectric properties of $LaCoO_3$ ceramics,” *Ceram. Int.*, vol. 37, no. 1, pp. 105–110, Jan. 2011.

[114] S. Yanagiya, N. V. Nong, J. Xu, and N. Pryds, “The Effect of (Ag, Ni, Zn)-Addition on the Thermoelectric Properties of Copper Aluminate,” *Materials (Basel).*, vol. 3, no. 1, pp. 318–328, Jan. 2010.

[115] L. Wu, Q. Meng, C. Jooss, J.-C. Zheng, H. Inada, D. Su, Q. Li, and Y. Zhu, “Origin of Phonon Glass-Electron Crystal Behavior in Thermoelectric Layered Cobaltate,” *Adv. Funct. Mater.*, vol. 23, no. 46, pp. 5728–5736, Dec. 2013.

[116] M. N. Rahaman, *Ceramic Processing and Sintering*. CRC Press, 2003, p. 875.

[117] “The Pioneer of Spark Plasma Sintering (SPS) Systems,” *Fuji Electronic Industrial Co., Ltd.* [Online]. Available: http://sps.fdc.co.jp/.

[118] A. Sotelo, G. Constantinescu, S. Rasekh, M. A. Torres, J. C. Diez, and M. A. Madre, “Improvement of thermoelectric properties of $Ca_3Co_4O_9$ using soft chemistry synthetic methods,” *J. Eur. Ceram. Soc.*, vol. 32, no. 10, pp. 2415–2422, Aug. 2012.

[119] Q. Yao, D. L. Wang, L. D. Chen, X. Shi, and M. Zhou, “Effects of partial substitution of transition metals for cobalt on the high-temperature thermoelectric properties of $Ca_3Co_4O_{9+\delta}$,” *J. Appl. Phys.*, vol. 97, no. 10, p. 103905, 2005.

[120] Y. Zhang, J. Zhang, and Q. Lu, “Synthesis of highly textured $Ca_3Co_4O_{9+\delta}$ ceramics by spark plasma sintering,” *Ceram. Int.*, vol. 33, no. 7, pp. 1305–1308, Sep. 2007.

[121] H. Q. Liu, Y. Song, S. N. Zhang, X. B. Zhao, and F. P. Wang, “Thermoelectric properties of $Ca_{3-x}Y_xCo_4O_{9+\delta}$ ceramics,” *J. Phys. Chem. Solids*, vol. 70, no. 3–4, pp. 600–603, Mar. 2009.

[122] Y. Wang, Y. Sui, J. Cheng, X. Wang, W. Su, and H. Fan, “Influence of Y^{3+} doping on the high-temperature transport mechanism and thermoelectric response of misfit-layered $Ca_3Co_4O_9$,” *Appl. Phys. A*, vol. 99, no. 2, pp. 451–458, Jan. 2010.

[123] S. Pinitsoontorn, N. Lerssongkram, A. Harnwunggmoung, K. Kurosaki, and S. Yamanaka, “Synthesis, mechanical and magnetic properties of transition metals-doped $Ca_3Co_{3.8}M_{0.2}O_9$,” *J. Alloys Compd.*, vol. 503, no. 2, pp. 431–435, Aug. 2010.

[124] Y. Song, Q. Sun, L. R. Zhao, and F. P. Wang, “Rapid Synthesis of Bi Substituted $Ca_3Co_4O_9$ by a Polyacrylamide Gel Method and its High-Temperature Thermoelectric Power Factor,” *Key Eng. Mater.*, vol. 434–435, pp. 393–396, Mar. 2010.

[125] N. V. Nong, S. Yanagiya, S. Monica, N. Pryds, and M. Ohtaki, “High-Temperature Thermoelectric and Microstructural Characteristics of Cobalt-Based Oxides with Ga Substituted on the Co-Site,” *J. Electron. Mater.*, vol. 40, no. 5, pp. 716–722, Mar. 2011.

[126] J. Pei, G. Chen, N. Zhou, D. Q. Lu, and F. Xiao, "High temperature transport and thermoelectric properties of $Ca_{3-x}Er_xCo_4O_{9+\delta}$," *Phys. B Condens. Matter*, vol. 406, no. 3, pp. 571–574, Feb. 2011.

[127] F. P. Zhang, X. Zhang, Q. M. Lu, J. X. Zhang, Y. Q. Liu, and G. Z. Zhang, "Preparation and high temperature thermoelectric properties of $Ca_{3-x}Ag_xCo_4O_{9+\delta}$ oxides," *Solid State Ionics*, vol. 201, no. 1, pp. 1–5, Oct. 2011.

[128] Y. Ou, J. Peng, F. Li, Z. X. Yu, F. Y. Ma, S. H. Xie, J.-F. Li, and J. Y. Li, "The effects of dual doping on the thermoelectric properties of $Ca_{3-x}M_xCo_{4-y}Cu_yO_9$ (M = Na, La)," *J. Alloys Compd.*, vol. 526, pp. 139–144, Jun. 2012.

[129] F. Delorme, D. Ovono Ovono, P. Marudhachalam, C. Fernandez Martin, and O. Fraboulet, "Effect of precursors size on the thermoelectric properties of $Ca_3Co_4O_9$ ceramics," *Mater. Res. Bull.*, vol. 47, no. 5, pp. 1169–1175, May 2012.

[130] J. G. Noudem, D. Kenfaui, D. Chateigner, and M. Gomina, "Toward the enhancement of thermoelectric properties of lamellar $Ca_3Co_4O_9$ by edge-free spark plasma texturing," *Scr. Mater.*, vol. 66, no. 5, pp. 258–260, Mar. 2012.

[131] E. Woermann and A. Muan, "Phase equilibria in the system CaO-cobalt oxide in air," *J. Inorg. Nucl. Chem.*, vol. 32, no. 5, pp. 1455–1459, May 1970.

[132] N. V. Nong and M. Ohtaki, "Thermoelectric properties and local electronic structure of rare earth-doped $Ca_3Co_2O_6$," in *2006 25th International Conference on Thermoelectrics*, 2006, pp. 62–65.

[133] Y. Miyazaki, K. Kudo, M. Akoshima, Y. Ono, Y. Koike, and T. Kajitani, "Low-Temperature Thermoelectric Properties of the Composite Crystal $[Ca_2CoO_{3.34}]_{0.614}[CoO_2]$," *Jpn. J. Appl. Phys.*, vol. 39, no. Part 2, No. 6A, pp. L531–L533, Jun. 2000.

[134] S. Bhattacharya, D. K. Aswal, C. Thinaharan, S. K. Gupta, and J. V. Yakhmi, "Anisotropic electrical transport studies of $Ca_3Co_4O_9$ single crystals grown by the flux method," *J. Cryst. Growth*, vol. 277, no. 1–4, pp. 246–251, Apr. 2005.

[135] D. Kenfaui, B. Lenoir, D. Chateigner, B. Ouladdiaf, M. Gomina, and J. G. Noudem, "Development of multilayer textured $Ca_3Co_4O_9$ materials for thermoelectric generators: Influence of the anisotropy on the transport properties," *J. Eur. Ceram. Soc.*, vol. 32, no. 10, pp. 2405–2414, Aug. 2012.

[136] Y. Song and C.-W. Nan, "Preparation of $Ca_3Co_4O_9$ by polyacrylamide gel processing and its thermoelectric properties," *J. Sol–Gel Sci. Technol.*, vol. 44, no. 2, pp. 139–144, Aug. 2007.

[137] Y. Zhang and J. Zhang, "Rapid reactive synthesis and sintering of textured $Ca_3Co_4O_9$ ceramics by spark plasma sintering," *J. Mater. Process. Technol.*, vol. 208, no. 1–3, pp. 70–74, Nov. 2008.

[138] Y. F. Zhang, J. X. Zhang, Q. M. Lu, and Q. Y. Zhang, "Synthesis and characterization of $Ca_3Co_4O_9$ nanoparticles by citrate sol-gel method," *Mater. Lett.*, vol. 60, no. 20, pp. 2443–2446, Sep. 2006.

[139] M. P. Pechini, "Method of Preparing Lead and Alkaline Earth Titanates and Niobates and Coating Method Using the Same to Form a Capacitor," United States Patent US 00333069711-Jul-1967.

[140] L. R. Pederson, G. D. Maupin, W. J. Weber, D. J. McReady, and R. W. Stephens, "Combustion synthesis of $YBa_2Cu_3O_{7-x}$: glycine/metal nitrate method," *Mater. Lett.*, vol. 10, no. 9–10, pp. 437–443, Feb. 1991.

[141] S. Roy, D. A. Sharma, S. N. Roy, and H. S. Maiti, "Synthesis of $YBa_2Cu_3O_{7-x}$ powder by autoignition of citrate-nitrate gel," *J. Mater. Res.*, vol. 8, no. 11, pp. 2761–2766, Mar. 2011.

[142] Y. Liu, Y. Lin, Z. Shi, C.-W. Nan, and Z. Shen, "Preparation of $Ca_3Co_4O_9$ and Improvement of its Thermoelectric Properties by Spark Plasma Sintering," *J. Am. Ceram. Soc.*, vol. 88, no. 5, pp. 1337–1340, May 2005.

[143] F. K. Lotgering, "Topotactical reactions with ferrimagnetic oxides having hexagonal crystal structures—I," *J. Inorg. Nucl. Chem.*, vol. 9, no. 2, pp. 113–123, Feb. 1959.

[144] F. Wakai, H. Fukutome, N. Kobayashi, T. Misaki, Y. Shinoda, T. Akatsu, M. Sone, and Y. Higo, "Direct observation of sintering mechanics of a single grain boundary," *Acta Mater.*, vol. 60, no. 2, pp. 507–516, Jan. 2012.

[145] S. Chen, X. Song, X. Chen, Y. Chen, E. J. Barbero, E. L. Thomas, and P. N. Barnes, "Effect of precursor calcination temperature on the microstructure and thermoelectric properties of $Ca_3Co_4O_9$ ceramics," *J. Sol-Gel Sci. Technol.*, vol. 64, no. 3, pp. 627–636, Oct. 2012.

[146] D. Kenfaui, D. Chateigner, M. Gomina, and J. G. Noudem, "Texture, mechanical and thermoelectric properties of $Ca_3Co_4O_9$ ceramics," *J. Alloys Compd.*, vol. 490, no. 1–2, pp. 472–479, Feb. 2010.

[147] Y. Zhou, I. Matsubara, S. Horii, T. Takeuchi, R. Funahashi, M. Shikano, J. Shimoyama, K. Kishio, W. Shin, N. Izu, and N. Murayama, "Thermoelectric properties of highly grain-aligned and densified Co-based oxide ceramics," *J. Appl. Phys.*, vol. 93, no. 5, p. 2653, 2003.

[148] Y.-H. Lin, J. Lan, Z. Shen, Y. Liu, C.-W. Nan, and J.-F. Li, "High-temperature electrical transport behaviors in textured $Ca_3Co_4O_9$-based polycrystalline ceramics," *Appl. Phys. Lett.*, vol. 94, no. 7, p. 072107, 2009.

[149] T. Tani, H. Itahara, C. Xia, and J. Sugiyama, "Topotactic synthesis of highly-textured thermoelectric cobaltites," *J. Mater. Chem.*, vol. 13, no. 8, p. 1865, 2003.

[150] H. Itahara, J. Sugiyama, and T. Tani, "Enhancement of Electrical Conductivity in Thermoelectric $[Ca_2CoO_3]_{0.62}[CoO_2]$ Ceramics by Texture Improvement," *Jpn. J. Appl. Phys.*, vol. 43, no. 8A, pp. 5134–5139, Aug. 2004.

[151] E. Guilmeau, R. Funahashi, M. Mikami, K. Chong, and D. Chateigner, "Thermoelectric properties–texture relationship in highly oriented $Ca_3Co_4O_9$ composites," *Appl. Phys. Lett.*, vol. 85, no. 9, p. 1490, 2004.

[152] E. Guilmeau, H. Itahara, T. Tani, D. Chateigner, and D. Grebille, "Quantitative texture analysis of grain-aligned $[Ca_2CoO_3]]_{0.62}[CoO_2]$ ceramics processed by the reactive-templated grain growth method," *J. Appl. Phys.*, vol. 97, no. 6, p. 064902, 2005.

[153] Y. Wang, Y. Sui, J. Cheng, X. Wang, W. Su, X. Liu, and H. J. Fan, "Doping-Induced Metal−Insulator Transition and the Thermal Transport Properties in $Ca_{3-x}Y_xCo_4O_9$," *J. Phys. Chem. C*, vol. 114, no. 11, pp. 5174–5181, Mar. 2010.

[154] G. Yang, Q. Ramasse, and R. Klie, "Direct measurement of charge transfer in thermoelectric $Ca_3Co_4O_9$," *Phys. Rev. B*, vol. 78, no. 15, p. 153109, Oct. 2008.

[155] A. Bhaskar, Z.-R. Lin, and C. Liu, "Thermoelectric properties of $Ca_{2.95}Bi_{0.05}Co_{4-x}Fe_xO_{9+\delta}$ ($0 \leq x \leq 0.15$)," *Energy Convers. Manag.*, vol. 76, pp. 63–67, Dec. 2013.

[156] G. Constantinescu, S. Rasekh, M. A. Torres, J. C. Diez, M. A. Madre, and A. Sotelo, "Effect of Sr substitution for Ca on the $Ca_3Co_4O_9$ thermoelectric properties," *J. Alloys Compd.*, vol. 577, pp. 511–515, Nov. 2013.

[157] R. Tian, R. Donelson, C. D. Ling, P. E. R. Blanchard, T. Zhang, D. Chu, T. T. Tan, and S. Li, "Ga Substitution and Oxygen Diffusion Kinetics in $Ca_3Co_4O_{9+\delta}$-Based Thermoelectric Oxides," *J. Phys. Chem. C*, vol. 117, no. 26, pp. 13382–13387, Jul. 2013.

[158] T. Wu, T. a. Tyson, J. Bai, K. Pandya, C. Jaye, and D. Fischer, "On the origin of enhanced thermoelectricity in Fe doped $Ca_3Co_4O_9$," *J. Mater. Chem. C*, vol. 1, no. 26, p. 4114, 2013.

[159] S. Pinitsoontorn, N. Lerssongkram, N. Keawprak, and V. Amornkitbamrung, "Thermoelectric properties of transition metals-doped $Ca_3Co_{3.8}M_{0.2}O_{9+\delta}$ (M = Co, Cr, Fe, Ni, Cu and Zn)," *J. Mater. Sci. Mater. Electron.*, vol. 23, no. 5, pp. 1050–1056, Oct. 2011.

[160] S. W. Nam, J. W. Choi, H. K. Hwang, and K. Park, "Improvement in high-temperature thermoelectric properties by adding Mn for Co in $Ca_3Co_4O_9$," *J. Nanosci. Nanotechnol.*, vol. 10, pp. 7689–7693, 2010.

[161] Y. Wang, Y. Sui, P. Ren, L. Wang, X. Wang, W. Su, and H. Fan, "Strongly Correlated Properties and Enhanced Thermoelectric Response in $Ca_3Co_{4-x}M_xO_9$ (M = Fe, Mn, and Cu)," *Chem. Mater.*, vol. 22, no. 3, pp. 1155–1163, Feb. 2010.

[162] C.-J. Liu, J. Chen, L.-C. Huang, Z.-R. Lin, and C.-L. Chang, "X-ray absorption spectroscopy studies of Fe-doped misfit-layered $Ca_3Co_{4-x}Fe_xO_{9+\delta}$ (x = 0, 0.05, 0.1, and 0.15)," *J. Appl. Phys.*, vol. 102, no. 1, p. 014908, 2007.

[163] C.-J. Liu, L.-C. Huang, and J.-S. Wang, "Improvement of the thermoelectric characteristics of Fe-doped misfit-layered $Ca_3Co_{4-x}Fe_xO_{9+\delta}$ (x = 0, 0.05, 0.1, and 0.2)," *Appl. Phys. Lett.*, vol. 89, no. 20, p. 204102, 2006.

[164] N. W. Ashcroft and N. D. Mermin, *Solid state physics*. New York: Holt, Rinehart and Winston, 1976.

[165] Y. Wang, Y. Sui, J. Cheng, X. Wang, and W. Su, "Efficient room temperature thermoelectric characteristics of $Ca_{3-x}Ag_xCo_4O_{9+\delta}/Ag_y$ composites," *J. Phys. D. Appl. Phys.*, vol. 41, no. 4, p. 045406, Feb. 2008.

[166] G. D. Tang, X. N. Xu, C. P. Tang, Z. H. Wang, Y. He, L. Qiu, L. Y. Lv, L. Xing, and Y. W. Du, "The spin-entropy enhancement induced by Ce doping in $Ca_3Co_4O_{9+\delta}$," *EPL (Europhysics Lett.*, vol. 91, no. 1, p. 17002, Jul. 2010.

[167] G. D. Tang, Z. H. Wang, X. N. Xu, L. Qiu, and Y. W. Du, "Evidence of spin-density-wave transition and enhanced thermoelectric properties in $Ca_{3-x}Ce_xCo_4O_{9+\delta}$," *J. Appl. Phys.*, vol. 107, no. 5, p. 053715, 2010.

[168] R. D. Shannon, "Revised effective ionic radii and systematic studies of interatomic distances in halides and chalcogenides," *Acta Crystallogr. Sect. A*, vol. 32, no. 5, pp. 751–767, Sep. 1976.

[169] M. Khafizov, I.-W. Park, A. Chernatynskiy, L. He, J. Lin, J. J. Moore, D. Swank, T. Lillo, S. R. Phillpot, A. El-Azab, and D. H. Hurley, "Thermal Conductivity in Nanocrystalline Ceria Thin Films," *J. Am. Ceram. Soc.*, vol. 97, no. 2, pp. 562–569, Feb. 2014.